Experimental study of underexpanded round jets : nozzle lip thickness effects and screech closure mechanisms investigation

Thiago Lima de Assunção

THÈSE

Pour l'obtention du Grade de

DOCTEUR DE L'UNIVERSITÉ DE POITIERS

&

FACULTÉ DES SCIENCES FONDAMENTALES ET APPLIQUÉES

(Diplôme National - Arrêté du 7 août 2006)

École Doctorale : Sciences et Ingénierie en Matériaux, Mécanique, Energétique et Aéronautique.

Spécialité : MÉCANIQUE DES MILIEUX FLUIDES ET ACOUSTIQUE

Présentée par

Thiago Lima de Assunção

Experimental Study of Underexpanded Round Jets: Nozzle Lip Thickness Effects and Screech Closure Mechanisms Investigation

Directeur de thèse : Yves Gervais
Co-direction : Vincent Jaunet & Stève Girard
Soutenue le 20 12 2018
Devant la Commission d'Examen

JURY

Estelle PIOT	Ingénieure de Recherche, ONERA, France	Rapporteur
Stéphane BARRE	Directeur de Recherche, CNRS, France	Rapporteur
Christophe SCHRAM	Professeur, VKI, Belgium	Examinateur
Daniel EDGINGTON-MITCHELL	Professeur, Monash University, Australia	Examinateur
Éric GONCALVES	Professeur, ISAE-ENSMA, France	Examinateur
Peter JORDAN	Chargé de Recherche, CNRS, France	Examinateur
Yves GERVAIS	Professeur, Université de Poitiers, France	Examinateur
Vincent JAUNET	Maitre de Conférence, ENSMA, France	Examinateur

ACKNOWLEDGEMENTS

I would like to express my eternal gratitude to my advisor, Prof. Yves Gervais and co-advisors, Dr. Stève Girard and Dr. Vincent Jaunet. Prof. Yves always encouraged me in this very important task, giving me academic support to reach my research objectives. I am also extremely grateful to Dr. Stève for his meaningful help with the laboratory facilities and attention spent from the time of my arrival in Poitiers, providing me with the necessary serenity to carry out my work. I thank Dr. Vincent Jaunet for his crucial contribution in this work, providing enthusiastic discussions and meaningful advice about the Screech phenomenon research.

Special thanks to Dr. Matteo Mancinelli for his meaningful discussion on the VS model and Dr. Guillaume Lehnasch and Dr. Anton Lebedev for their constructive criticism of the work. I would also like to express thanks to the jury members: Dr. Estelle Piot, Dr. Stéphane Barre, Prof. Christophe Schram, Prof. Daniel Edgington-Mitchell, Prof. Éric Goncalves and Dr. Peter Jordan for their suggestions and constructive feedback on the manuscript.

I extend my sincere gratitue to my dear colleagues from the "salle des doctorants" (Igor, Selène, Marc, Tamon, Oghuzan, Maxime, Filipe, Eduardo and Ugur) for creating an awesome atmosphere of work and comradery.

I could not forget to express my thanks to all of the staff at the Prime Institut (Alex, Thomas, Romain T., Romain B., Damien, Redouane, Patrick B., Patrick L., Dominique and Nicolas) for their technical contribution in this work. Moreover, special thanks to Mme. Nadia Maamar for her important administrative support throughout the whole of my stay in France.

Thanks to the Brazilian National Council for Scientific and Technological Development (*CNPq*) for their support with tuition fees and the Brazilian Air Force (*FAB*) for the opportunity and financial resources.

Finally, I would like to express my infinite gratitude to my parents (Severino and Mônica) for their endless love. To end, I am immeasurably grateful to my beloved wife, Cintia, for her unconditional love and support, which has given me two blessed children: Matheus and Marina.

RESUME

Cette thèse est une contribution expérimentale à l'étude des résonances aéroacoustiques des jets sous-détendus : le Screech. Diverses méthodes expérimentales sont utilisées à cette fin, telles que la mesure de pression acoustique, la strioscopie et la Vélocimétrie par Image de Particules, et associées à des techniques classiques de post-traitement comme les décompositions en mode de Fourier et aux valeurs propres. Ces Techniques permettent d'évaluer les effets d'épaisseur de la lèvre de la buse sur l'écoulement, et fournissent des informations sur les différences de comportement d'un même jet montrant des modes oscillatoires différents. Enfin, on entreprend d'étudier la présence de divers mécanismes de fermeture de la boucle de résonance pour divers modes de Screech. La présence d'ondes intrinsèques au jet, se propageant vers l'aval pour les modes axisymétrique (*A2*) et hélicoïdal (*C*) suggèrent que ces ondes puissent jouer un rôle dans la résonance. La signature de ces ondes n'est en revanche pas attestée pour les modes battants (*B*). Ces résultats semblent donc indiquer que plusieurs mécanismes de rétroaction différents puissent être à l'oeuvre dans la résonance du jet sous-détendu.

ABSTRACT

This work provides an experimental contribution to the study of the Screech phenomenon. Various experimental techniques such as microphones array, Schlieren and Particle Image Velocimetry (PIV) together with advanced post-processing techniques like azimuthal Fourier decomposition and Proper Orthogonal Decomposition (POD) are employed. These techniques enable the evaluation of the lip thickness effects on the jets generated by two different round nozzles. The differences on the flow aerodynamics and acoustics are discussed. Then, we carry out experiments to analyse the effects of the different dominant Screech modes (*B* and *C*) on the flow characteristics. No noticeable differences are found in the mean fields. However, the fluctuation fields shows the contrary: B mode has larger fluctuation. In the last part, we investigate the Screech closure mechanism. The signature of upstream jet waves is revealed in the axisymmetric (*A2*) and helical (*C*) mode. However, the mode *B* does not present evidence of this instability in the flow, indicating that its closure mechanism may be bonded to another kind of waves. The conclusion from these results is that the Screech phenomenon seems be driven by different closure mechanisms.

TABLE OF CONTENTS

LIST OF FIGURES

INTRODUCTION

The aircraft noise at take off and landing is a well remarked social problem due to the settlements surrounding airports as well as the increase in air traffic. Hence, the society has demanded solutions to improve acoustic comfort either by political petition or by mobilization of public opinion. One recent example of this protest could be observed in the discussion about the airport project in the region of Notre-Dame-des-Landes, France. Aware of the importance of the subject, the stakeholders of the air transport have attempted to decrease the levels of the aircraft noise. For instance, in France, it is possible to mention the IROQUA (Initiative de Recherche pour l'Optimisation Acoustique Aeronautique) that was created in 2005 and established a collaborative network composed by research institutes (CNRS and ONERA) and enterprises (Safran, Airbus and Dassault Aviation) with the purpose of developing research that aims to decrease the noise generated by aircrafts, including the jet noise which is composed by mixing noise, BBSAN and Screech. Similar initiative has been developed in Brazil, in the scope of the Projeto Silence, with participation of UFSC (Universidade Federal de Santa Catarina) and Embraer.

The expansion process of underexpanded sonic jets in quiescent atmosphere leads to the formation of a train of shock-cell structures within the potential core, interacting with the jet turbulence inside of the mixing layer and producing "shock-associated noise". Under special self-resonance conditions these imperfectly expanded jets emit very intense pure tones, known as Screech, which was first pointed out by Powell (1953 *a*,*b*). Screech, as well as broadband shock-associated noise (BBSAN), are part of the shock noise.

Since the early works of Powell (1950's), screeching jets have been widely studied (see Raman (1999) for a review), but mostly from the acoustic point of view. The principle of its generation is commonly described by a global looping process in four steps: perturbations growing within the mixing layer, shock/turbulence interaction, backward propagation of acoustic wave (possibly through a so-called shock-leakage mechanism), and mixing layer selective re-excitation. The detailed physical mechanisms, involved at each step of this looping process, however remain unidentifiable. Therefore, the evaluation of the unsteady features of such jets is of paramount importance in order to understand the phenomena in its globality.

In addition to acoustic comfort issues, the Screech knowledge is also of paramount importance in safety issues due to its primarily upstream directivity. The phenomenon is able to cause structural damage and fatigue failure of aircraft components (Hay & Rose, 1970 and Seiner, Manning & Ponton 1987). The former authors pointed out that in the 1960's shock-cell noise was identified as a full scale phenomenon occurring under flight conditions leading to the appearance of some minor cracking of the tailplane structure of a VC 10 aircraft (fig. I.1). These cracks, at the first moment, were thought to be due to metal fatigue caused either by aerodynamic buffeting during reverse thrust engine operation or by jet noise. Afterwards, it was found out that the shock-cells, formed in the cruise flight, have emmited Screech tones that aggravated the fatigue failures in the structure components.

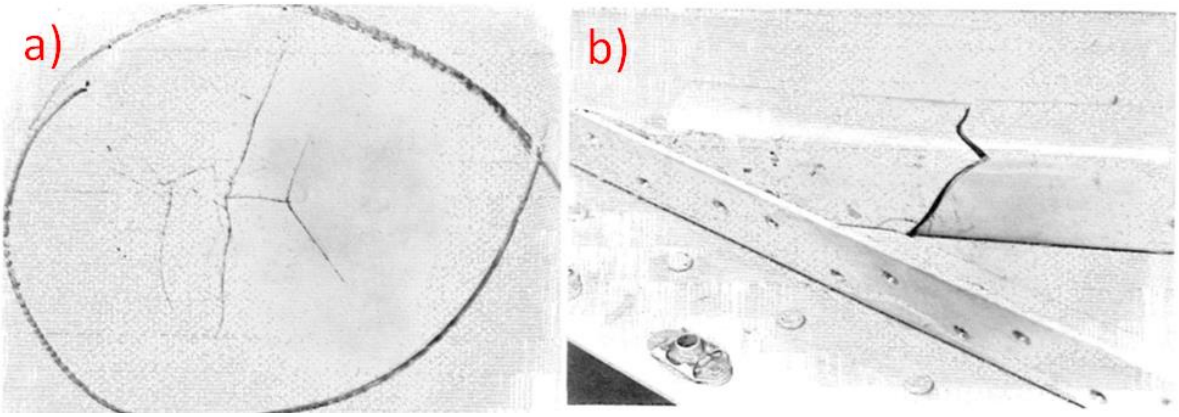

Figure I. 1: a) skin and b) stringer cracks. Hay & Rose (1970).

Therefore, the present manuscript aims to analyse the complex spatio-temporal organization of screeching jets, generated by two different convergent circular nozzles, and its link with their dominant sound emission. The detailed objectives of this manuscript are presented below:

1) Evaluate the lip thickness influence on the flow aerodynamics and acoustics: it is known that the nozzle lip thickness causes effects on the Screech phenomenon, thus we aim to analyse the differences in the flow aerodynamics caused by two different nozzles and its link with Screech generation;
2) Analyse the link between Screech modes and flow aerodynamics: we have the purpose of evaluate how the different dominant Screech modes influence the jet structures.
3) Investigate the Screech closure mechanism for different dominant modes: we carry out an investigation of the signature of the upstream-travelling intrinsic jet waves and their link with the Screech.

Thus, in order to reach these objectives the work is organized into five chapters. The chapter 1 presents the physics of underexpanded screeching jets via a literature review. The chapter 2 provides a description of the facilities together with the techniques employed for data analysis. In the chapter 3, we present information on how the acoustic, the topology and the flow structures are influenced by the nozzle lip thickness. The chapter 4 focuses on how the topology and the flow structures are influenced by two different dominant Screech modes *B* and *C*. A investigation about Screech closure mechanism by upstream-travelling waves inside of the jet is carried out in the chapter 5. Finally, all main results are summarized in the conclusion with suggestions and remarks for future works.

1 PHENOMENOLOGY

In this chapter we present the main aspects about the physics of underexpanded screeching jets. In the first part of this section the flow topology and the physical phenomena involved in nonideally supersonic jets such as the compressibility effects inside of the mixing layer, the shock-cell structure in the potential core, the shock leakage and the shock oscillations phenomena are presented as well as some principles of turbulence. In the last part, an overview of the Screech phenomenon is provided. The main aspects of this shock noise component are presented such as generation mechanism, modes, staging, sources, directionality, temperature and thickness influence as well as Screech influence on the jet topology.

1.1 Underexpanded Jets

A jet can be described as an outward flow, generated by a nozzle, in a generally resting environment. There are three important parameters for the jet flow: the nozzle's diameter (*D*), the Nozzle Pressure Ratio (*NPR)* and the Reynolds number (*Re)*. The hypothetical fully expanded jet diameter, named D_j (see eq. 1.1), is often used:

$$D_j = D\left[\frac{1+\frac{M_j^2(\gamma-1)}{2}}{1+\frac{(\gamma-1)}{2}}\right]^{\frac{\gamma+1}{4(\gamma-1)}}\left(\frac{1}{M_j}\right)^{\frac{1}{2}} \qquad \text{eq. 1.1}$$

where γ is the ratio between the specific heats (respectively at constant pressure and volume) and M_j the Mach number of the fully expanded jet under adiabatic and reversible conditions (isentropic). An analytical expression for M_j is given by:

$$M_j = \sqrt{\frac{2}{\gamma-1}\left(NPR^{\frac{\gamma-1}{\gamma}}-1\right)} \qquad \text{eq. 1.2}$$

where the *NPR* is the ratio between the total pressure (stagnation pressure P_o) inside of the plenum chamber of the tunnel and the ambiance exit pressure, P_a ($NPR = P_0/P_a$). This is an important parameter that defines the jet topology and it is important to notice that a convergent nozzle only provides a sonic flow if the *NPR* reaches a critical value of *1.89* (in the case of air flow). Within the context of a Screech study it is important to give the velocity of the hypothetical perfectly expanded jets (U_j), whose analytical expression is:

$$U_j = M_j\sqrt{\gamma R T_s} \qquad \text{eq. 1.3}$$

where T_s is the static temperature of the ideally expanded jet:

$$T_s = T_0\left(1+\frac{\gamma-1}{2}M_j^2\right)^{-1} \qquad \text{eq. 1.4}$$

According to Anderson Jr. (1991), supersonic jets are classified as a function of the nozzle exit pressure conditions (fig.1.1) and it is possible to establish three flow conditions: 1) if the isentropic pressure at the nozzle exit (p_{e6} in fig. 1.1) is smaller than the ambient pressure P_a (p_b in fig.1. 1) the jet is overexpanded and the shock waves formation allows the recovery of the ambient pressure; 2) if the isentropic pressure is equal to the ambient one, the jet is perfectly expanded; in this case no shock-cell formation is expected; 3) finally, if the isentropic pressure at the nozzle exit is larger than the ambient one, this mismatch induces the apparition of a

complex quasi-periodic shock-cell structure where the flow periodically expands and compresses, attempting to match the ambient pressure. The jet is said to be underexpanded in this case. In other words, the nozzle is too "short" for the flow to fully expanded.

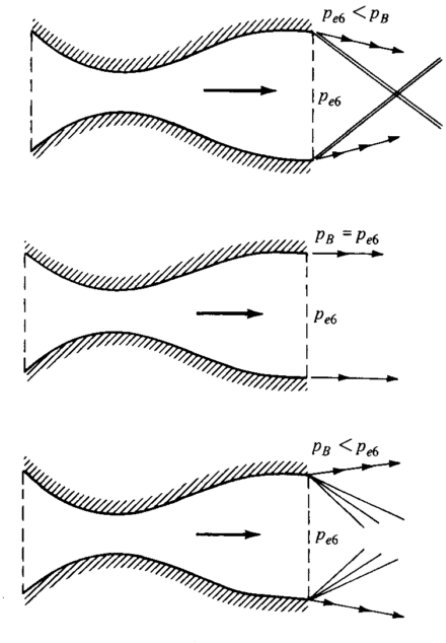

Figure 1. 1: three kinds of jet topology as a function of exit conditions. Overexpanded on the top, perfectly expanded in the middle and underexpanded at the bottom. Anderson Jr (1991).

Free jets are constituted by several regions (see figure 1.2): 1) the potential zone (Z_p) which is the zone where the jet flow is confined from the environment by the mixing layer and whose length is L_p (potential core length). For round jets this region is formed by a potential cone (C_p) at the end of which the eddy structures of the flow have a maximum size (Lehnasch, 2005); 2) a transition zone which is the region where the eddy structure sizes are reduced, becoming smaller and the flow getting a strong *3D* behaviour (Crow & Champagne ,1971); 3) the developed turbulence zone, consisting in a region that developed turbulence exists, where the flow dynamics are not influenced by the viscosity (Lesieur, 1997) and where the velocity and temperature profiles are in similarity.

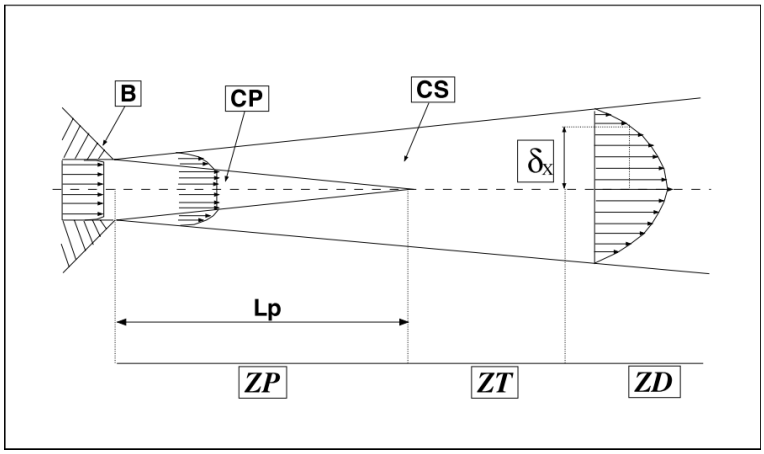

Figure 1. 2: global jet structure. Lehnasch (2005).

Lau *et al*. (1979) presents an analytical estimation of the potential core length (eq.1.5), based on the Mach number at the nozzle exit up to 2.5:

$$\frac{L_p}{D_j} = 4.2 + 1.1{M_j}^2 \qquad \text{eq. 1.5}$$

Tam *et al*. (1985) included in this estimation the temperature ratio between exit (T) and ambient (T_a) temperatures:

$$\frac{L_p}{D_j} = 4.2 + 1.1{M_j}^2 + \Delta(\frac{T}{T_a}) \qquad \text{eq. 1.6}$$

and:

$$\Delta(\frac{T}{T_a}) = \begin{cases} 1.1\ (1 - \frac{T}{T_a}) & for\ \frac{T}{T_a} \leq 1 \\ \exp\left[-3.2\left(\frac{T}{T_a} - 1\right)\right] - 1 & for\ \frac{T}{T_a} \geq 1 \end{cases}$$

1.1.1 Compressibility Effects

In the case of supersonic jets, the effect of increasing Mach number on the flow is not only represented by an increase in the jet velocity but also other physical modifications in the jet topology and the mixing layer turbulence**.** Panda (2006) pointed out that "an increase in the jet Mach number causes a progressive reduction in the growth rate of the lip shear layer which manifests in a lengthening of the potential core…" This effect on the mixing layer is known as *compressibility effects* and a brief description of this physical phenomenon is provided in the following.

The mixing layer is a result of the interaction of two parallel flows at different velocities, leading, as consequence in the case of jets, to a shear-layer between the potential core and the ambient (fig. 1.3).

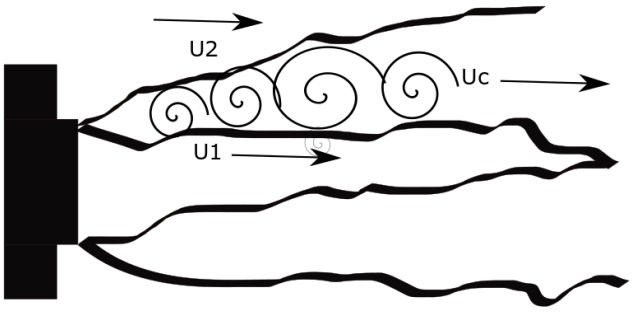

Figure 1. 3: sketch of the jet mixing layer. U_1 and U_2 are the fast and slow flow velocities in each side of the mixing layer, and *Uc* is the velocity of instabilities.

The shear-layer growth of supersonic jets is conditioned by the convective Mach number M_c that may be built as a function of the difference between the outer flow velocity and the velocity of instabilities (large vortices), U_c (Bogdanoff, 1983), where these large eddies are the most amplified instabilities of the flow (Ho & Huerre, 1984). M_c is also important as it influences, as well as U_c, the entrainment into the mixing region (Dimotakis, 1986).

Papamoschou & Bunyajitradulya (1997), in their work about large eddies evolution in the compressible shear layer, provide expressions for U_c and M_c:

$$U_c = (U_1 c_2 + U_2 c_1)/(c_1 + c_2) \quad \text{eq. 1.7}$$

$$M_c^1 = (U_1 - U_c)/a_1 \quad \text{eq. 1.8}$$

$$M_c^2 = (U_c - U_2)/a_2 \quad \text{eq. 1.9}$$

If we consider the stagnation region between the vortices as isentropic, then:

$$M_c^1 \approx M_c^2 \approx M_c = \frac{U_1 - U_2}{a_1 + a_2} \quad \text{eq. 1.10}$$

In the above equations, the index "1" and "2" refer to fast and slow flow velocities on each side of the mixing layer, respectively, and the parameter *a* is the local sound velocity. The mixing layer spreading rate is defined as the ratio between the vorticity thickness variation ($d\delta_\omega$) and the shear-layer length (*dx*). Dimotakis (1991) presented an equation for the spreading rate calculation, considering an incompressible flow:

$$\left(\frac{d\delta_\omega}{dx}\right)_i = C_\delta \frac{(1-r_u)(1+\sqrt{s})}{2(1+r_u\sqrt{s})}\left[1 - \frac{(1-\sqrt{s})(1+\sqrt{s})}{1+\frac{2.9(1+r_u)}{1-r_u}}\right] \quad \text{eq. 1.11}$$

where r_u is the ratio between the two velocities U_2 and U_1, s is the ratio between the two density ρ_2 and ρ_1, and C_δ is the spreading/growth constant. For compressible jets, as already mentioned, M_c is the parameter used to measure the compressibility effects on the growth of the mixing layer. Papamoschou & Roshko (1988) showed a relation between the spreading rate and M_c, based on the compressibility factor ϕ:

$$\delta'_\omega = \left(\frac{d\delta_\omega}{dx}\right)_i \phi(M_c) \quad \text{eq. 1.12}$$

Dimotakis (1991) presented an expression of this compressibility factor as a function of M_c:

$$\phi(M_c) = 0.2 + 0.8\exp(-3M_c^2) \quad \text{eq. 1.13}$$

Papamoschou & Roshko highlighted that the mixing layer growth rate decreases as M_c increases (see fig. 1.4) accompanied with similar reductions in the turbulent fluctuating velocities and shear stresses. Indeed, analysing the fig. 1.4, we can notice that the spreading rate falls abruptly from $Mc \approx 0.5$ and reaches a plateau for $Mc \approx 0.9$. Samimy and Elliott (1990) found that for $M_c = 0.54$ the vorticity thickness growth rates were over 20% higher than for $M_c = 0.64$.

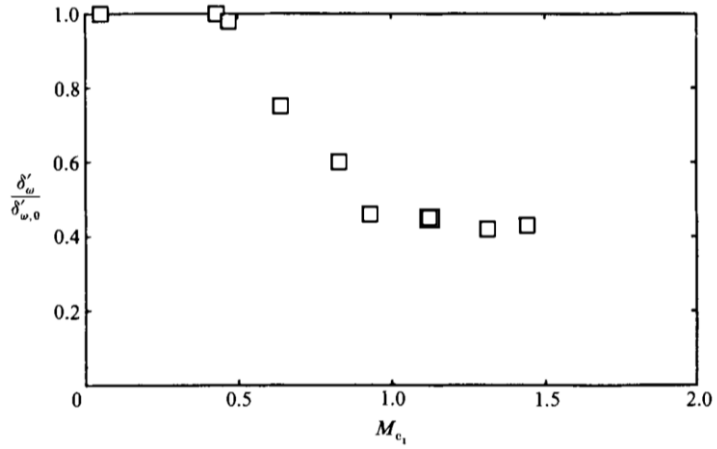

Figure 1. 4: experimental data of compressible mixing layer growth rate, normalized by incompressible value. Papamoschou & Roshko (1988).

To summarize, as M_c increases the spreading rate of compressible mixing layers decreases with a strong change in the slope of the mixing layer growth rate for $M_c \approx 0.5$. This effect is of course associated to the elongation of the potential core of supersonic jets. Other considerations regarding compressibility effects will be shown in the next section devoted to turbulence aspects.

1.1.2 Turbulence

Turbulent flows are unstable, with time and space dependent fluctuations. They have large diffusivity, are rotational, *3D* and present dissipative features. Moreover, they present difficulty in behaviour prevision (the effects are a set of events not connected to each other from which the phenomenon may become non-linear).

Turbulent large scale structures play an important role in the Screech phenomenon. For compressible shear-layer, their scales have, according to Papamoschou and Roshko (1988), a size of the local mixing layer thickness. Moreover, for underexpanded jets, the large scales are formed by the large vortices (Kelvin-Helmholtz instabilities) in the mixing layer (Brown and Roshko, 1974) as can be seen in fig. 1.5. The latter authors and Papamoschou & Bunyajitradulya (1997) pointed out the importance of large *coherent* structures for jet entrainment.

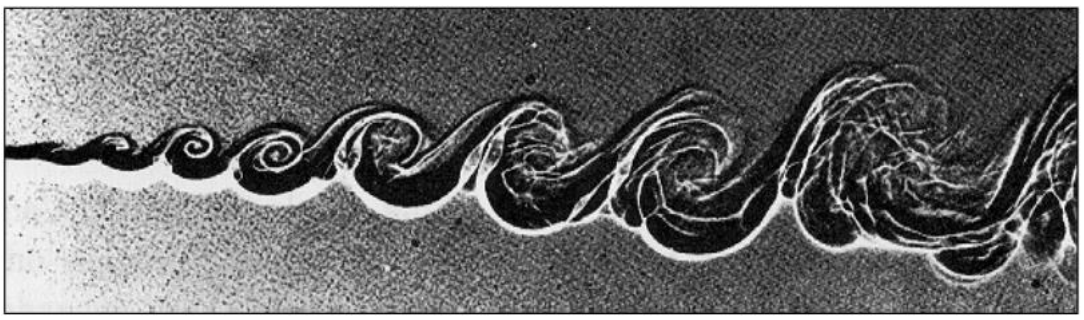

Figure 1. 5: Kelvin-Helmholtz instabilities. Brown & Roshko (1974).

The concept of *coherent* structures in turbulence may be defined as those that can be found downstream of the flow with the same initial upstream shape. This concept was

introduced in the 80's (Cantwell, 1981 and Hussain, 1983) and is very important because it gives an idea of how the turbulence may be treated as more than a random and chaotic movement in the flow. In the Screech analysis, large coherent structures have a major role in the noise generation dynamic, thus it is important when analysing turbulence to separate the random fluctuations from the organized ones (Alkislar *et al.*, 2003, Edgington-Mitchell *et al.*, 2014b and Tan *et al*., 2016).

In the case of the jet, the organized coherent structures have an elliptical shape as pointed out by Mahadevan & Loth (1994), Fleury *et al.* (2008) and André *et al.* (2014). It needs to be stressed that large turbulent scales have low frequency and large turbulent energy due to energy transport propriety, contrary to small ones that have a high frequency and low turbulence energy due to dissipation behaviour (Kerhervé *et al*., 2004 and Talbot *et al*., 2013).

Kastner *et al.* (2006) pointed out that mixing noise is formed by the large coherent structure breakdown, regardless of the Reynolds number studied. Mollo-Christensen (1967) was the first to suggest the importance of these structures as noise source, followed by Crow & Champagne (1971), Bishop *et al.* (1971), Tam (1972) and Morrison & McLaughlin (1979). Crighton (1975) cited that to understand the role of the large coherent structures in noise generation it is necessary to analyse their dynamic in unsteady flow conditions, in other words, a real-time flow field data analysis is required.

André *et al*. (2014) pointed out that for slightly underexpanded non screeching jet (M_j = 1.1), the sonic line and the centre line of the mixing layer are almost not modulated by the shocks, contrary to strongly underexpanded jet (M_j = 1.5). Concerning the turbulence levels, the results of André *et al.* (2014) agree with Seiner & Norum's results (1980) where it was observed that, for slightly underexpanded conditions, the turbulence level is almost unaffected by the shocks. However, for strong underexpansion this is no more valid and it is possible to observe a large modulation in turbulence levels. The same modulation due to shocks in the mixing layer was found by Panda & Seasholtz (1999) by density fluctuations measurements. Nevertheless, contrary to André *et al*. (2014), Tan *et al*. (2017) found out that even at low pressure ratio, the coherent structures are modulated by shocks. From the results of these authors, it is known that the shock system acts as a turbulence level suppressor.

The turbulence time scales provide information about how much time the structure remains coherent. André *et al*. (2014) pointed out that this scale decreases as M_j increases, although this trend is not very clear in the work of Panda (2006). Thus, this coherence falling may be explained by dissipative scales acting in the transition of the large scales into small ones when M_j increases. This behaviour may support Pao and Seiner's (1983) suggestion that the noise mechanism could be different for the low and high M_j.

Concerning integral length scales of turbulence (eddy size), Panda (2006) observed that it decreases with increasing frequency, thus small eddies have higher frequencies. In this work it was also noted that small eddies have a larger convective Mach number than large ones. Kerhervé *et al*. (2004) showed that jet energy is most efficiently used for large turbulent scales production with the small scales being quickly dissipated.

With reference to the convective Mach number, when it increases the turbulence becomes less organizated (Clemens & Mugal 1992 and Papamoschou & Bunyajitradulya, 1997). Normand (1990), from DNS simulation, has shown that for M_c >0.6 there is an inhibition of the Kelvin-Helmholtz instabilities and Samimy & Elliott (1990) noted that there is a tendency

to decrease the fluctuation levels as M_c increases. Similar results were found by Pantano & Sarkar (2002) and Fu & Li (2006) and may be understood as the compressibility effects on the turbulence.

As already mentioned, the Screech phenomenon is result of the interaction between shock and coherent structures propagating inside of the mixing layer. Therefore, the velocity of these instabilities, known as convective velocity (U_c), is an important parameter to be evaluated. The value of $0.7U_j$ is adopted for round jets and $0.55U_j$ for rectangular ones (Walker & Thomas, 1997) regardless of the M_j conditions. However, in Screech analysis these values for all M_j conditions does not explain the jet mode shifting (staging). For rectangular jets is not a large problem due to non-staging tendencies, meanwhile for underexpanded round jets these values are of paramount importance, due to fact that the changes in the flow dominant instability (staging) are related to changes in the convective velocity (phase velocity). Raman (1997) pointed out that convective velocity increases as M_j increases and quoted that this behaviour was also observed in Morrison & McLaughlin's works (1980) for round jets. Mercier *et al.* (2015) carried out a Schlieren analysis of high frequency samples and showed that the convective velocity changes with the downstream position where it increases until a certain distance of jet exit, making the concept of constant convective velocity questionable.

1.1.3 Shock-Cell Structure

Following Pack (1948), shocks are the result of a mechanism of internal reflection of expansion waves into compression ones at the jet boundary. The subsequent coalescence of the latter leads to a thin region through which the flow properties change abruptly, thus shocks are flow discontinuity. Love *et al*. (1959) and Johannesen (1957) showed through Schlieren images that shock waves are formed in underexpanded jets. Indeed, for underexpanded jets, the flow needs to equalize the over pressure at the nozzle exit with the ambient pressure. Hence, the expansion waves reflect as compression ones while compression waves (shock) reflect as expansion ones (see fig.1.6). However, in the jet centre line the reflection occurs in the same manner, in other words, compression waves reflecting into compression ones.

This natural attempt to equalize the jet pressure with the ambient one leads to a shock-cell structure formation with a diamond pattern, as can be seen in fig. 1.7. In underexpanded jets, depending on the expansion level, the first shock-cell could present a marked Mach disk that consists of normal shock formation due to shock reflection at the jet centre line. Subsequently, there is a formation of a subsonic zone behind it (fig. 1.8).

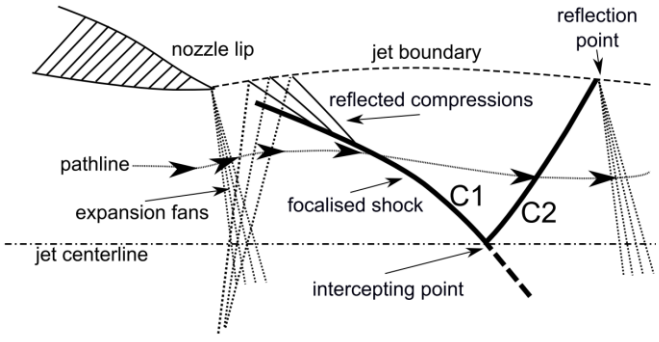

Figure 1. 6: shock-cell structure scheme. Savarese (2014).

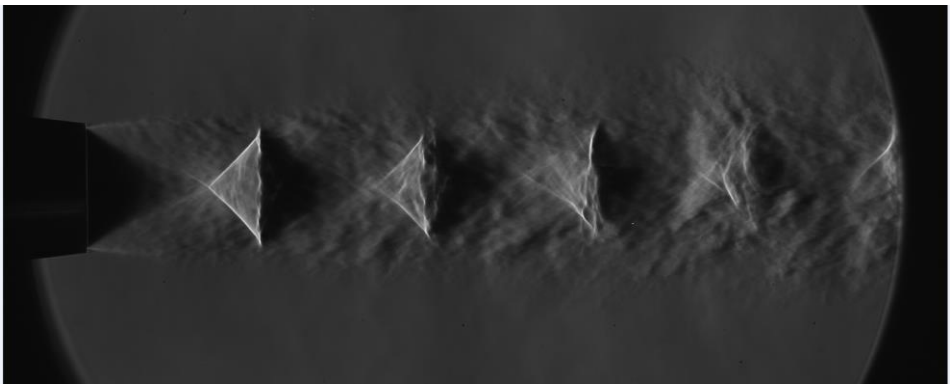

Figure 1. 7: Schlieren visualisation of shock-cell structure of the underexanded jet at Mj=1.50.

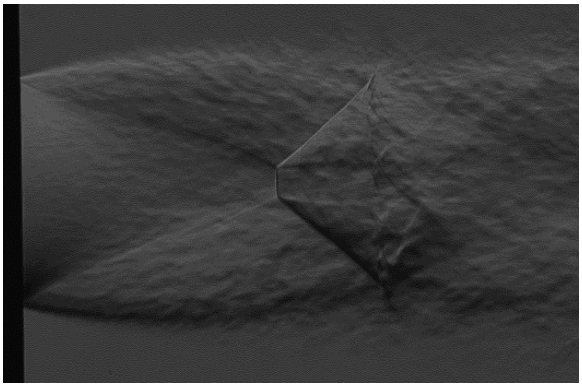

Figure 1. 8: Schlieren visualisation of a jet at *Mj=1.61* with a marked Mach disk.

A mathematical model for the shock-cell structure was first proposed by Prandtl (1904) and reworked by Pack (1950). It is known as Prandtl-Pack model. This theory takes into account a shock-cell structure model according to the following assumptions: 1) slightly imperfectly expanded jets; 2) small-amplitude pressure disturbances and 3) uniform jet base flow with vortex-sheet layer model. Following the mathematical model of Prandt-Pack's theory presented by Tam & Tanna (1982), the ratio between the shock-cell static pressure perturbation (p') and ambient pressure P_a, at first order solution and in cylindrical coordinates (r,x,θ), can be expressed as:

$$\frac{p'}{P_a} = \sum_{n=1}^{\infty} A_n \emptyset_n(r) \cos(k_n x) \qquad \text{eq. 1.14}$$

where:

$$A_n = \frac{2\Delta P}{\mu_n P_a} \qquad \text{eq. 1.15}$$

and the wavenumber of the n^{th} mode is given by:

$$k_n = \frac{2\mu_n}{D_j \beta} \qquad \text{eq. 1.16}$$

$$\beta = \sqrt{M_j^2 - 1} \qquad \text{eq. 1.17}$$

$\emptyset_n(r)$ is the set of orthonormalized eigenfunction $J_0(\frac{2\mu_n r}{\beta})/J_1(\mu_n)$, where J_0 and J_1 are the zero and first order Bessel's function of the first kind. The term μ_n is the n^{th} root of $J_0(\mu_n)=0$ and $\Delta P = P_e - P_a$, where the subscripts "*e*" and "*a*" refer to conditions at the nozzle exit and ambiance, respectively. Considering the first term in equation 1.14 and that the shock-cell wavelength is $2\pi/k_1$ it is possible to obtain the following expression for the shock-cell length:

$$L_s = \frac{2\pi}{k_1} = \frac{\pi D_j \beta}{\mu_1} \qquad \text{eq. 1.18}$$

as μ_1=2.40483, it comes:

$$L_s \approx 1.306 \beta D_j \qquad \text{eq. 1.19}$$

As already mentioned, the Prandt-Pack theory considers a vortex sheet model. It still remains valid close to the lip, where the shear layer is thin but loses accuracy further downstream. Tam *et al*. (1985) present a model that takes into account the enlargement of the mixing layer. However, the Prandt-Pack model already remains a good estimation of L_s, widely used in jets studies although it over predicts the shock-cell length (Gao & Li, 2009, Munday *et al*., 2011 and Heeb *et al*., 2014b).

1.1.3.1 Shock Leakage

As Screech is due to interaction between coherent structures in the mixing layer and the shock waves. It is important to understand one of the results of this interaction known as shock leakage. Under certain situations, compression waves do not stay confined inside the jet potential core and a part of their energy is released as pressure waves, producing noise. This "*escape*" is known as shock leakage. Suzuki & Lele (2003), in their numerical and *2D* work, have pointed out that the "shock leakage" is an interaction between shock and turbulence processes, where the shocks pass through a vortex-laden mixing layer, as can be seen in fig. 1.9 (Daviller *et al.*, 2013). The saddle point between two eddies allows for pressure waves to escape while the vortices are passing. In the frames "*D-F*" of the fig. 1.9, it is possible to observe that the pressure waves propagate in the upstream direction of the flow and possibly feed the Screech feedback mechanism. Thus, it appears that shock leakage occurs when the local vorticity weakens **(**Edgington-Mitchell *et al.*, 2014b).

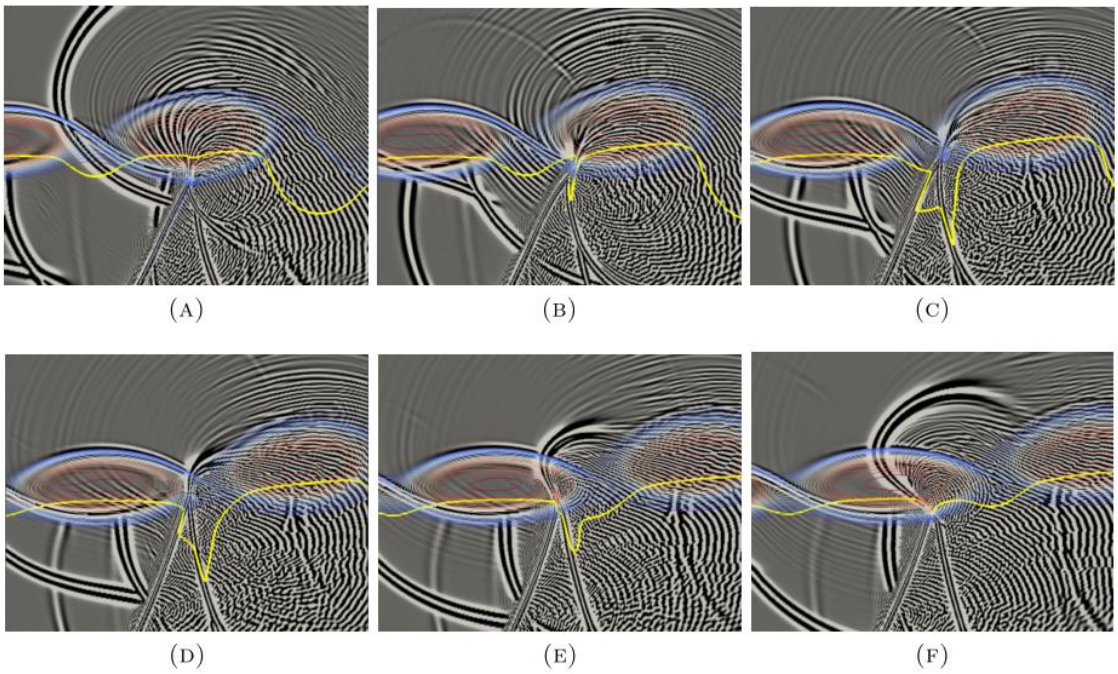

Figure 1. 9: instantaneous snapshots of shock leakage dynamic. Daviller et al. (2013).

Suzuki & Lele (2003) also noted that as the jet temperature increases it is easier for the shocks to penetrate the mixing layer, improving the shock leakage dynamics. Moreover, when the large coherent structure is broken down into the smaller structures the saddle points does not seem to be formed and the shock waves are scattered by the turbulence (Lee *et al*., 1993). Thus broadband shock noise is generated. Finally, Savarese (2014) pointed out that shock leakage phenomena has never been observed experimentally, only numerical studies were able to provide this behaviour and, up to 2017, shock leakage has still not been experimentally visualised. If found to the contrary, the author is not aware of this.

1.1.3.2 Shock Oscillations

Shock wave oscillations at screech frequencies were cited by Lassiter & Hubbard (1954) through a shadowgraph technique. With the same idea the shock-noise theory of Harper-Bourne & Fisher (1973) was based on the experimental observation that shock behaviours are correlated with the broadband shock noise component (BBSAN). Sherman *et al*. (1976), using a Schlieren analysis for shock distortion, noticed a relation between shock oscillations and Screech frequencies.

Later, Panda (1998) showed those shock oscillations in his work by laser light scattering acquired by Photo-Multiplier Tube, for two jet conditions (M_j *=1.19* and *1.42*), involving axisymmetric and helical Screech modes, respectively. He noticed that the motion of the shocks is more important in the jet core than close to the shear layer. However, this behaviour does not agree to what is expected, as the shock/vortices interaction at shear layer yields more flow unsteadiness. This may be explained by "damping" caused by the shock leakage phenomenon, for example. In his work, Panda showed that the first shock-cell does not have a large oscillation, contrary to the other ones. Another important result is that the mode fashion (fig. 1.10) and frequency of oscillations are the same of the Screech tone. The fig. 1.10 shows nine radial shock positions, on the third cell, for M_j=1.42 and at the different phases of Screech cycle

(τ/T_s). Considering the jet under helical mode, it is possible to see that there is a phase difference of about 180° in the shock oscillation (the lower half disappears at τ/T_s =0.17 and appears at 0.83). This behaviour is important because it shows that the shock/turbulence interaction has an important role in the Screech mechanism.

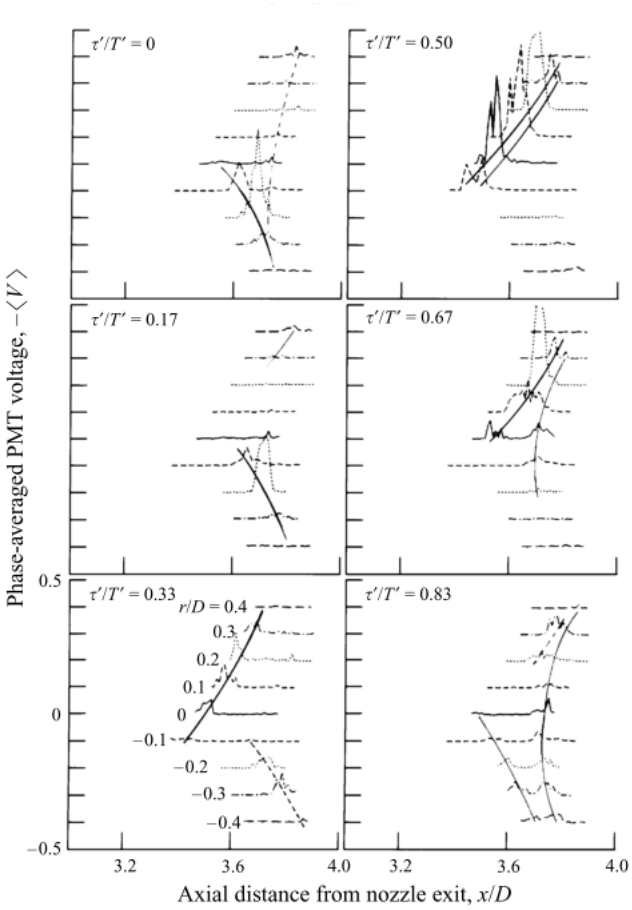

Figure 1. 10: phase-average PMT data obtained at nine radial positions, on third shock in Mj=1.42 and at the different phases of Screech cycle (τ/T_s). Panda (1998).

Panda also observed that the interaction between shock and large organized vortices causes shock splitting into two weaker ones, corroborated by Westley & Wooley (1968, 1970) who observed, by Schlieren film visualisations, that the interaction leads to a generation of a new shock. A possible explanation of the shock splitting is that when a vortical structure spills over the shock, the associated pressure fluctuations due to the passage of these structures are generated as well as a distortion of the super/subsonic interface. Hence, this oscillation may yield important information about large coherent structure turbulence, responsible for the Screech mechanism.

Finally, shock oscillations were also studied by André *et al.* (2011, 2012), in round convergent jets. In the former work, the authors apply an algorithm to high-speed Schlieren images for shock tips detection at the first and second cells and observed that the shock oscillation occurs at almost the same frequency than the Screech, as can be seen in fig. 1.11. In this image one can notice that the PSD (Power Spectral Density) of the near-field pressure and the shock location signal shows almost the same peak Screech frequency. Hence, we remark that the shock motion in the jet is linked to the Screech mechanism.

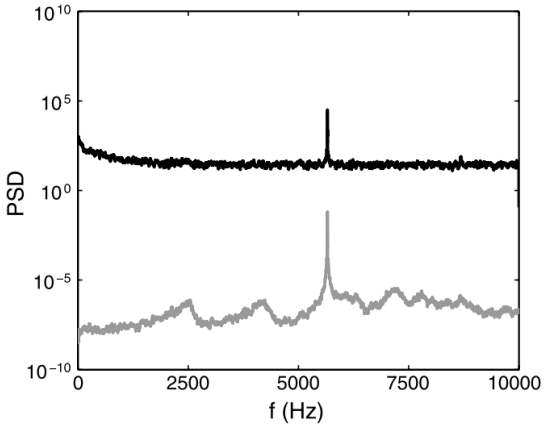

Figure 1. 11: PSD (Power Spectral Density) of near-field microphone signal (gray) and PSDx10^5 of the signal of containing the axial location at the first shock tip at NPR 2.27 (black). André et al. (2011).

1.2 Screech

The present section provides a review about Screech noise where the main aspects concerning the phenomenon are presented.

1.2.1 Underexpanded Jet Noise in Convergent Nozzle

According to Tam & Tanna (1982), the difference between convergent-divergent and convergent nozzles, concerning the operating conditions, is that the latter always underexpands while the former may be operated at under, over or design conditions. In their work, the authors showed that the minimum noise generation occurs when the nozzle operates at fully expanded condition (fig. 1.12), as in this case, the shock associated noise component is not present.

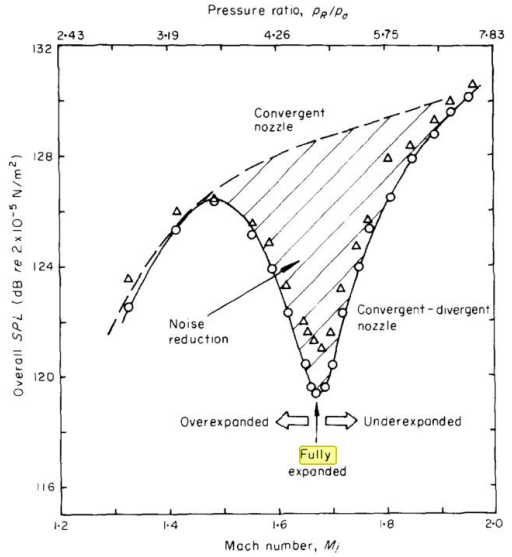

Figure 1. 12: noise intensity for nozzles undergoing different operating conditions. Tam & Tanna (1982).

The supersonic jet noise in imperfectly expanded flows, as already cited, is formed by turbulent mixing noise, broadband shock-associated noise (BBSAN) and Screech tones, where the two latter are linked to shock-cell structures and known as shock associated noise. André (2012) showed a typical far-field noise spectrum for the convergent nozzles with these three components identified (see fig. 1.13).

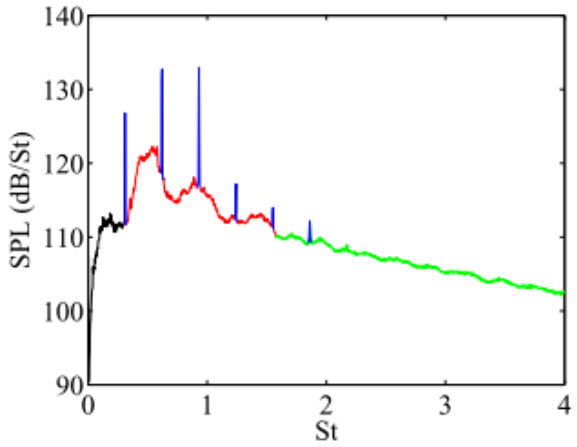

Figure 1. 13: typical jet noise spectrum of underexpanded nozzle in far field at *Mj=1.35*. The black line represents mixing noise, red line the broadband noise, blue line the screech noise and green line is the combination between mixing and broadband noise. André (2012).

1.2.2 Screech Modes and Staging

As M_j increases the Screech phenomena presents a curious behaviour for round and elliptical jets: frequencies jumps and structures shifts. These "stages", visualized as "jumps" in the Screech frequency curve, are called Screech modes and are classified according to jet mode instability. Powell (1953a) identified, for round jets, 4 screech modes that he named A, B, C and D. We report in fig. 1.14 the Screech frequency as a function of *Mj* from Panda *et al.* (1997), where the different modes are represented.

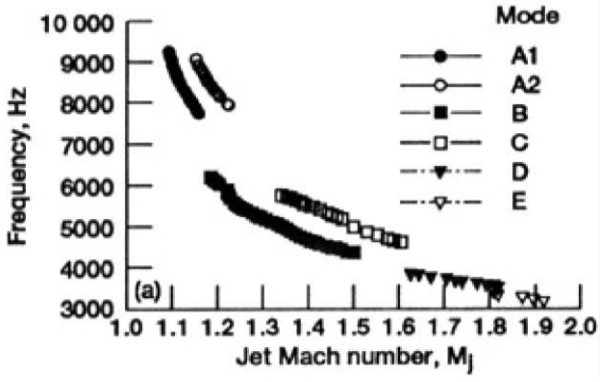

Figure 1. 14: screech modes for a circular convergent nozzle. Panda *et al.* (1997).

Powell (1953a) also showed that there is a hysteresis phenomenon between modes *C* and *D*, and that the transition from modes *A* to *B* is very large with respect to the shift in the frequency. Merle (1956) found that the mode *A* is constituted of two sub parts, *A1* and *A2*. Panda *et al*. (1997) found the existence of another mode that they called *E*. Clem *et al.* (2012) highlighted new screech modes B' and F, as can be seen in fig. 1.15. For the rectangular and

elliptical nozzle geometry, Panda *et al*. (1997) found that for the former the staging behaviour depends on the aspect ratio and the latter presents staging modes called *E1*, *E2* and *E3*.

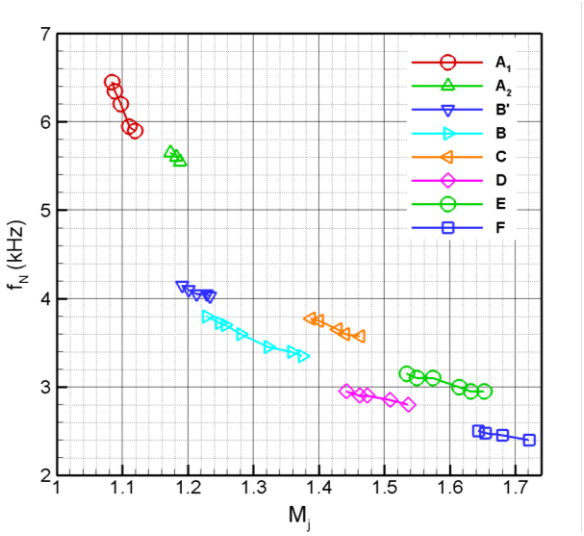

Figure 1. 15: fundamental Screech frequency versus *Mj* for 37.6 mm circular convergent nozzle. Clem et al. (2012)

Powell *et al*. (1992) employed a Schlieren system for visualisation and microphones to determine the mode organization: *A1* and *A2* are axisymmetric (or varicose mode), *B* is flapping (or sinuous), *C* is helical and *D* is flapping (or sinuous) too, which confirms previous Powell's observation. Similar results also were observed by Davies & Oldfield (1962). Nowadays, the mode *D* is considered to be a mode *B* extension (Edgington-Mitchell *et al*., 2015). It means that extrapolating mode *B*, in the Strouhal x M_j curve, the frequencies for *B* and *D* modes match together. Moreover, mode *B* is the result of the superposition of two helical modes with opposite signs (Zaman, 1999, Edgington-Mitchell *et al*., 2015 and Clem *et al*., 2016).

Powell *et al.* (1992) also observed the existence of primary (dominant) and secondary Screech frequencies, as shown in fig. 1.16. It is possible to notice that the jet can simultaneously present two frequencies (dominant and secondary). Moreover, Powell *et al.* showed that there is a hysteresis phenomenon during the transition between modes *C* and *D*, as already cited. In this work the authors showed the mode *u* which they suspected to be the continuation of the mode *A2*. However, due to weak tone and a lack of convincing evidence of continuity, this mode was marked as unidentifiable.

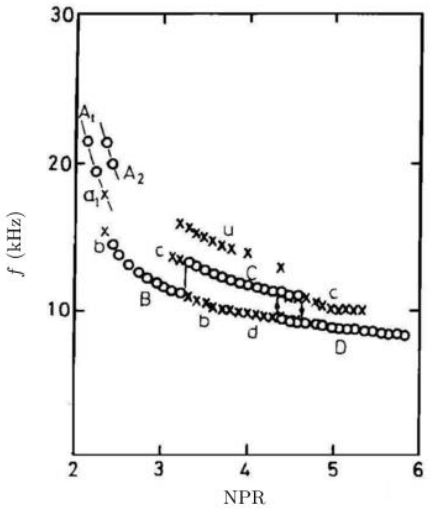

Figure 1. 16: screech frequency versus *NPR*. Frequencies of dominant modes (circles) and secondary modes (crosses). Powell et al. (1992).

Shen & Tam (2002) explained, using different mechanisms of feedback, that it is possible for two modes to coexist, refuting the earlier idea that Screech staging results in a continuous shifting from one mode to another. It is necessary to emphasize that the Screech staging phenomenon is still not completely clear: the physical mechanisms that rule this behaviour still need further study.

1.2.3 Mechanism

As already mentioned, the mechanism of Screech generation is cyclic. It consists of a looping behaviour with 4 phases: 1) perturbations (instabilities waves) increasing within the mixing layer and propagating downstream. They constitute the energy source of the Screech feedback loop (Tam, 1995); 2) shock/turbulence interaction; 3) backward propagation of acoustic waves, and; 4) instabilities re-excitation close to jet exit, restarting the loop (see fig. 1.17), where at this location the thin layer makes instabilities more susceptible to excitation (Kandula, 2008). The first description of the Screech feedback loop was provided by Powell (1953a). Raman (1997) presented Schlieren images of these phases (fig. 1.18) in his work about Screech suppression.

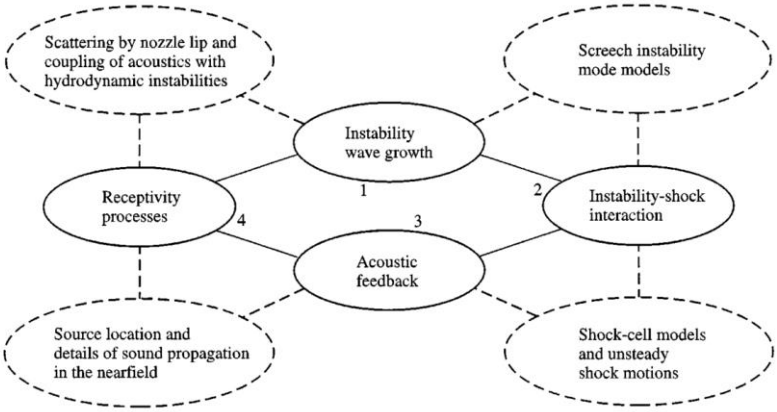

Figure 1. 17: diagram of screech loop (solid lines) and associated phenomena (dashed lines). Raman (1999).

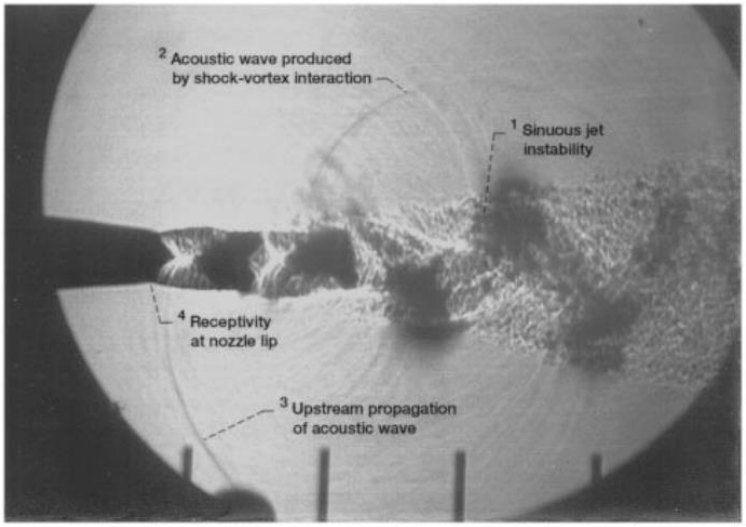

Figure 1. 18: Schlieren image of rectangular nozzle operating in screech loop. *Mj = 1.5*. Raman (1997).

Shen & Tam (2002) proposed that the feedback phenomenon may be closed by two kinds of disturbances propagating upstream, suggesting that 2 different closure mechanisms may exist. The first mechanism is depicted in fig. 1.19 and it was proposed by Tam *et al*. (1986). The *weakest link feedback loop model*, consists of interactions between the shock cell and amplified disturbances that generate acoustic perturbations propagating upstream, **outside of the jet shear layer**, reflecting on the nozzle lip and exciting new instabilities. For this model of feedback, Shen & Tam found a good agreement for the modes *A1* (axisymmetric) and *B* (flapping), meanwhile the results for the modes *A2* (axisymmetric) and *C* (helical) are poorly predicted. It is the *classical* or *standard* model of the Screech closure mechanism, also proposed by Powell (1953a).

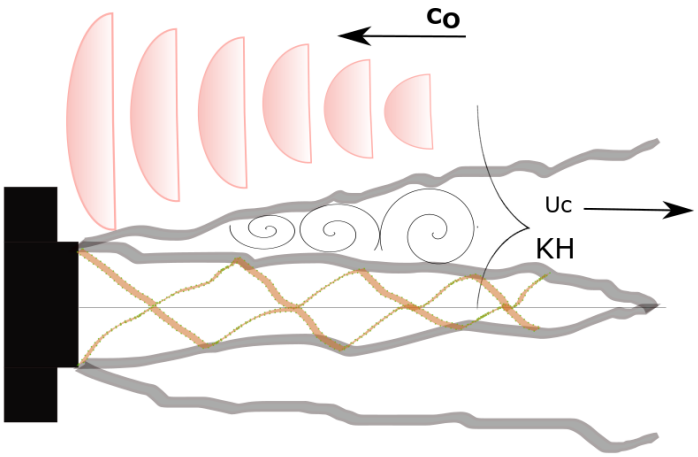

Figure 1. 19: sketch of the first Screech closure mechanism (classical model).

The second mechanism (fig. 1.20) is based on the presence of another kind of upstream instability waves, with spatial support **inside** and **outside** of the jet, identified by Tam & Hu (1989). Employing this model, Shen & Tam could predict the frequency of modes *A2* (axisymmetric) and *C* (helical). Recently, Edgington-Mitchell *et al.* (2018) showed the signature of this kind of instabilities for both axisymmetric modes *A1* and *A2*, indicating that these upstream-travelling disturbances may close the Screech feedback mechanism of all axisymmetric Screech tones.

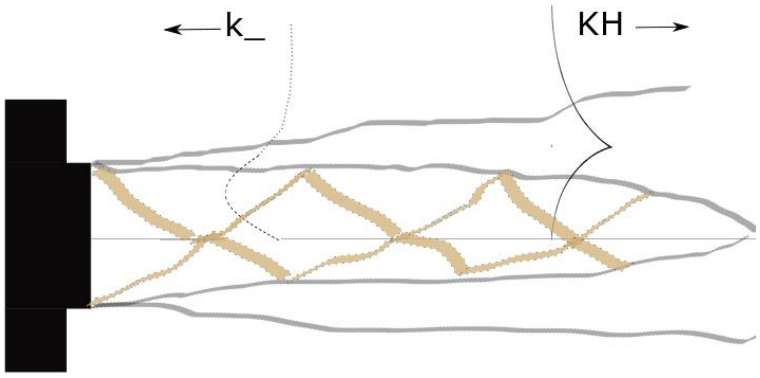

Figure 1. 20: sketch of the second Screech closure mechanism (jet modes).

According to Shen & Tam (2002), the presence of these two feedback models explains the coexistence of two Screech tones simultaneously. Later, Chatterjee *et al*. (2009) found that two feedback mechanisms are associated to two different length scales. The first one (classical) is linked to shock cell spacing and the second one (waveguide model) is bonded to the standing wavelength. Moreover, Edgington-Mitchell *et al.* (2015) pointed out that the jump in Screech frequency, for elliptical nozzles, may be associated to the transition between different acoustic feedback mechanisms.

To resume, the closure mechanism is still a debated question. No work in the literature has identified the signature of the second Screech closure in the modes *B* and *D*. Furthermore, Gojon *et al.* (2018) observed these waves in a numerical simulation but, no experimental observation is available for the mode *C*. If found to the contrary, the author is not aware of this.

1.2.4 Sources and Directionality

To analyse the shock/turbulence interaction responsible for the Screech generation, it is necessary to know where the acoustic sources are located. Powell (1953b) hypothesized that an array of sources are responsible for Screech noise, meanwhile from Schlieren observations Powell *et al*. (1992), Umeda & Ishii (2001) and Tam *et al.* (2014) pointed out that only one source contributes to the Screech. Davies & Oldfield (1962), from Schlieren analysis, determined that the predominant sources of screech are located between the 5^{th} and 6^{th} shock cells for *B* and *C* modes. Lee & Westley (1972) determined that the principal sources are located at the 4^{th} cellule for the *B* mode. Wlezien & Kibens (1988) determined that, for the *B* mode, the acoustic sources are located at the end of the 3^{rd} cell. Umeda & Ishii (2001) showed from a non-stationary (spark) Schlieren analysis that for the *A*, *B* and *C* modes the sources are located at the end of the 3^{rd} cell, and 5^{th} cell for *D* mode. Shen & Tam (2002) mentioned that the sources are placed between the 4^{th} and 5^{th} shock cell for the modes *A1*, *A2*, *B* and *C*. Gao & Li (2009) located the sources between the 2^{nd} and 4^{th} shock-cell for *A1*, *A2*, *B*, *C* and *D* modes. Mercier *et al.* (2016), through high speed Schlieren, established that, for *A* and *B* modes, the Screech sources are placed at the 4^{th} shock cell. In the case of rectangular jets, the sources are located between the 3^{rd} and 4^{th} shock-cells (Kaji & Nishijima, 1996, Walker & Thomas, 1997 and Raman, 1997). From all of these works we can ensure that the first six shock cells are responsible for the Screech tone generation. In order to summarize the screech sources, we present in table 1.1 the information obtained by different authors.

Table 1.1: shock cell positions of Screech sources for round jets.

Researcher	***A Mode***	***B Mode***	***C Mode***	***D Mode***
Powell (1953b)	*Array of Sources*			
Davies & Oldfield (1962)	-	*5^{th}-6^{th}*		-
Lee & Westley (1972)	-	*4^{th}*	-	-
Wlezien & Kibens (1988)	-	*3^{rd}*	-	-
Umeda & Ishii (2001)	*3^{rd}*			*5^{th}*
Shen & Tam (2002)	*4^{th}-5^{th}*			-
Gao & Li (2009)	*2^{th}-4^{th}*			
Mercier et al. (2016)	*4^{th}*		-	-

As already shown by Powell, the Screech dominant frequency and harmonics have a different directionality due to sources interaction. The fundamental frequency is more intense in the upstream and downstream directions while the first harmonic is more intense at 90° to the jet axis, as can be seen in fig. 1.21.

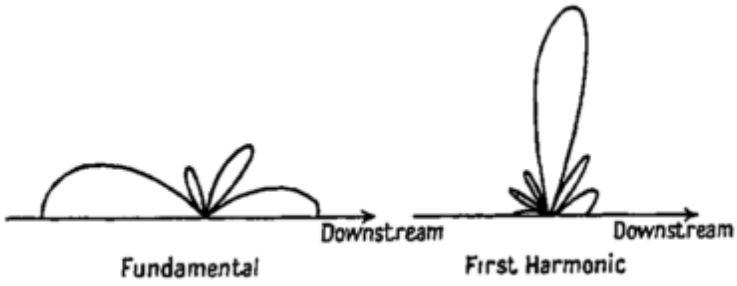

Figure 1. 21: Screech intensity directionality. Powell (1953a).

1.2.5 Jet Temperature Influence

From the eq. 1.3 we can notice that if the jet temperature increases the U_j (fully expanded jet velocity) increases too. The instability waves also may propagate at higher velocities (U_c) as temperature increases. Moreover, shock-cell structures (including spacing) are not temperature dependent (Krothapalli & Strykowski, 1996 and Shen & Tam, 2000). These facts lead to an increase of the Screech frequency as the temperature increases (Massey & Ahuja, 1997, Massey, 1997 and Shen & Tam, 2000). However, the Strouhal number ($\frac{f_s D_j}{U_j}$) does not present the same trend. Indeed, Shen & Tam (2000) do not find a large difference in the Strouhal number, in their work about effects of jet temperature on Screech tones.

Rosfjord & Toms (1975) showed that not only the Screech frequency increases with the temperature, but the modal structure changes too. Massey & Ahuja (1997) found the same behaviour concerning mode switching at elevated jet temperatures, where an increase in the jet total temperature inhibits the emergence of the flapping mode, as can be seen in fig. 1.22. One explanation for this behaviour may be found in Tam *et al*. (1994) where the authors mentioned that the temperature may change the most amplified modes of these instabilities at the same *Mj* condition, perhaps causing modal changes in the Screech phenomenon.

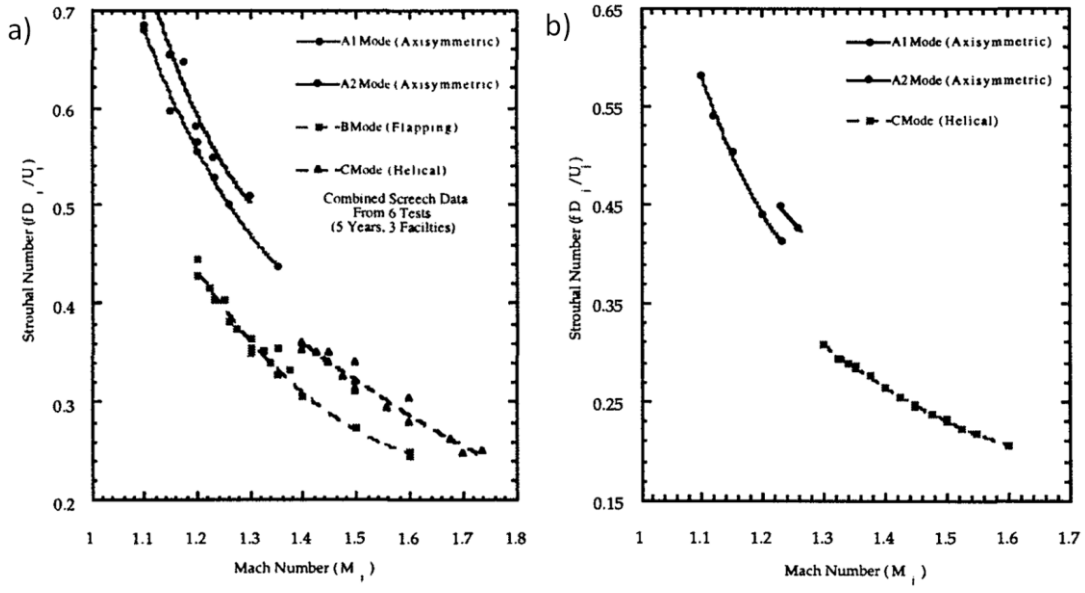

Figure 1. 22: dependence of the Screech modes with temperature for several Mj conditions, a) unheated jets and b) temperature ratio (*Tr*) 2.78. Massey & Ahuja (1997).

Massey *et al*. (1994), Krothapalli *et al.* (1997) and Viswanathan (2006) showed a decreasing of the Screech intensity for hot jets in their study. Krothapalli *et al.* (1997) explained that the reason for this amplitude reduction is that as the jet temperature increases, the *3D* instability waves amplify significantly, exceeding their *2D* counterpart due to an increase in the convective Mach number (Krothapalli & Strykowski, 1996). Thus, this phenomenon results in a loss of axisymmetric coherence in the flow that weakens the feedback loop, decreasing the Screech amplitude.

1.2.6 Nozzle Lip Thickness Influence

Ponton & Seiner (1992) observed that the Screech amplitude increases with the Mach number and then reaches a plateau until the Screech cessation. However, the authors showed that if the lip thickness is increased, the Screech's mechanism is reactivated and its cessation is retarded. The same trends are shown from the numerical simulations conducted by Shen & Tam (2000). The influence of the lip thickness for Screech reactivation is that a thick lip is able to scatter and reflect sound, such that there is an improvement in the receptivity and the re-excitation occurs again. In other words, for thin lip nozzle, the Screech re-excitation may be blocked by a large initial mixing layer that forbids the acoustic waves to reach the nozzle lip (Raman, 1997). This ability to scatter and reflect sound is also reported by Kim & Lee (2007), as can be seen in fig.1.23.

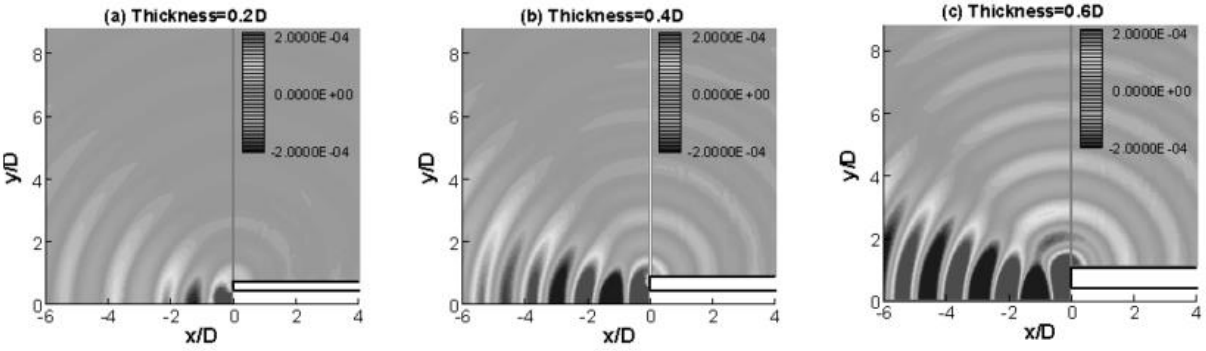

Figure 1. 23: comparison of instantaneous scattered pressure fields. Nozzle lip thickness: a) 0.2D, b) 0.4 D and c) 0.6D. Kim & Lee (2007).

Norum (1983) reported a large increase in the Screech intensity of mode *C*, of the order of 10 *dB* when using thick instead of thin lip nozzles. Similar results were found for rectangular jet studies (Raman, 1997). However, Ponton & Seiner (1992) and Shen & Tam (2000) (numerical work) obtained quite different results: the lip thickness increases slightly the Screech amplitude. The general trend is explained to be due to the increase in the oscillations strength as the lip becomes thicker. However, no appreciable change is shown when a certain thickness value is reached (Raman, 1998). Meanwhile, it is also known that the Screech amplitude is sensitive to environmental conditions and presents difficult in terms of repeatability which can explain the scatter of the results (André, 2012).

The Screech frequency is slightly modified by the lip thickness (Aoki *et al.* 2006). Ponton & Seiner (1992) observed that thick lip nozzle generates lower frequencies than thin lip one for *A* and *B* modes, and higher for *C* one. Another important feature observed by Ponton & Seiner (1992) is that the lip thickness causes modal changes in the jet. These changes may be

associated to an initial entrainment and/or an increase of disturbances amplification in the shear layer.

1.2.7 Cessation

As already mentioned, a decrease in the receptivity at the nozzle lip is responsible for natural Screech cessation and an increase of the lip thickness provides improvement in this receptivity, leading to Screech reactivation (Raman, 1997). This is shown in fig. 1.24 where an increasing in the lip thickness enables the Screech pehnomenon at higher *Mj*. Therefore, as Screech phenomenon is driven by feedback mechanisms, one can suppress it by avoiding the excitation of the instability waves at the nozzle lip. Physical feedback barriers positioned at certain locations downstream of the nozzle exit have been used to eliminate Screech (Ahuja 1984, 1985 and Rice & Raman, 1993). Moreover**,** Zaman (1999) pointed out that the presence of tabs may reduce (rectangular jets) or suppress (round jets) the Screech. The tabs produce two counter rotating vortices that increase the jet spread and may suppress this tonal noise. Wlezien & Kibens (1988) found the same results as well as Norum (1983). They pointed out that asymmetric nozzles generate asymmetric shocks that destroy the Screech feedback mechanism.

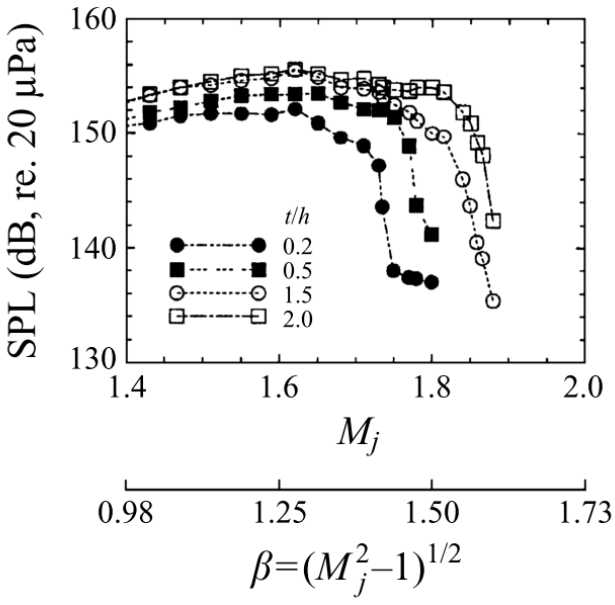

Figure 1. 24: shifting of rectangular jet Screech cessation versus Mj for various lip thickness. Raman (1997).

1.2.8 Frequency Estimation

Powell (1953a) proposed the first estimation of the Screech frequency. He considered that the Screech period (T_s) is composed of the time that the instabilities propagate in the mixing layer (L_s/Uc), until reach a shock wave, and the time for the upstream acoustic waves to reach the nozzle (L_s/a_0):

$$T_s = \frac{L_s}{U_c} + \frac{L_s}{a_0} \qquad \text{eq.1.20}$$

where L_s is the shock-cell length, U_c is the convective velocity of the coherent structures and a_0 is the ambient sound velocity. The eq. 1.20 can be rewrite as:

$$f_{S=}\frac{U_C}{L_S(1+M_C)} \qquad \text{eq. 1.21}$$

where f_s is the Screech frequency. In this equation the effect of temperature on screech frequency is not explicit. This problem was solved later by Tam *et al.* (1986) who obtained the Strouhal number (non-dimensional Screech frequency) as a function of M_j and $\frac{T_a}{T_t}$ (the ratio between ambient and total temperatures), as one can see in eq. 1.22.

$$\frac{f_s D_j}{U_j} = 0.67\left(M_j^2-1\right)^{-\frac{1}{2}}\left[1+0.7M_j\left(1+\frac{\gamma-1}{2}M_j^2\right)^{-\frac{1}{2}}\left(\frac{T_a}{T_t}\right)^{-\frac{1}{2}}\right]^{-1} \qquad \text{eq.1. 22}$$

However, this equation does not deal with staging phenomenon prediction or the presence of multiple Screech modes (Walker & Thomas, 1997). Several researchers have analysed L_s and U_c values for various jet conditions, taking into account screech modes of jets. The table below shows the ratio U_c/U_j obtained by different researchers considering several conditions, although the value 0.7 is commonly assumed, as already said.

Table 1.2: convective velocity of turbulent structure (*Uc/Uj*)

Researcher	A mode	B mode	C mode	D mode
Tam *et al.* (1986)		0.7		
Powell *et al.* (1992)	0.64	0.60-0.75	0.8	0.75
Panda *et al.* (1997)	0.67	0.58	0.66	0.69
Massey & Ahuja (1997)	0.67	0.6	0.62	-

Massey & Ahuja (1997) presented an equation different to the one given by Tam *et al.* (1986). The former authors took into account the frequencies of Screech jumps and adapted equation 1.22 for modes *A* and *C* (eqs. 1.23 and 1.24, respectively) with U_c obtained from measurements and coefficients chosen to fit the curve with experimental results:

$$\frac{f_s D_j}{U_j} = \frac{1.25}{1.1}0.63\left(M_j^2-1\right)^{-\frac{1}{3}}\left[1+0.63M_j\left(1+\frac{\gamma-1}{2}M_j^2\right)^{-\frac{1}{2}}\left(\frac{T_a}{T_t}\right)^{-\frac{1}{2}}\right]^{-1} \qquad \text{eq. 1.23}$$

$$\frac{f_s D_j}{U_j} = \frac{0.615}{1.1}\left(M_j^2-1\right)^{-\frac{1}{3}}\left[1+0.615M_j\left(1+\frac{\gamma-1}{2}M_j^2\right)^{-\frac{1}{2}}\left(\frac{T_a}{T_t}\right)^{-\frac{1}{2}}\right]^{-1} \qquad \text{eq. 1.24}$$

The term $\left(M_j^2-1\right)^{-\frac{1}{3}}$ instead of $\left(M_j^2-1\right)^{-\frac{1}{2}}$ was chosen empirically, and its value provides an improvement in order to adjust with the experimental data. For the mode *B*, André (2012) provides the equation:

$$\frac{f_s D_j}{U_j}=\frac{0.58}{1.1}\left(M_j^2-1\right)^{-\frac{1}{3}}\left[1+0.58M_j\left(1+\frac{\gamma-1}{2}M_j^2\right)^{-\frac{1}{2}}\left(\frac{T_a}{T_t}\right)^{-\frac{1}{2}}\right]^{-1} \qquad \text{eq. 1.25}$$

with L_s=$1.1\left(M_j^2-1\right)^{\frac{1}{3}}$ (shock-cell spacing) provided by Massey & Ahuja (1997) and the convective velocity found by Panda *et al.*'s work (U_c=*0.58*U_j). These modifications lead to enhancements in the agreement with his measured data. As already mentioned, mode *D* may be considered as a mode *B* continuation, so that estimation for this latter may be extrapolated and employed for the former.

In all of these estimations, the shock-cell length L_s is used to determine the Screech frequency. However, Panda (1999) replaced this length by the standing wave spacing (L_{sw}) which provides better agreement. The standing waves are formed by the interaction between hydrodynamic waves, which are due to the potential pressure field generated by coherent turbulent structures propagating downstream, and the acoustic pressure field which is due to the shock/turbulence interaction propagating upstream. Summarizing, these waves are result of the interaction between the propagation of the hydrodynamic (downstream) and the acoustic (upstream) waves.

Panda (1999) pointed out that this length may be obtained directly by observation of pressure fluctuations in the near-field of the jet. These fluctuations were also observed in the work of Westley & Woolley (1969, 1975) and Edgington-Mitchell *et al.* (2015). Raman & Rice (1994) and Hu & McLaughlin (1990) observed that hydrodynamic waves have the same Screech frequency (f_s). With this information, one can establish the following relations:

$$\frac{1}{L_{sw}}=\frac{1}{\lambda_s}+\frac{1}{\lambda_h} \qquad \text{eq. 1.26}$$

$$\lambda_s=\frac{c}{f_s} \qquad \text{eq. 1.27}$$

$$\lambda_h=\frac{U_c}{f_s} \qquad \text{eq. 1.28}$$

In the above equations, λ_s and λ_h are the wavelenghts of the upstream acoustic and downstream hydrodynamic instabilities, respectively. Rearranging the equations 1.26, 1.27 and 1.28 we obtain:

$$f_{s=\frac{U_c}{L_{sw}(1+M_c)}} \qquad \text{eq. 1.29}$$

which is similar to the equation obtained by Powell (1953a), but employing the standing wavelength L_{sw} instead of *Ls.*

Gao & Li (2009) found that the velocity is fairly modulated by the shock-cells. However, the pressure in the near-field does not show the same behaviour, demonstrating that it does not coincide with shock space locations, as can be seen in fig. 1.25 for M_j *=1.30.* Moreover, the modulation in the near-field pressure are linked to L_{sw}. Thus, from the fig. 1.25 one can remark that L_s and L_{sw} do not match. Indeed, Panda (1999) found that L_{sw} is about 80%

of the L_s for the two jets conditions (M_j = 1.19 and 1.42). It is important to notice that, according to Panda (1999), Tam *et al.* (1986) have used the same percentage ($0.8L_s$) in their empirical relation to determine Screech frequency (eq. 1.22). However, depending on the operation conditions, the standing wavelength can be smaller than, larger than or even equal to the shock spacing (Panda *et al.*, 1997).

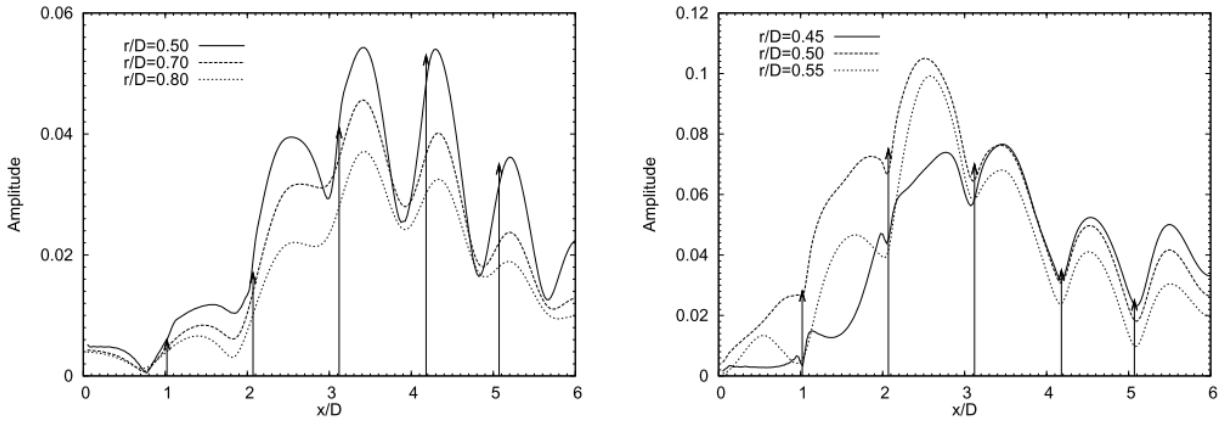

(a) Pressure disturbance (b) Steam-wise velocity disturbance

Figure 1. 25: a) amplitudes of the pressure fluctuations in the near field and b) steamwise velocity of screeching jets at *Mj= 1.30*. The vertical arrows in the figures represent shock locations. Gao & Li (2009).

Furthermore, it is also important to cite the works of Ahuja (1985) and Raman *et al.* (1997) regarding mixing layer receptivity where they noted, using a sound reflective surface, that the shock-cell spacing L_s does not change, meanwhile the Screech frequency does. Hence, the standing wavelength L_{sw} changes to adjust the sound generation according to a new configuration. Similar behaviour of unchanged variations of shock-cell spacing during stages jumps was found by Clem *et al*. (2016). Finally, Panda *et al*. (1997) calculated the standing wavelength and the shock-cell spacing versus M_j for three different nozzle geometries, as can be seen in fig. 1.26. It is clear in their work that, for circular nozzles, the standing wave presents a staging while the shock spacing does not.

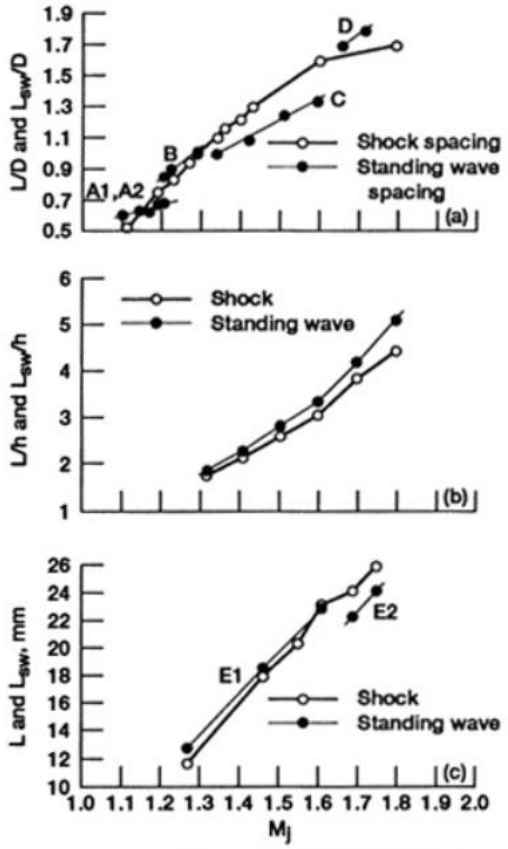

Figure 1. 26: average shock-cell and standing wave spacing versus *Mj* for 3 nozzle geometries: a) circular, b) rectangular and c) elliptical. Panda et al. (1997).

Although the standing wavelength L_{sw} represents the Screech staging from the flapping *B* to the helical *C* modes (decreasing when the frequency increases), we will see in the section devoted to the nozzle lip thickness effect the opposite tendency: this characteristic wavelength increases with Screech frequency. The interpretation of that depends on the behaviour of the coherent structures propagating inside of the mixing layer, leading to non trivial and subsequently non direct relation between this wavelength and the Screech frequency. As such, the author thinks that the L_{sw} is much more a result of the Screech phenomenon than a source of that, becoming the employ of the standing waves for frequency estimation questionable.

Finally, Gao & Li (2009) developed an analytical estimation for the Screech frequency based on their numerical simulations, Panda's work and experimental results of several authors. This method consists of a *polynomial adjustement* for each Screech mode estimation, as can be seen below.

$$S_t = \frac{f_s D}{U_j} = \frac{m\ C\ D}{nL(1+M_c)} \qquad \text{eq. 1.30}$$

$$\lambda_s = \frac{nL(1+M_c)}{mM_c} \qquad \text{eq. 1.31}$$

$$M_c = CM_j(1+\frac{\gamma-1}{2}M_j^2)^{-1/2}\sqrt{\frac{T_t}{T_a}} \qquad \text{eq. 1.32}$$

$$L_s = 1.26\sqrt{M_j^2 - 1} \qquad \text{eq. 1.33}$$

where n=5; m=5 (*A1*, *B* and *D* modes) or 6 (*A2* and *C* modes) and C=0.58 (axisymmetric modes) or 0.615 (flapping and helical modes). Note that the estimation of the shock-spacing L_s (eq. 1.33) is different to the Prandtl-Pack's theory (eq. 1.19) as its value was obtained adjusting the curve with numerical simulations (Gao & Li, 2009) and experimental data (Panda *et al*., 1997).

1.2.9 Screech Influence on Jet Topology

Screech causes differences on the flow topology of imperfectly expanded jets. Zaman (1999) pointed out that Screech increases jet spreading. According to the author, Screech causes jet excitation that changes vortices dynamics, decreasing random fluctuations and becomes them more organized and intensified. These structures roll-up periodically under excitation and their evolution consists of convection downstream and breaking down into disorganization near the end of the potential core leading to additional entrainment. Crow & Champagne (1971) showed that the entrainment is more pronounced when the "preferred modes" are reached under acoustic excitation. Thus, this organization, intensification and subsequent dynamics of the coherent structures are believed to lead to increase spreading of jets under Screech. This effect on jet spreading was also reported by Glass (1968) and Sherman *et al.* (1976) for circular jets and Krothapalli *et al.* (1986) for rectangular jets, as already cited. Moreover, considering that the large coherent structures are bonded to jet entrainment (Brown & Roshko, 1974 and Papamoschou & Bunyajitradulya, 1997), it is possible to infer that Screech may also increase it, through the organization and intensification of the vortices.

Screech on jet may cause shortening of the potential core (Glass, 1968 and Bridges & Wernet, 2008). However, Heeb *et al*. (2014a) noticed that this Screech effect on the potential core requires the Screech as dominant source of noise.

1.3 Conclusion

Underexpanded jets and associated Screech tones have received a lot of attention since the pioneering work of Powell. Nevertheless, we see that some details of this phenomenon are still debated. The Screech frequency estimations are based on the *empiricism*, performed by experimental data and the closure mechanism remains need to be elucidated, although meaningful contribution has been given by several authors. Screech staging is still not clear and the physical mechanism that rules this behaviour still needs further study.

2 EXPERIMENTAL TECHNIQUES AND FACILITIES

In this chapter we present the facilities and the techniques employed to measure and study supersonic jets issued from circular convergent nozzles. The experiments were carried out at the CEAT (Centre d'Études Aérodynamiques & Thermiques), a research centre linked to the P' Institute, a CNRS (*Centre National de la Recherche Scientifique)* laboratory.

2.1 Supersonic Flow Facility

The air flow is supplied at *200 bar* from the CEAT high pressure network and the pressure is adjusted by a regulation station, where the NPR (consequently the *Mj*) is monitored, ensuring a stable stagnation pressure within a maximum *NPR* variation $(\Delta NPR/NPR)_{max}$ of $\pm 0.35\%$. Thereafter, the flow passes through a heater (Vulcanic, DN 80 Type 10942) which is used to maintain total temperature (T_0) at about *293K*, ensuring constant and reproducible temperature. The reservoir pressure (stagnation pressure) is measured by a GE/Druck pressure transducer (UNIK 5000 PTX5072) with a pressure range of *0-10 bar* installed in the plenum chamber and the total temperature is acquired by type *K* thermocouple.

To investigate the supersonic flow, two circular convergent nozzles with a *10 mm* outlet diameter were employed with different geometries (fig. 2.1). The nozzles have *0.03D* and *1.0D* lip thickness, respectively, and in the present work they are labelled as thin (*0.03D*) and thick lip (*1.0D*). We employ a cylindrical coordinates system (*r, x*, θ*)*, corresponding to radial, axial and azimuthal coordinates, respectively. The reference system as well as a layout of the supersonic jet experimental facility are depicted in fig. 2.2. As said above, the system is supplied by a continuous flow of high pressure air and the flow passes through a porous muffler before entering the plenum chamber and exiting through the nozzle.

Figure 2. 1: evaluated nozzles. Thin lip (left) and thick lip (right).

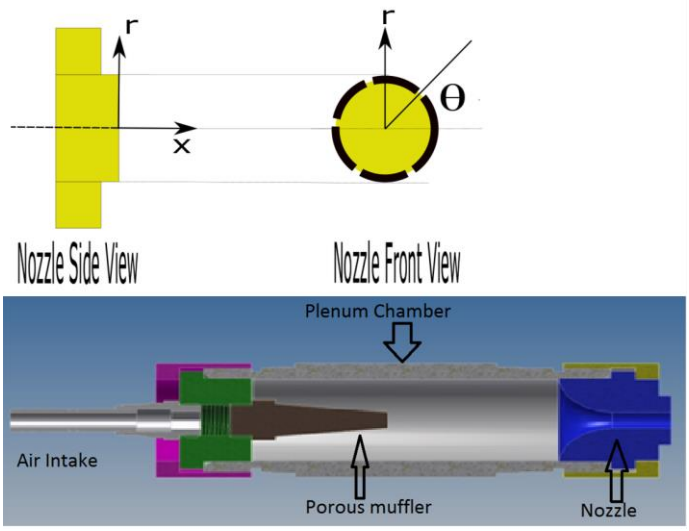

Figure 2. 2: coordinates system centered at the nozzle exit (top) and layout of supersonic flow facility (bottom).

2.2 Acoustic Measurements

To perform an azimuthal Fourier decomposition of the sound pressure fields generated by underexpanded jets, an array of 6 microphones was employed providing an azimuth angle sampling of $\pi/3$, as can be seen in fig. 2.3. Moreover, ¼" GRAS microphones (46BP model) and a PXIe-1071 system of National Instruments were employed with an acquisition frequency of 200 *kHz* and *30s* for each test which provided signals of *6M* points. The frequency of acquisition enables temporal analysis of the phenomenon due to the fact that it is 5 to 6 times larger than the characteristics frequencies of the flow ($fc= U_j/ D_j$).

The array was located parallely to the jet exit section and each microphone was positioned at a radius of *1.5D* to the jet axis. The calibration was performed by a Brüel & Kjaer sound calibrator (pistonphone), Type 4231. We performed detailed acoustic measurement over a *Mj* range between *1.0* and *1.86*, with $\Delta M_j = 0.02$, providing 44 jets conditions considered for each nozzle. The experiments were not carried out in an anechoic chamber, but foam was used on the background frame of the supersonic flow facility to mitigate the sound reflexion effects.

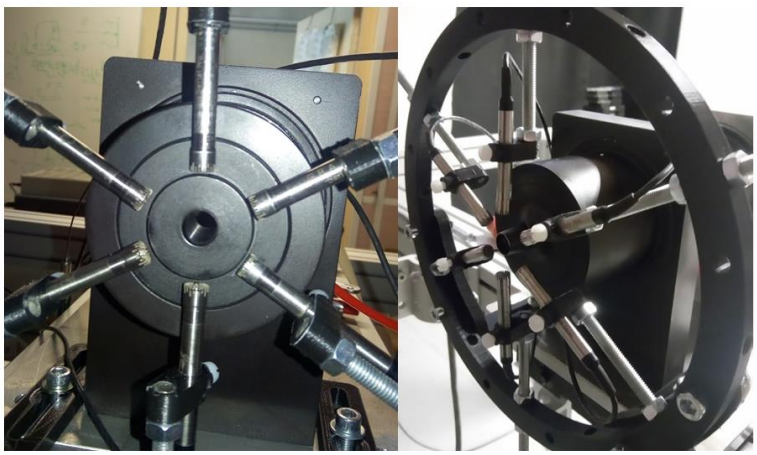

Figure 2. 3: microphone array employed for azimuthal Fourier decomposition.

Azimuthal Fourier decomposition is useful to isolate the sound pressure fluctuations correlated to the azimuthal direction (Cavalieri *et al.*, 2012). Moreover, it is known that the low order (*m=0, m=±1,…*) azimuthal modes are strongly related to large scale coherent structures of the flow (Weightman *et a*l., 2017). Thus, from the jet azimuthal Fourier decomposition, it is possible to assess the sound radiation by Screech, identifying which mode is present in the flow (Massey & Ahuja, 1997). Hence, to transform the sound pressure field, $p(x,\theta,t)$, acquired by the microphones array into Fourier modes the equation below can be employed:

$$p_m(x,t) = \frac{1}{2\pi}\int_0^{2\pi} p(x,\theta,t)e^{im\theta}d\theta \qquad \text{eq. 2.1}$$

where θ is the azimuth angle and *m* the order of the Fourier mode. It is important to recall that in the Fourier transform, due to symmetry property, the positive (*m=1,2,3,…*) and negative (*m=-1,-2,-3,…*) mode numbers form conjugate pairs, for instance, $p'_1 = p'^{*}_{-1}$, whilst the mode *0* (axisymmetric mode) is real.

Thereafter, the energy of the azimuthal pressure modes is obtained by computing their PSD (Power Spectral Density). Moreover, it is well known that Screech is axisymmetric, flapping or helical (Powell *et al*., 1992) and that each of these modes provides a signature on a specific azimuthal Fourier mode. However, the flapping and helical Screech modes, in the Fourier decomposition, are represented by either *m=-1* or *m=1* or both. Hence, taking into account this characteristic, only the azimuthal modes *m=0* and *m=1* are evaluated as these two modes represent all the Screech ones.

A microphone in far-field, at 90° and placed at *46D* from the nozzle exit, was also used in order to measure the acoustic pressure fluctuations. This was also done during the Schlieren and PIV experiments, enabling to monitor the jet Screech modes during these experiments.

2.3 Schlieren Experiments

The Schlieren visualization is performed to evaluate the general flow topology. Although it is an "integral line-sight" technique it allows to obtain information about the shock-cells as well as insightful information about near-field gradient density fluctuations resulting from coherent vortices passage inside the shear layer.

A Toepeler Z-type Schlieren was employed in this study, where a layout can be seen in fig. 2.4. Instantaneous images were taken using two 75mm mirrors with a 500 mm focal distance. A 4 MP camera (CCD Camera JAI/Pulnix TMC-4200CL) equipped with a 100 mm lens (Tokina AT-X M100 Pro D A) is used, providing *26 pix/mm* of spatial resolution and therefore a field of view of approximately *6.5D*. A LED (Light Emitting Diode) light source was employed as illumination, with a *3 μs* pulse duration. This yields sufficient light intensity with short pulse illumination at a relatively low cost and without the risks concerning the use of LASER (Settles & Hargather, 2017). This time scale (*3 μs*) is able to provide instantaneous Schlieren visualisation due to fact that it is lower than the characteristic flow time scales (D_j/U_j) where this latter has an order of magnitude about *25 μs*. The sample analysed consisted in a set of 1000 images, acquired at a frequency of *10 Hz* (*fps*). This acquisition frequency does not allow time-resolved analysis of the phenomenon due to fact that the characteristic frequencies of the flow ($fc= U_j/ D_j$) are of an order of magnitude of 40 *kHz*.

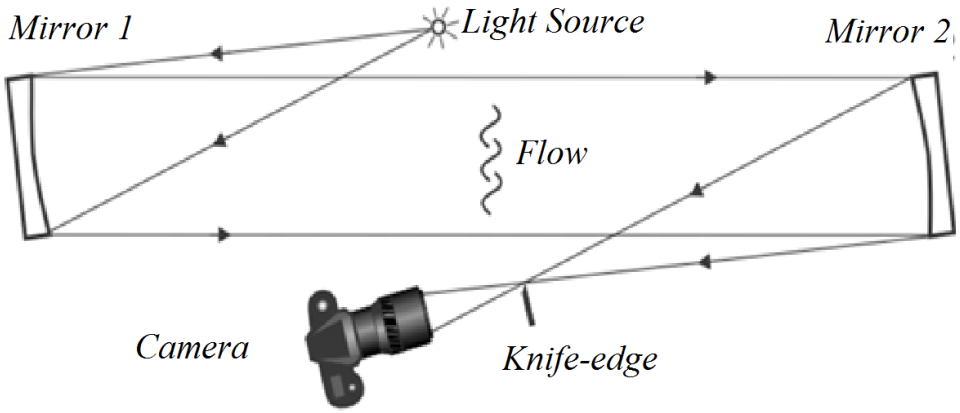

Figure 2. 4: Toepler Z-type Schlieren layout. Settles & Hargather (2017), modified.

The knife-edge was placed perpendicularly to the jet axis, allowing axial density gradient ($\partial\rho/\partial x$) observation. The experiments were performed for four M_j conditions and for both nozzles. Flow parameters selected for Schlieren are depicted in the table. 2.1. The conditions analysed covered the jets under two Screech dominant instability modes, either flapping or helical, respectively. Moreover, for the jet generated by the thick lip nozzle, two distinct dominant modes *B* and *C* were evaluated at $Mj = 1.5$.

Table 2.1: analysed flow conditions by Schlieren experiments. $T_0 = 293K$ and $Re_j = \rho_j U_j D_j / \mu$.

Thin lip nozzle				
NPR	M_j	*Mode*	U_j *(m/s)*	Re_j
2.89	*1.33*	*B*	*392*	*3.65E+05*
3.67	*1.50*	*B*	*427*	*4.44E+05*
4.34	*1.61*	*B*	*449*	*5.07E+05*
5.45	*1.76*	*B*	*475*	*6.04E+05*
Thick lip nozzle				
NPR	M_j	*Mode*	U_j *(m/s)*	Re_j
2.89	*1.33*	*B*	*392*	*3.65E+05*
3.67	*1.50*	*B,C*	*427*	*4.44E+05*
4.34	*1.61*	*B*	*449*	*5.07E+05*
5.45	*1.76*	*B*	*475*	*6.04E+05*

The results of the Schlieren visualisation are treated in the chapters 3 and 4 where the effects of the nozzle lip thickness and Screech modes on the flow are evaluated.

2.4 PIV Experiments

In order to analyse the jets velocity fields, Particle Image Velocimetry (PIV) experiments were carried out. PIV is used to obtain information about the mean and fluctuating velocity fields. The PIV system consisted in a laser Quantel Twins Ultra *30mJ*, type Nd-YAG, with a *532 nm* wavelength and a pulse duration of 7*ns* yielding *1mm* light sheet thickness. The images were acquired by an Image Pro *4M* camera with *2048 x 2048* pixels resolution equipped

with a Tokina ATX Pro *100mm* lens and f/4 aperture (f-stop). The fig. 2.5 shows a picture of the PIV system used in the experiments. The flow was seeded with oil particles, which have a maximum diameter of 1 µm, generated by an atomizer aerosol generator ATM 210 (TOPAS). The particles must be small enough to follow the flow and large enough to scatter light (Prasad, 2000). Melling (1997) pointed out that particle diameters of about 1 µm or smaller may ensure acceptable flow tracking for turbulent and high-speed flows. In order to ensure if the diameter of the particles employed in this study is correct, we calculate the settling velocity and the relaxation time:

$$u_\infty = \frac{g d_p^2 (\rho_p - \rho_f)}{18\mu} \qquad \text{eq. 2.2}$$

$$\tau_s = \frac{d_p^2 \rho_p}{18\mu} \qquad \text{eq. 2.3}$$

where g is the gravity acceleration, d_p and ρ_p are the diameter and density of the particles, respectively, and µ and ρ_f are the fluid viscosity and density, respectively. If these parameters are negligible compared to the flow scales it means that the particle is able to follow the flow and adapt to abrupt fluctuations. The values calculated were of the order of mm/s for the settling velocity and 5 µs for relaxation time, both much smaller than the flows scales.

Figure 2. 5: PIV system

The analysed jet conditions are depicted in the table 2.2. A set of 2000 snapshots was acquired for each jet condition. The interframe time was set to 1µs, providing a particle displacement of about 15 pix. The acquisition frequency of *7Hz* was employed between images pairs that again did not allow time resolved analysis. In order to analyse the accuracy of the measurements, an evaluation of the convergence was carried out, as can be seen in fig. 2.6, for *Mj=1.5* generated by thick lip. The point evaluated is located inside of the mixing layer, close to the first shock reflexion. In fig. 2.6 are depicted the mean values $\overline{u}$ and $\overline{v}$ as well as the *rms* of the fluctuations $\sigma_u = \sqrt{\overline{u'^2}}$ and $\sigma_v = \sqrt{\overline{v'^2}}$. We remark that acceptable convergence is reached with 1000 snapshots. For this reason, the number of samples employed in this work (2000 snapshots) is suitable to perform the study. Similar results were found for other *Mj* conditions.

Table 2.2: analysed jet conditions by PIV technique.

Thin Lip Nozzle(Mj)	*Thick Lip Nozzle(Mj)*
1.13	*1.13*
1.33	*1.33*
1.5	*1.50 B and C modes*
1.61	*1.61*
1.76	*1.76*

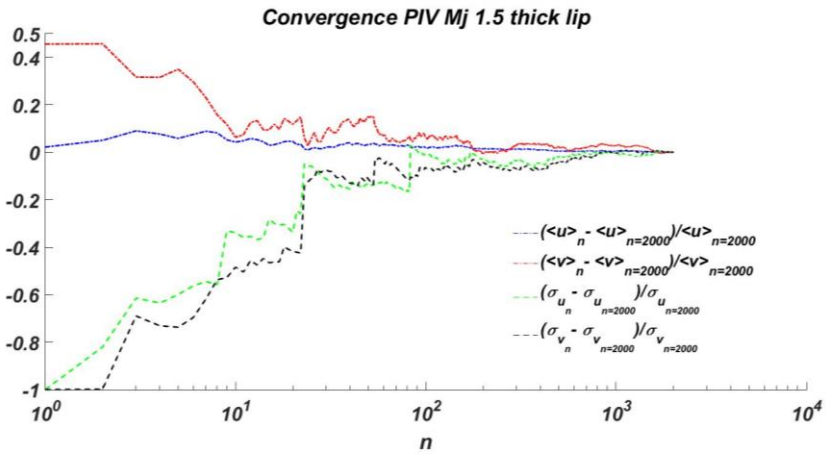

Figure 2. 6: statistic convergence of the PIV data. *Mj=1.5* thick lip *B* mode.

The images processing was performed by DaVis software where two calculation settings were employed. In the first one, the cross-correlation was performed on a *GPU* (Graphic Processing Unit) with initial interrogation window size of 32 pixels that was reduced to a final window of 8 pixels, employing 50% overlap. This processing provides a high-speed time for vector field calculation. However, its drawback consisted in a noticeable number of spurious vectors which were eliminated in the post-processing task and no considered in the study. The fig. 2.7 shows the ratio between these vectors and the total sample size (*number of SV /2000*) for the jet generated by the thick lip, at *Mj=1.5* and under dominant flapping mode *B*. One can observe that the number of the snapshots that presented spurious vectors was less than 5% of the total number of snapshots. The chapter 3 and 4 of this work are performed from the results of this processing.

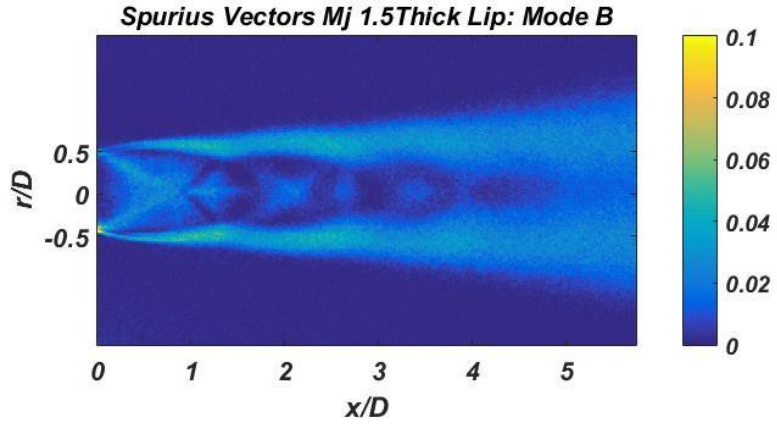

Figure 2. 7: ratio between number of the spurious vectors and total sample size. *Mj=1.5*, thick lip dominant flapping mode *B*.

The second processing was carried out on a *CPU* (Central Processing Unit) with initial interrogation window size of 32 pixels that was reduced to a final window of 16 pixels, employing 50% overlap. The advantage of this processing is that it provides better results concerning the spurious vectors, however the calculation time is slower than using *GPU*. The chapter 5 of this work employs the results generated by this processing. The PIV parameters for both processing are summarized in the table 2.3. It is worth to mention that no noticeable difference was found between the results provided by the two PIV processings in the fluctuations and mean fields. This is showed in fig. 2.8 which presents the result of the two processing for longitudinal mean velocity (*U*), normalized by U_e (jet velocity at the nozzle exit), for the jet at *Mj =1.13* and generated by thick lip nozzle.

Table 2.3: summarized PIV parameters.

PIV PARAMETERS		
PARAMETER	*VALUE*	*NON-DIMENSIONAL VALUE*
IW_O	*32 pixels*	*0.43D*
IW_1	*16 pixels| 8 pixels*	*0.22D|0.11D*
Light Sheet Thickness	*1.0 mm*	*0.1D*
Δt	*1μs*	-
Field of View	*63 mm x 40 mm*	*6.3D x 4D*

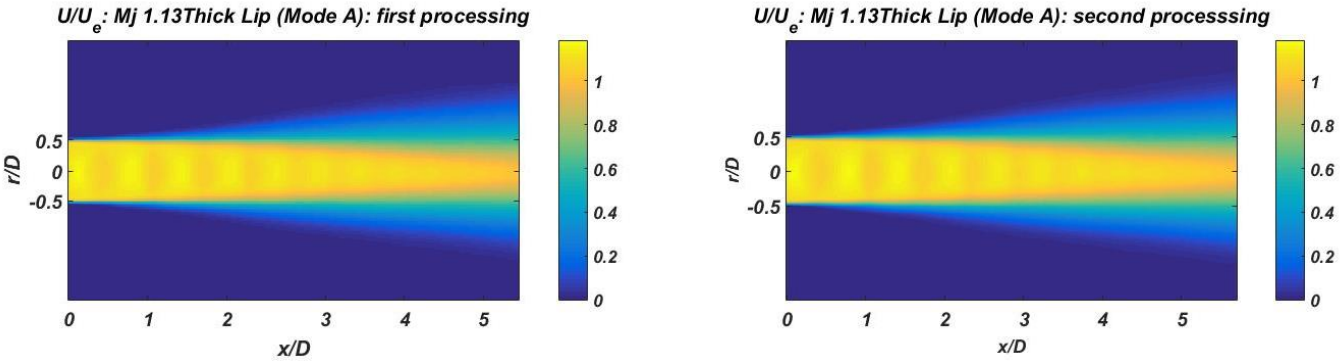

Figure 2. 8: longitudinal mean velocity (*U*) normalized by *Ue* for *Mj=1.13*. *GPU* (left) and *CPU* processing (right).

Before analysing the velocity fields it was necessary to evaluate whether the particles influence, in any way, the Screech phenomenon (modes or frequency changes). A study about the particle effect was carried out to analyse the noise spectrum of the jet with and without seeding for each M_j analysed. The result for *Mj=1.13* is depicted in fig. 2.9 and it shows clearly that no particle effect is noticeable in the acoustic spectrum. The same result was observed for all *Mj*, ensuring that seeding had no effect on the Screech.

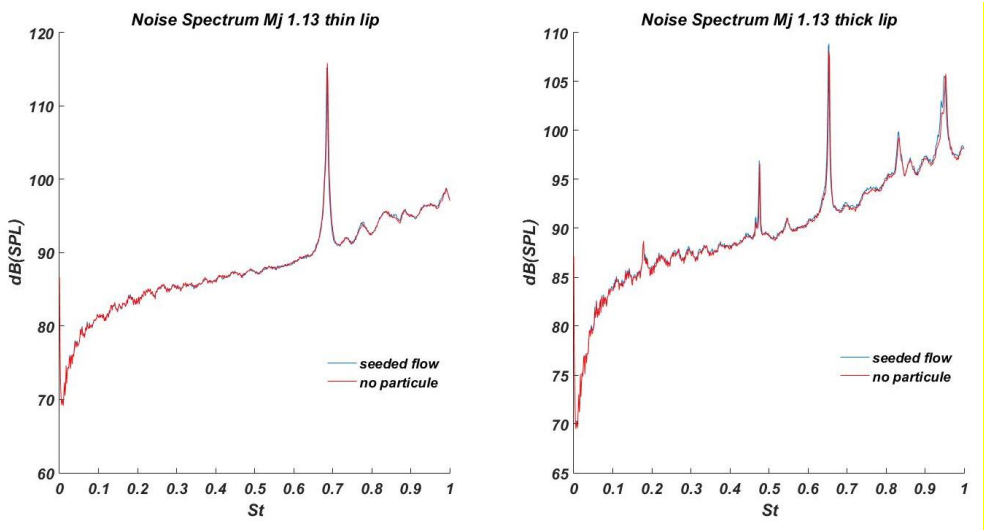

Figure 2. 9: particle effect in the noise spectrum for *Mj=1.13*, thin (left) and thick (right) lip nozzle.

2.5 POD analysis

The paramount role that large coherent structures have in the Screech phenomenon, interacting with shock-cells and generating the upstream acoustic wave is well known. Thus, evaluating these structures as a function of the nozzle geometry and flow conditions may provide meaningful information. For this purpose POD (Proper Orthogonal Decomposition) is employed in this work. POD is a tool that allows to obtain information about coherent and energetic structures contained in the flow field. As such, it is able to extract the coherent fluctuations associated with the Screech.

The pioneer in applying POD for structures identification in turbulent flows is Lumley (1967) and applications for round jets were demonstrated by Glauser & George (1987a,b). Although mathematically POD does not provide what the modes represent in a physical sense, it is assumed that the most energetic modes are associated with reiterated fluctuations generated from large scale coherent structures of the flow (Berkooz *et al*. 1993). POD was employed on Schlieren data in a recent work by Berry *et al.* (2017) to analyse supersonic multi-stream rectangular jets. Furthermore, Jaunet *et al.* (2016) used POD for convection velocity estimation in a supersonic jet. Edgington-Mitchell *et al*., (2014a,b) employed the technique to evaluate the Mach disk of underexpanded jets and to analyse the link between coherent structures and sound production in the axisymmetric screeching jets under helical mode. A brief description of the technique is provided and a more complete discussion about POD can be found in Sirovich's (1987).

POD is a method that finds optimal basis functions by identifying the structures with largest mean square projection. The POD is an eigenvalue problem with spatial (*classical POD*) or temporal (*Snapshot POD*) correlation tensors. For a given spatiotemporal field *g(x,t)*, which can be a scalar (in the case of the Schlieren analysis) or a vector field (for PIV data), the decomposition is defined as:

$$g(x,t) = \sum_{n=1}^{N} a^{(n)}(t)\Phi^{(n)}(x) \qquad \text{eq. 2.4}$$

where $\Phi^{(n)}(x)$ is the n^{th} eigenfunction (spatial mode), $a^{(n)}(t)$ represents the n^{th} eigenvector (temporal coefficient) and *N* is the database size. By definition the eigenfunctions $\Phi^{(n)}(x)$ are orthonormal (orthogonal and of unit length), hence:

$$\left((\Phi^{(n)}(x), \Phi^{(m)}(x)\right) = \delta_{nm} \qquad \text{eq. 2.5}$$

where (,) represents the scalar product and $\delta_{nm}$is equal to 1 only if n=m. The temporal coefficients $a^{(n)}(t)$ are orthogonal to each other, thus:

$$\langle a^{(n)}(t).a^{(m)}(t)\rangle = \lambda^n \delta_{nm} \qquad \text{eq. 2.6}$$

where $\langle\,.\,\rangle$ represents the ensemble average and λ^n is the n^{th} eigenvalues.

Thus, POD is applied to PIV data to evaluate the nozzle lip thickness effect on the flow structures (chapter 3) as well as the link between Screech modes and the coherent structures (chapter 4). In addition, the technique is employed in the investigation of the upstream-travelling waves, subject of the chapter 5.

Finally, the experiments and techniques showed in this chapter allow us to evaluate the Screech phenomenon, where the results are presented soon of this work. We start with the analyse of the nozzle thickness effect on the underexpanded screeching jets, subject of the next chapter.

3 NOZZLE LIP THICKNESS EFFECTS

This chapter presents how the acoustics, the topology and the coherent structures are influenced by the nozzle lip thickness. We aim to show the influence of the lip on both, the far-field pressure spectrum and the azimuthal Fourier modes of the near-field pressure, focusing on the Screech tones. Schlieren images and PIV data are used to investigate the nozzle lip thickness effect on the flow topology and turbulence characteristics. Moreover, the effect of the lip thickness on the standing wavelength, which results from an hydrodynamic/acoustic wave interaction, is evaluated. Finally, the coherent structures are investigated via correlation and POD analysis.

3.1 Acoustics

This section presents the acoustics differences between the nozzles, analysing the far-field pressure spectrum as well as the resuts of the azimuthal Fourier decomposition performed from the near-field pressure spectrum data.

3.1.1 Far-Field Screech Noise

The far-field acoustic spectrum is plotted in a cartography as a function of the Strouhal number ($St = \frac{f_s D_j}{U_j}$) and the fully expanded jet Mach number (*Mj)*, in the fig. 3.1, for both the thick and the thin lip nozzles. The Strouhal number is defined as a function of the perfectly expanded velocity and diameter of the jet, U_j and D_j respectively. We can notice that both jets present the Screech modes *A1*, *A2*, *B*, *C* and *D*, as indicated in fig. 3.1. As mentioned, we see that the transition from the axisymmetric mode (*A2*) to the flapping one (*B*) is abrupt, represented by a noticeable fall in the Screech frequency. Moreover, it is possible to observe the general tendency of the Strouhal number (frequency) decreases as *Mj* increases, characterizing a typical Screech curve. This behaviour is explained by the increase of the shock-cell length as *Mj* increases, leading to a frequency reduction. An exception of this behaviour appears during the shift of the mode *B* to *C*, where we can observe a frequency augmentation.

Concerning the thin lip nozzle, in the fig. 3.1, one can see that the jet at *Mj=1.5* presents a coexistence of *B* and *C* Screech modes, where it is clear that the former is the dominant tone and the latter is the secondary one. In the same figure, it is not possible to identify Screech for M_j larger than *1.7*, for the jet generated by this nozzle.

Considering the thick lip nozzle, the figure shows that, contrary to the thin lip case, the Screech tones are visible beyond M_j =1.7. This nozzle effect is known as Screech reactivation (Raman, 1997). The same figure shows, as expected, that the thick nozzle causes modal changes in the jet flow (Ponton & Seiner, 1992 and Weightman *et al*., 2017), as can be seen by the early transition between the Screech *B* mode to the *C* one. Furthermore, the thick lip nozzle seems to generate single modes: no sign of the coexistence of *B*-*C* modes is visible in the cartography. In other words, it is not possible to notice the coexistence of *B* and *C* modes between M_j *1.4* and *1.64*, in contrast to the thin lip nozzle. Due to Screech directivity issues (microphone position), the first harmonic appears more energetic than the fundamental frequency of the phenomenon (Powell, 1953a).

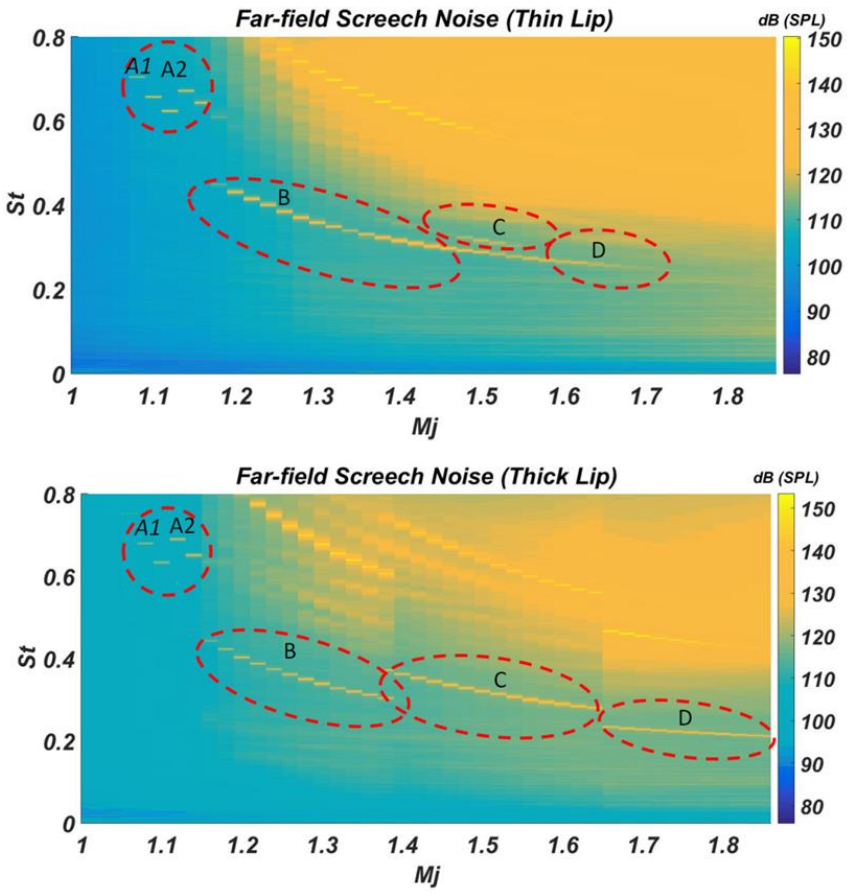

Figure 3. 1: cartography of the PSD of far-field noise of the screeching jets generated by thin (top) and thick (botton) lip nozzle.

In order to evaluate the differences between the far-field noise spectrum generated by these nozzles, the two cartographies are plotted on top to each other in fig. 3.2. As can be seen, the Screech frequency is affected by the nozzle lip thickness for the *A1*, *A2* and *B* modes: the thin lip nozzle presents higher frequencies than the thick one, agreeing with the literature (Ponton & Seiner, 1992). On the contrary, the helical *C* mode presents almost the same Strouhal number, regardless of the lip thickness. This result does not agree with Ponton & Seiner (1992) who observed that the *C* mode is also affected by the nozzle lip thickness, increasing the frequency as the lip thickness increases. Moreover, from fig. 3.2, it is possible to observe that the helical *C* mode has a larger extension for the jet generated by the thick lip than by the thin one.

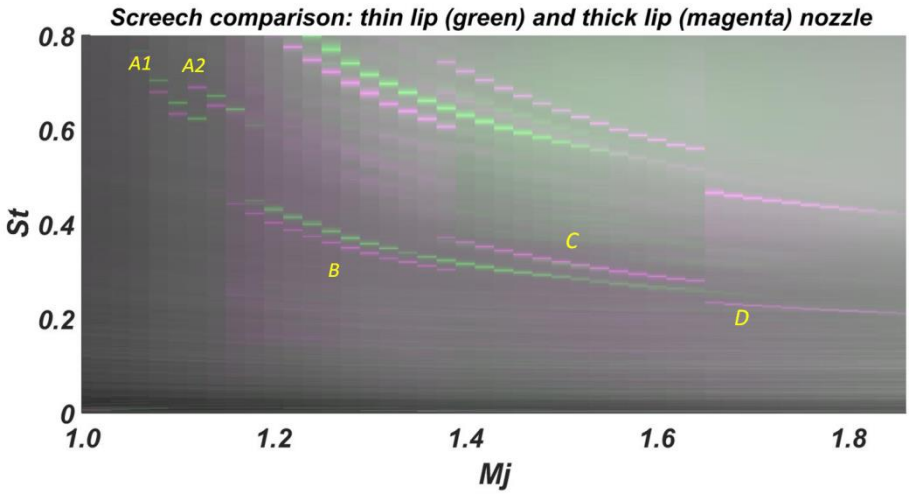

Figure 3. 2: comparison between far-field pressure spectrum generated by two different nozzles: thick lip (magenta) and thin one (green).

3.1.2 Relation Between Screech and Azimuthal Fourier Modes

The *PSD* (Power Spectral Density) of the two first azimuthal (*m=0* and *m=1*) Fourier modes of the near-field pressure are shown in the figs. 3.3-3.4, for the thin and thick lip nozzles, respectively. One can notice in the fig. 3.3 that, contrary to what can be seen in far-field, the signature of the *A2* mode can be tracked for a wider range of *Mj* in the near-field, although its strongest amplitude is seen at lower *Mj*. This result provides an additional experimental "convincing evidence" to the work of Powell *et al*. (1992) where the authors suggested that the unidentified mode *u* is a *A2* mode extension, as already mentioned in the chapter 1 (see fig. 1.16). A Similar conclusion for this "unidentified" mode was obtained numerically by Gojon *et al*. (2018). Moreover, concerning the lip thickness effects, we can notice that the signature of the *A2* mode is much more remarkable for the jet generated by the thin lip nozzle than by the thick one. It suggests that the thin lip nozzle generates jets that improve the support of this axisymmetric mode.

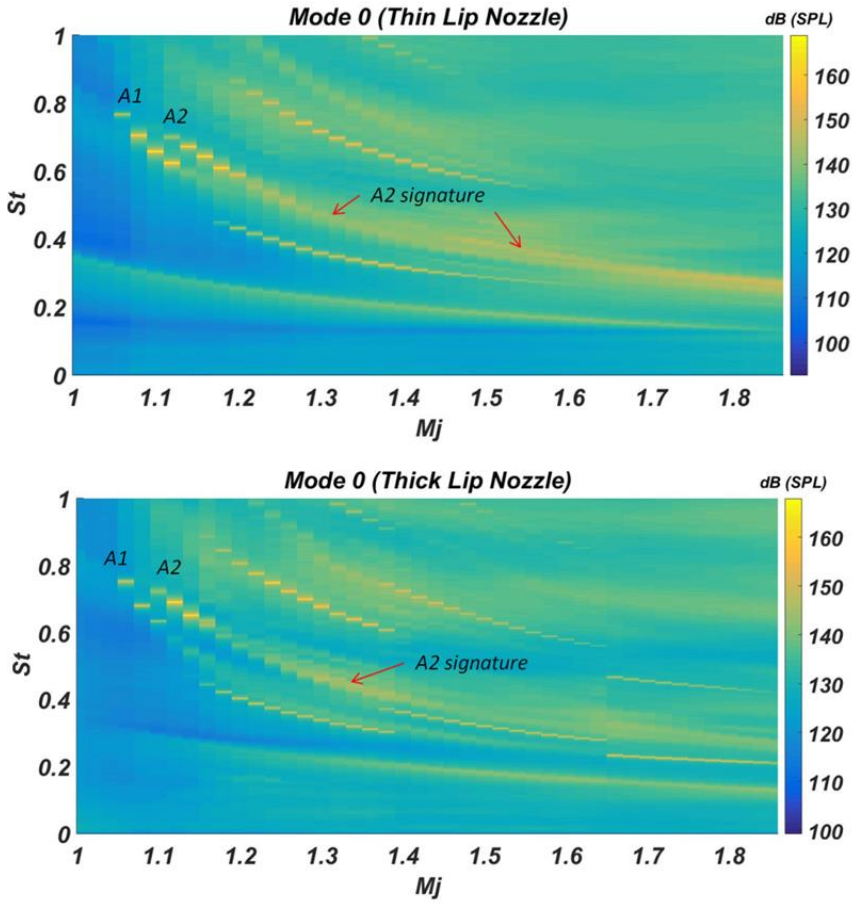

Figure 3. 3: cartography of the PSD of the first azimuthal mode (*m=0*) of the near-field pressure as a function of *St* number and *Mj*. Effect of the nozzle lip on *A1/A2* Screech modes: thin (top) and thick lip (bottom).

The results for the azimuthal mode *1* are presented in fig. 3.4. One can observe that, for both nozzles, there is no sign of flapping *B* mode in the range of *Mj* conditions where the axisymmetric modes *A1* and *A2* are dominant. In the thin lip case, contrary to what can be observed in the far-field, the flapping mode *B* signature can be tracked until M_j *=1.86*. Interesting results are obtained in the thick lip case: one can see that the *B* mode always exists in the near-field, although in the far-field spectrum it is not possible to notice it. The flapping mode *B* coexists with the helical *C* one and extends up to M_j *1.86*. Furthermore, the strongest amplitude of the helical *C* mode is obtained for a narrow range of M_j conditions in the thin lip case (*1.35<Mj<1.58*, approximately) while in a wider range for the thick one (*1.32<Mj<1.65*, approximately).

Finally, we have shown that near-field measurements allow to obtain the signature of the non-dominant Screech modes that do not strongly radiate in the acoustic far-field. These observations permit to conjecture that there seem to be no physical sense classifying the Screech tones in other modes as *D*, *E* and *F* (Powell, 1953a, Panda *et al*.,1997 and Clem *et al*. 2012) due to the fact that these ones are either flapping *B* mode extension (Edgington-Mitchell *et al*., 2015) or helical *C* mode reactivation. However, this is not so clear in the thin lip case at high *Mj*.

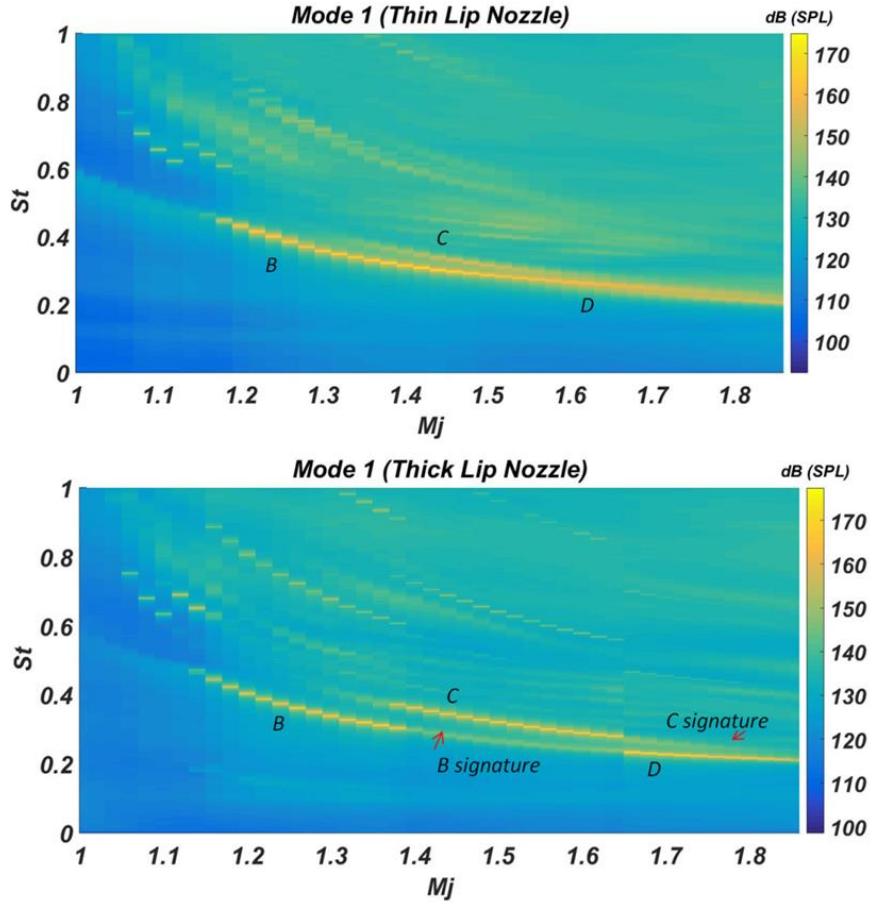

Figure 3. 4: cartography of the PSD of the first azimuthal mode (*m=1*) of the near-field pressure as a function of St number and *Mj*. Effect of the nozzle lip on *B/C/D* Screech modes: thin (top) and thick lip (bottom).

3.1.3 Conclusion

We have noticed that the thick lip nozzle provides modal changes in the flow compared to the thin one, causing an early transition between the *B* and the *C* Screech modes, and leading to a wide range of M_j conditions where the helical *C* mode can exist. Moreover, concerning the *A1*, *A2* and *B* modes, the thin lip generates jets with Screech frequencies higher than the thick one, agreeing with Ponton & Seiner (1992). However, we did not remark difference in the Screech frequency for the helical *C* mode.

The near-field pressure observation confirms that the axisymmetric mode *A2* can be tracked for a large range of M_j conditions, although its amplitude is higher at low *Mj*. Moreover, the signature of the mode *A2* is more pronounced for the jet generated by the thin lip nozzle than by the thick one, indicating that the former improves the support for this axisymmetric Screech mode. The jet under axisymmetric dominant Screech modes does not present other tones, neither corresponding to flapping *B* mode nor to helical *C* one. Furthermore, it was possible to notice that the flapping *B* and helical *C* modes coexist in the near-field, in certain ranges of *Mj*, for both nozzles. Finally, the near-field results suggest that classifying the Screech modes in *D*, *E* and *F* represents more a nomenclature issue than a physical sense, due to the fact these modes are either flapping *B* mode extension or helical *C* mode reactivation. This behavour is not so clear in the thin lip case at high *Mj*, maybe due to modes interaction.

3.2 Flow Topology

In this section, we analyse the lip thickness effect on the general flow topology of the jets. These effects are presented on the average shock-cell spacing and the standing wavelength, using instantaneous Schlieren images and PIV data. The effect on the mixing layer spreading rate and turbulence levels is also presented. Although the thick lip naturally provides a dominant *C* Screech mode at *Mj = 1.5*, it is possible to make it switch artificially to the *B* one by the introduction of a pertubation in the flow. The switched configuration then stays active continuously. In other words, the thick lip nozzle is able to provide distinct flows, with different dominant tonal modes, for the same *Mj=1.5*. This ability is used with the purpose to isolate the effects of the lip thickness from the Screech mode effects. Hence, the jet at *Mj=1.5* under flapping *B* dominant mode will be analysed in this section instead of the one under helical *C* instability.

3.2.1 Average Flow Topology and Shock-Cell Spacing

In order to determine the average shock-cell spacing, we employ a set of 1000 Schlieren images, for each jet condition. From this set of data, the average density gradient maps are obtained, as can be seen in fig. 3.5, for the jet at *Mj=1.5* and both nozzles. In this figure, the axial coordinate (*x/D*) represents the position of the measured shock-cells. As can be seen, the shock-cell length is very similar for both nozzles. The 4th shock-cell, in the thick lip case, is barely visible contrary to the thin one. This may indicate a high oscillation level and/or a large mixing layer thickness for the jet generated by the thick lip nozzle. Due to these experimental limitations, it was not possible to determine all the shock-cell lengths for each *Mj* condition, thus this study used a maximum of 4 shock-cells to calculate the average shock-cell length. We report the average shock-cell spacing (L_s) in fig. 3.6 as well as a comparison with Prandtl-Pack and Gao & Li estimations.

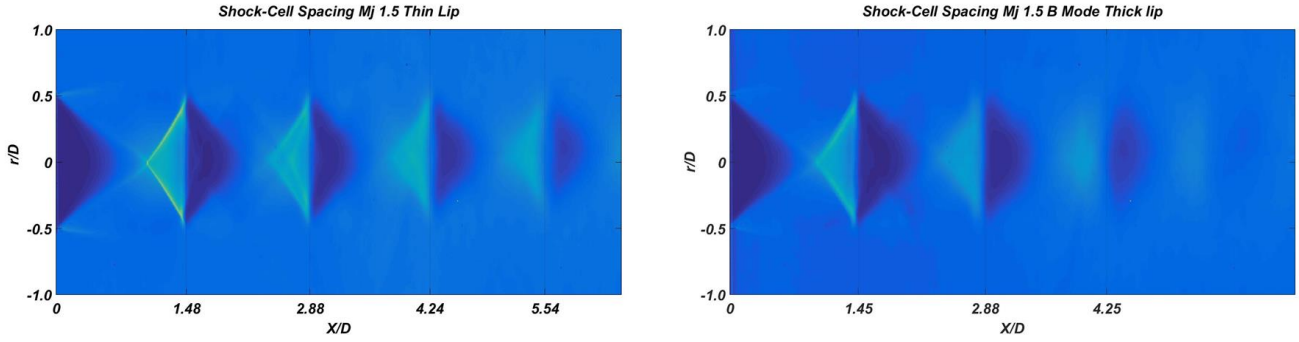

Figure 3. 5: mean density gradient fields for *Mj= 1.5*, thin (left) and thick lip (right). Shock-cell length represented in axial coordinate.

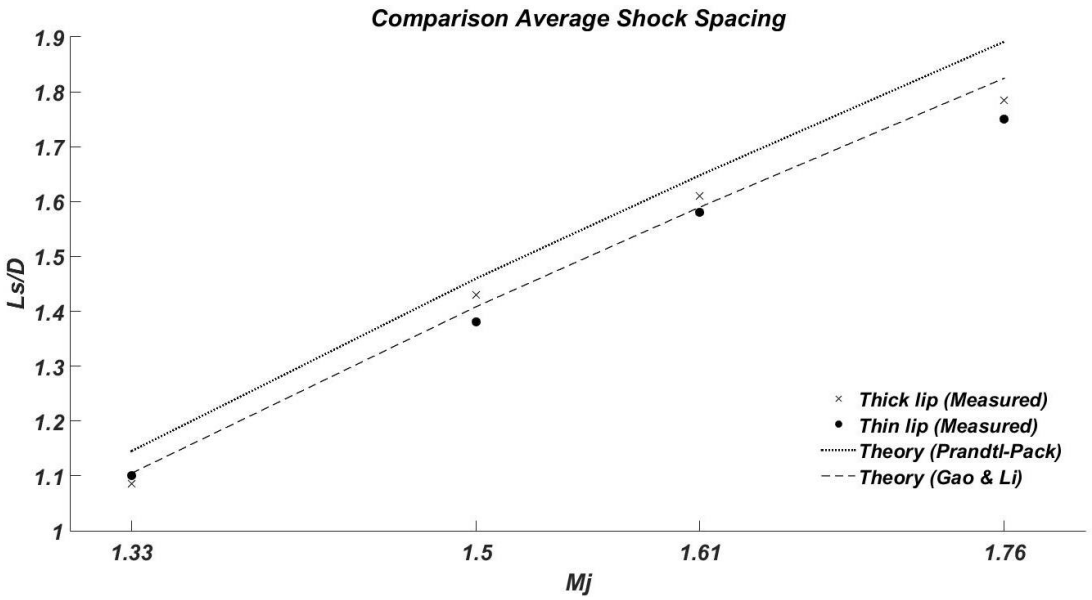

Figure 3. 6: average shock-cell spacing. Comparison between theory and experimental data

Overall, analysing the fig. 3.6 it is possible to observe that the thin lip nozzle provides slightly smaller shock-cell length compared to the thick one. This result is consistent with the fact that Screech frequencies are slightly higher for the jets generated by the thin lip nozzle, as observed in the acoustic section. Moreover, as M_j increases, the difference between experimental data and Prandt-Pack vortex-sheet theory increases, a behaviour that has already been documented by other authors (Munday *et al*. ,2011, Heeb *et al.* ,2014b, and Tam *et al.*, 1986). This discrepancy is due to the effects of the enlargement of the mixing layer in the real flow conditions, contrary to assumptions of the model (infinitely thin layer). As such, the model correctly predicts lower *Mj* conditions as well as it still remains valid close to the lip, where the shear layer is thin, but loses accuracy further downstream.

3.2.2 Standing Wavelength

As we have instantaneous Schlieren images, it is possible to obtain the grey level fluctuations. The *rms* values of grey level fluctuations for *Mj=1.33* and both nozzles can be seen in figs. 3.7. The image shows an interesting feature: the jet generated by the thick lip nozzle seems to spread out more importantly than the thin lip one. In other words, it seems that the thick lip increases the jet spread. This is consistent with what can be found in rectangular jets: the strength of oscillations increases with the lip thickness, with no noticeable changes beyond a thickness greater than *1.0D* (Raman, 1998). Moreover, as can be seen from the *rms* spread out, the first shock-cell is more stable than the other ones regardless the nozzle (Panda, 1998 and André *et al.*, 2011). It is also possible to notice in fig. 3.7 that the near-field presents lobes fluctuations levels. They are due to standing waves formation (Panda, 1999, Edgington-Mitchell *et al.*, 2015 and Gojon *et al.*, 2018). These structures are also visible in the near-field of the velocity fluctuations, as can be seen in fig. 3.8 for the jet at *Mj=1.33*.

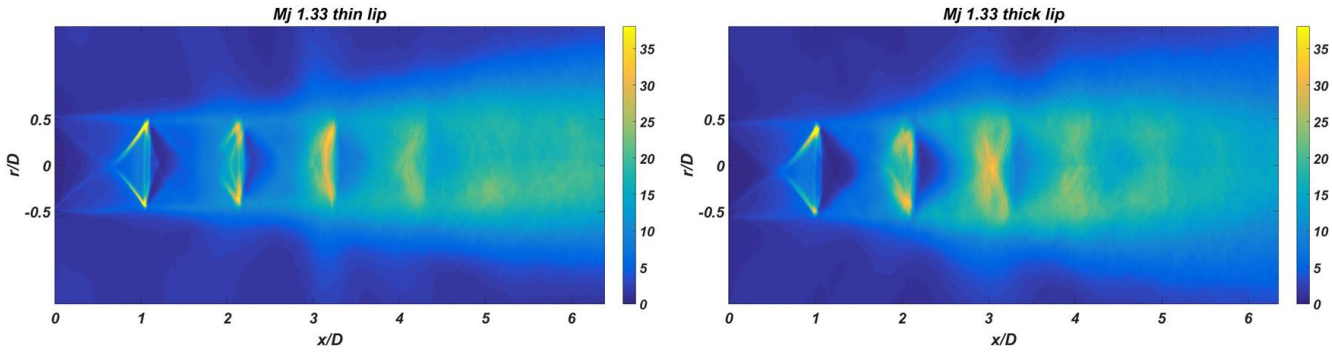

Figure 3. 7: *rms* of grey level fluctuations of the jet at *Mj=1.33*. Thin (left) and thick lip (right) nozzles.

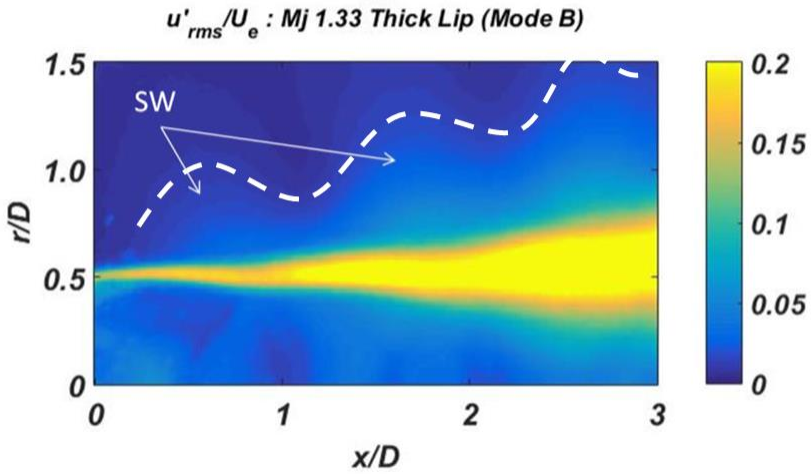

Figure 3. 8: longitudinal *rms* velocity fluctuation (u'_{rms}) normalized by *Ue* and standing waves (SW) identification. Jet at *Mj = 1.33* generated by the thick lip nozzle.

The formation of the standing wave is a result of hydrodynamic/acoustic wave interaction. Panda (1999) measured the standing wavelength from the pressure fluctuations in the near-field of the jet. We measure this length from the *rms* of the velocity fluctuations and the results are depicted in fig. 3.9. Unfortunately, for *Mj = 1.61* and *1.76* it was not possible to track the standing waves signature. Therefore, we focus on *Mj=1.13*, *1.3*3 and *1.5*.

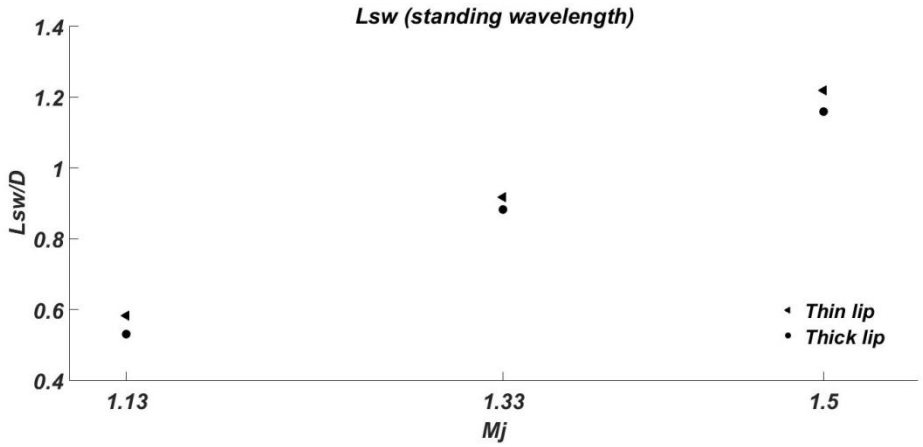

Figure 3. 9: comparison of the standing wavelength for the thin and thick nozzle

We report on the fig. 3.9 the length of the standing waves measured (L_{sw}) for both nozzles. We can observe that overall the standing wavelength for the thin lip is slightly larger than for the thick one. This result is interesting as it may be the signature that the thin lip produces smaller convective vortices (with larger velocity) (Panda, 2006), leading to an increase in the standing wavelength (see eqs. 1.26-1.28). Thus, the velocity of these vortices can explain the differences in the Screech frequencies previously observed.

Finally, comparing the standing wavelength and the average shock-cell spacing for *Mj=1.33* and *1.5*, we obtain the ratio $L_{sw}/L_s \approx 80\%$, the same value reported by Panda (1999) and employed by Tam et al. (1986) for the adjustment of their Screech estimation model.

3.2.3 Mean Velocity Fields

We present here the results obtained with the PIV measurements. The longitudinal mean velocity fields, normalized by U_e (jet velocity at the nozzle exit) are depicted in figs. 3.10-3.12, for the jets at *Mj=1.33*, *1.5* and *1.61*, respectively. In fig. 3.10, for a Mach number $M_j=1.33$, one can remark that the spreading of the jet issued from the thick lip nozzle is larger than the thin lip case. Although less pronounced, this effect is also noticed in the jet at *Mj=1.5* (fig. *3.11*). Moreover, observing the fig. 3.12 ($M_j=1.61$) one can see the Mach disk influence in the flow topology, leading to a subsonic region inside of the jet core. Another effect that may be observed is that the initial mixing layer curvature increases as M_j increases due to the intensification of underexpansion levels (Lehnasch, 2005 and André *et al*. 2014).

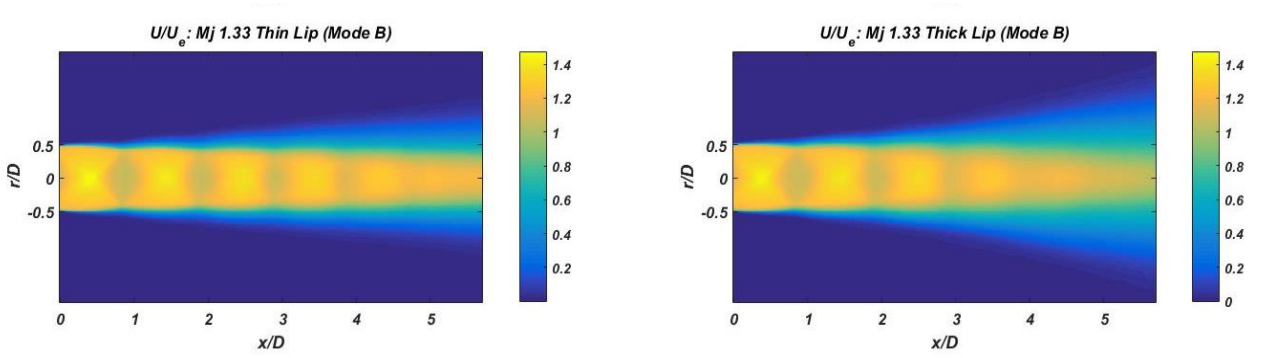

Figure 3. 10: longitudinal mean velocity (*U*) normalized by *Ue* for *Mj=1.33*. Thin (left) and thick (right) lip nozzles.

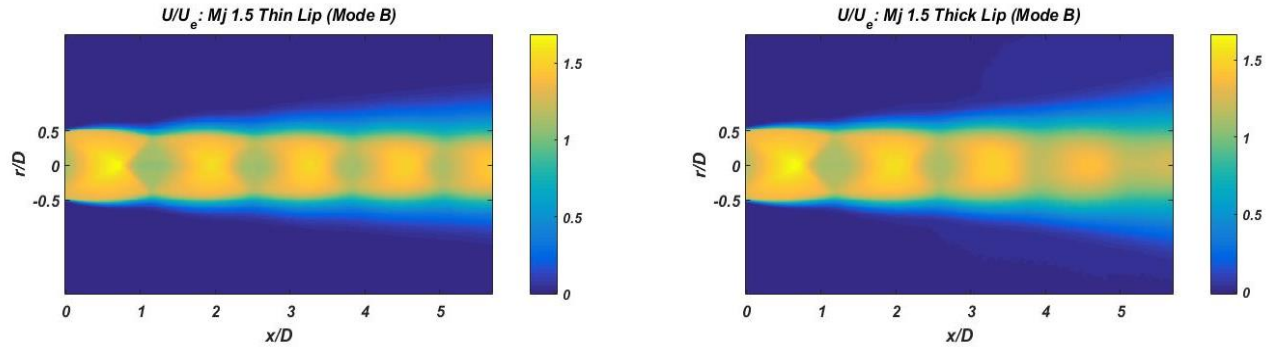

Figure 3. 11: longitudinal mean velocity (*U*) normalized by *Ue* for *Mj = 1.5*. Thin (left) and thick (right) lip nozzles.

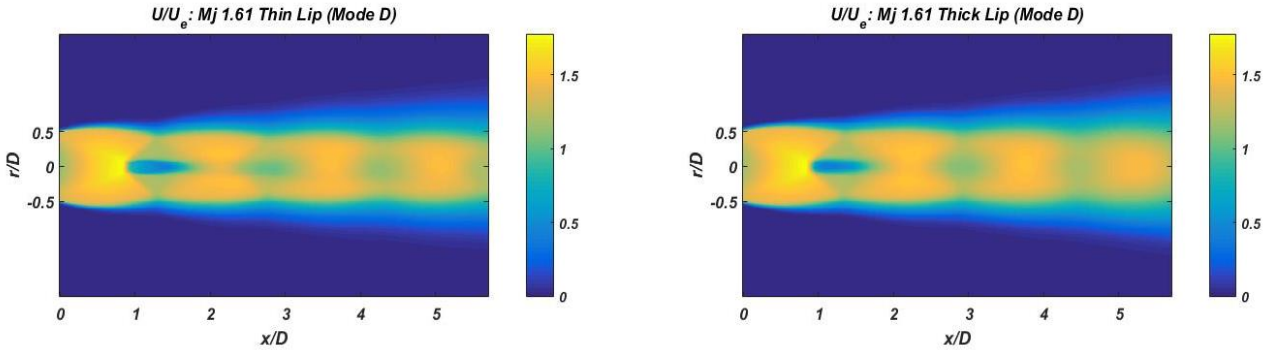

Figure 3. 12: longitudinal mean velocity (*U*) normalized by *Ue* for *Mj = 1.61*. Thin (left) and thick (right) lip nozzles.

The mean axial velocity profile, for *Mj=1.33*, is plotted in fig. 3.13. We can observe that there is no large difference in the shock-cell length for the flows generated by the thick lip or thin one, agreeing with previous observations. It is possible to remark that the maximum velocity at the jet axis are larger for the thin lip than for the thick one. Moreover, we can notice that, from *x/D=4.0*, the sock-cell structure begins to collapse for the thick lip nozzle. This observation may be linked to the fact that the thick lip nozzle generates jets with a larger spreading rate of the mixing layer than the thin one. Indeed, the evolution of the mixing layer acts to decrease the potential core length, subsequently minimizing the number of shock-cells.

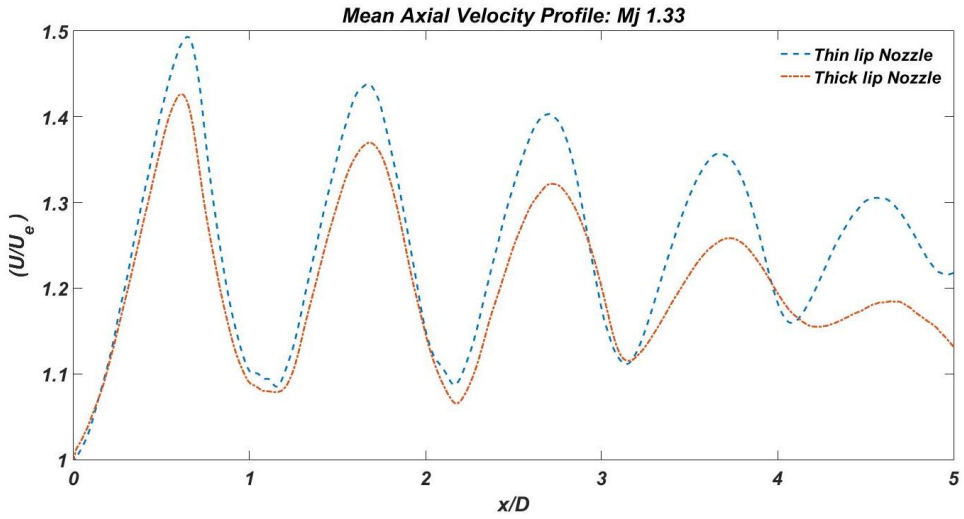

Figure 3. 13: mean axial velocity profile normalized by *Ue* for *Mj=1.33*.

From the mean velocity fields results a study of the nozzle lip effect on the mixing layer spreading rate is carried out. We analyse the evolution of the mixing layer vorticity thickness, defined as:

$$\delta_\omega = \frac{\Delta U}{\left(\frac{\partial U}{\partial y}\right)_{max}} \qquad \text{eq. 3.1}$$

where $\left(\frac{\partial U}{\partial y}\right)_{max}$ is the maximum velocity gradient measured in the velocity profile. We plot in the fig. 3.14 the vorticity thickness evolution for the jets at *Mj =1.33*. As expected from the literature (Ponton & Seiner, 1992 and Kim & Lee, 2007) and from our previous results, the thick lip produces mixing layers thicker than the thin one. Similar results were observed for all *Mj* conditions considered.

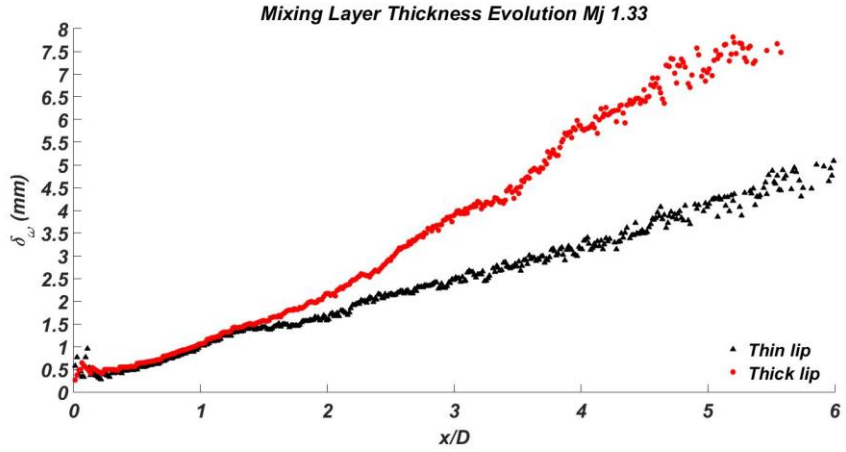

Figure 3. 14: mixing layer vorticity thickness evolution *Mj = 1.33*, thin and thick lip nozzle.

Applying a linear least squares regression it is possible to estimate the slope of each curve to obtain the mixing layer spreading rate ($d\delta_\omega/dx$), reported in fig. 3.15 as a function of the Mach number *Mj*. For all nozzles, one can see that the spreading rate of the mixing layer

decreases as *Mj* increases, except for the thick lip between *Mj=1.13* and *1.33*. This behaviour is due to compressibility effects on the spreading rate of the mixing layer (Papamoschou & Roshko, 1988). Overall, the thick lip tends to increase the jet spreading rate and it seems from fig. 3.15 that the increase amount depends on the jet Mach number and thus probably on the Screech mode. This lip thickness effect on the jet spreading was documented by Raman (1998) in the case of rectangular jets.

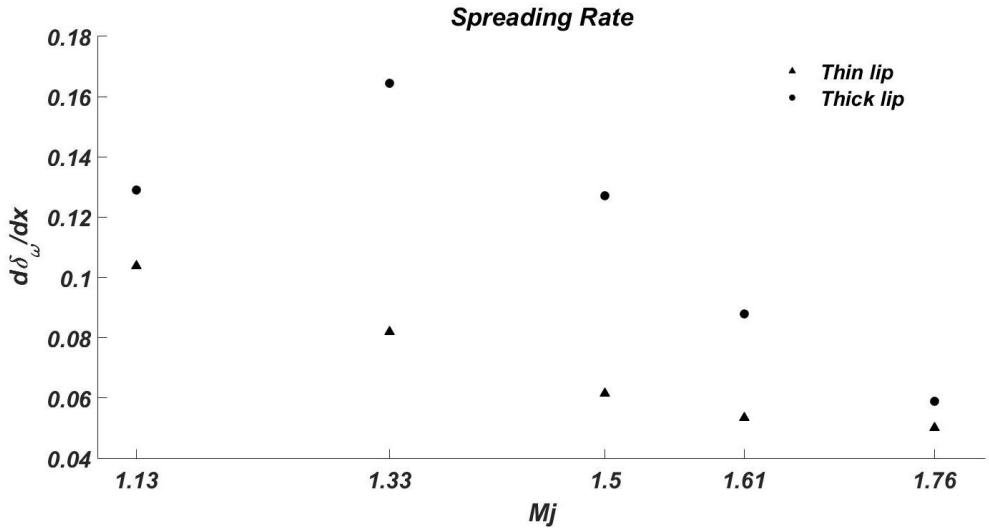

Figure 3. 15: spreading rate for all *Mj* conditions considered.

3.2.4 Velocity Fluctuation Fields

We observed in the previous section that the thick lip nozzle generates higher spreading rate and larger mixing layer thickness compared to the thin lip case. Now, we aim to investigate the influence of the lip thickness on the velocity fluctuations.

The lip thickness effect on the fluctuation velocity fields for *Mj =1.33*, *1.5* and *1.61* are presented in figs. *3.16-3.21*. These images present comparisons between normalized *rms* velocity fields generated by the two different nozzles operating at the same M_j. It is possible to notice in fig. 3.16 that the jets issued from the thick lip, at M_j*=1.33,* present higher longitudinal fluctuation levels than for the thin one. In the same figure, we can also remark that the flow generated by thin lip presents a remarkable modulation of longitudinal fluctuation levels caused by shocks reflexions in the mixing layer. Similar observations can be made for the jet at *Mj=1.5* (fig. 3.17). In the fig. 3.18 (*Mj=1.61*) we observe that these thickness lip effects are less pronounced than in the previous cases.

Considering the tranversal fluctuations, the figs. 3.19, 3.20 and 3.21 show similar behaviour of the longitudinal levels observed, for the *Mj=1.33*, *1.5* and *1.61*, respectively. Overall, the thick lip nozzle provides higher energetic levels on all the velocity components.

Finally, observing the images one can notice that it is easier to identify standing waves in the near-field of jets generated by the thick lip nozzle. This behaviour, as mentioned, is certainly related to the turbulence structures convected in the jet mixing layer: they are larger in the flow generated by the thick lip nozzle than by the thin one.

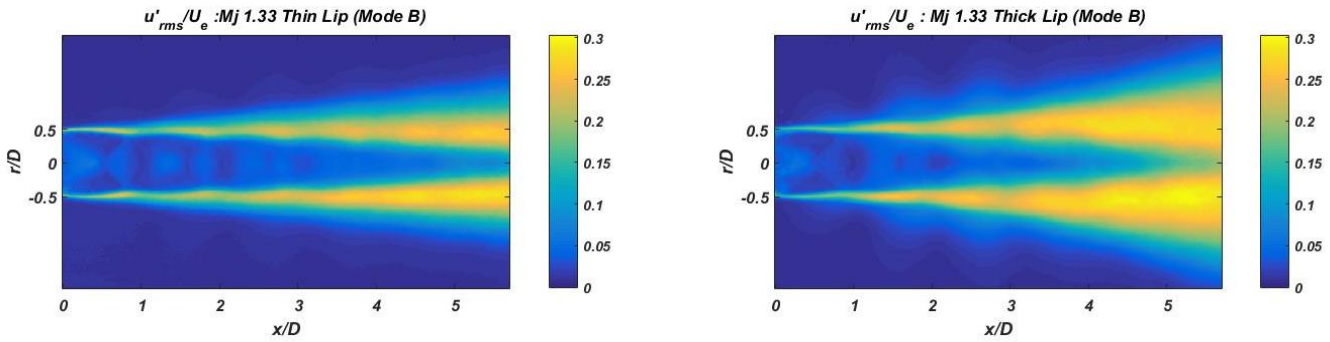

Figure 3. 16: longitudinal *rms* velocity fluctuation (u'_{rms}) normalized by *Ue* for *Mj=1.33*. Thin (left) and thick (right) lip nozzles.

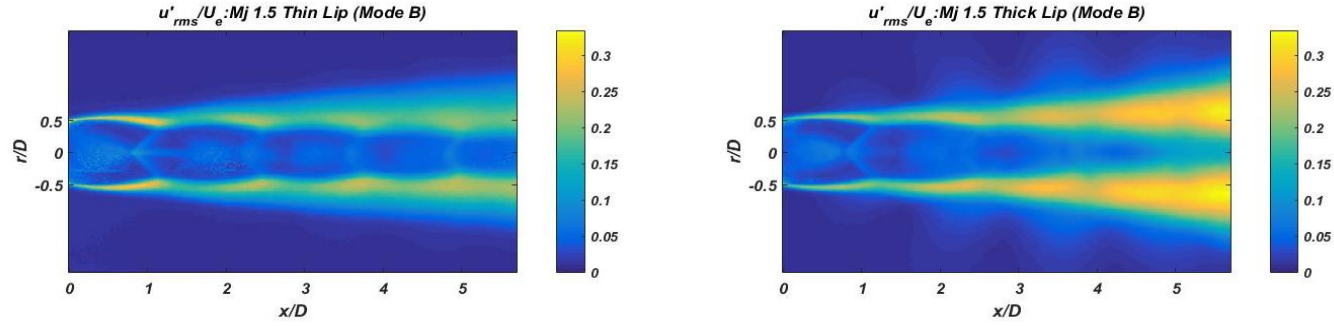

Figure 3. 17: longitudinal *rms* velocity fluctuation (u'_{rms}) normalized by *Ue* for *Mj = 1.5*. Thin (left) and thick (right) lip nozzles.

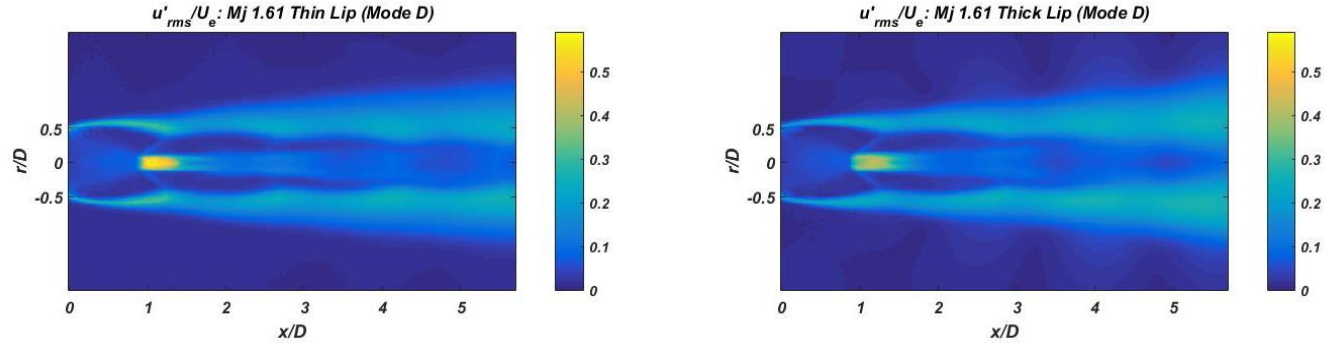

Figure 3. 18: longitudinal *rms* velocity fluctuation (u'_{rms}) normalized by *Ue* for *Mj=1.61*. Thin (left) and thick (right) lip nozzles.

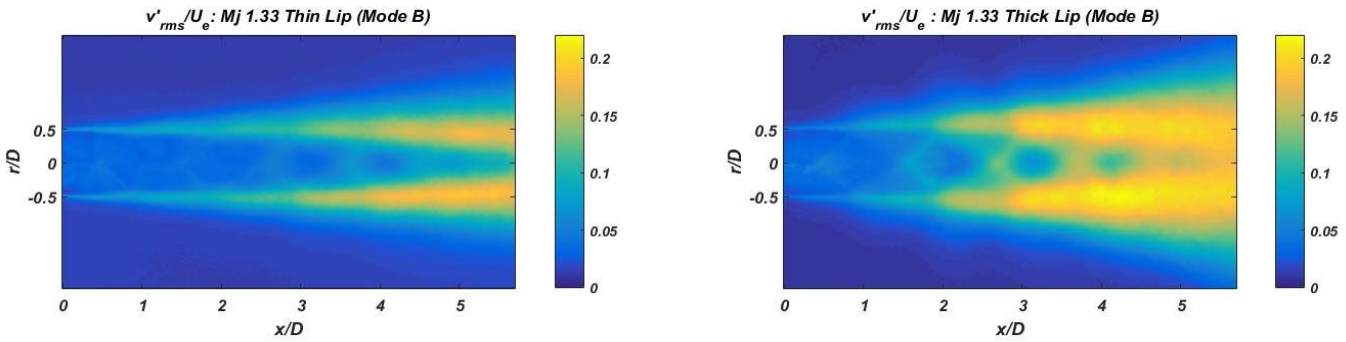

Figure 3. 19: transversal *rms* velocity fluctuation (v'_{rms}) normalized by *Ue* for *Mj = 1.33*. Thin (left) and thick (right) lip nozzles.

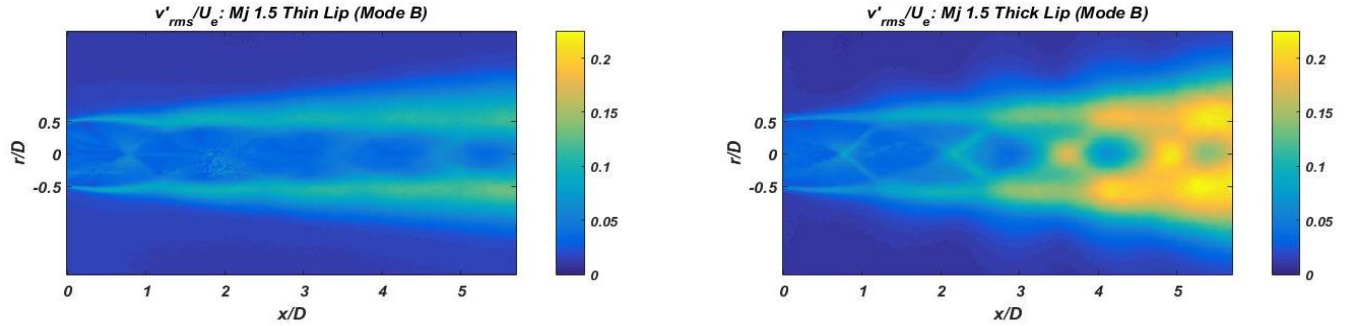

Figure 3. 20: transversal *rms* velocity fluctuation (v'_{rms}) normalized by *Ue* for *Mj =1.5*. Thin (left) and thick (right) lip nozzles.

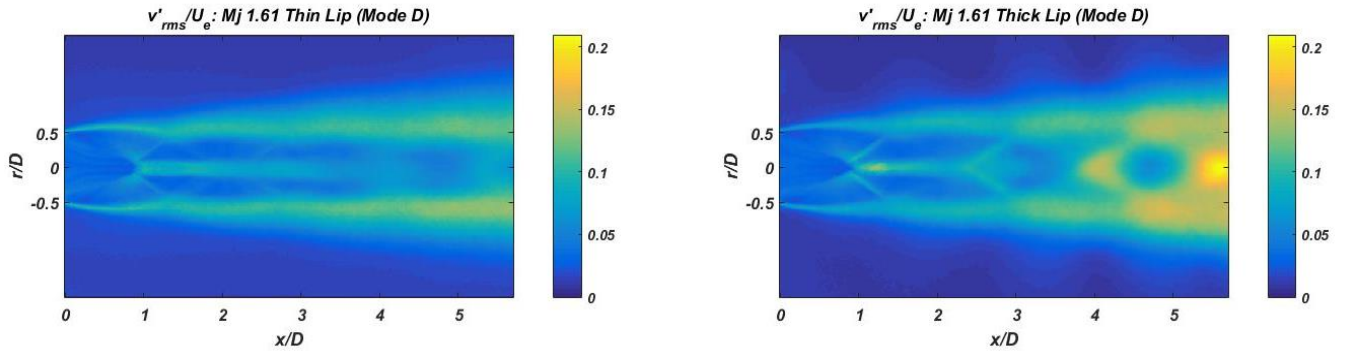

Figure 3. 21: transversal *rms* velocity fluctuation (v'_{rms}) normalized by *Ue* for *Mj=1.61*. Thin (left) and thick (right) lip nozzles.

Since we reported that the fluctuation levels are higher for the jets generated by the thick lip than by the thin one, we carry out an evaluation focusing on the lip thickness effect on the turbulence components in the mixing layer.

3.2.4.1 Turbulence Intensity

The longitudinal ($\sigma_u = \sqrt{\overline{u'^2}}$) as well as the transversal ($\sigma_v = \sqrt{\overline{v'^2}}$) turbulence intensities are normalized by the local difference of mean velocities $\Delta U = U_1 - U_2$, where U_1 and U_2 are the fast and slow flow velocities in each side of the mixing layer, respectively. Due

to the fact that underexpanded jets are not adapted flows, this study focuses on the values of $(\sigma_u/\Delta U)_{max}$ and $(\sigma_v/\Delta U)_{max}$ of each axial coordinate considered, corresponding to the strongest fluctuations in the mixing layer centre (André *et al.* 2014). The normalized longitudinal turbulence levels are plotted in figs. 3.22-3.24 for different *Mj* conditions.

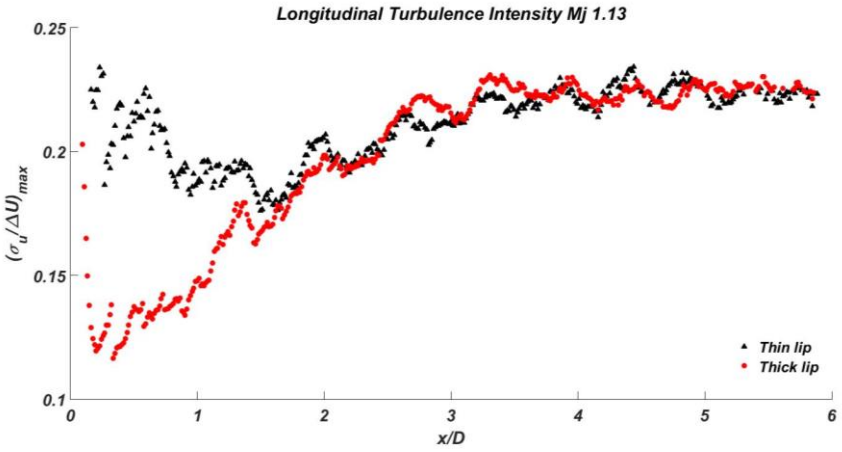

Figure 3. 22: maximum longitudinal turbulence intensity for *Mj=1.13*.

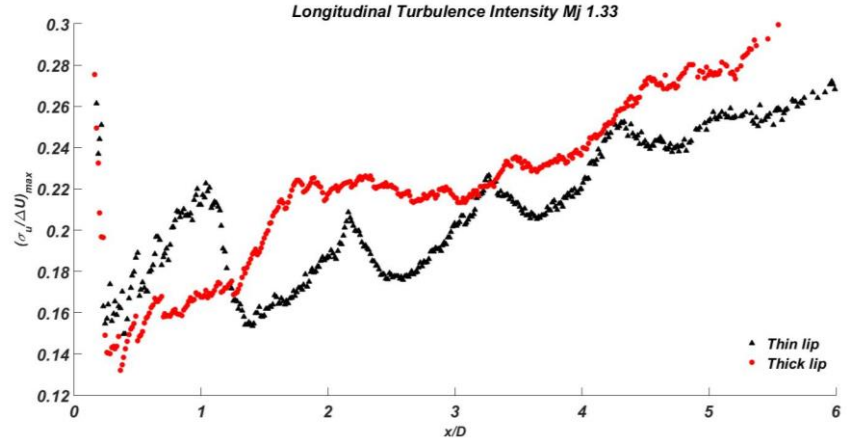

Figure 3. 23: maximum longitudinal turbulence intensity for *Mj=1.33*.

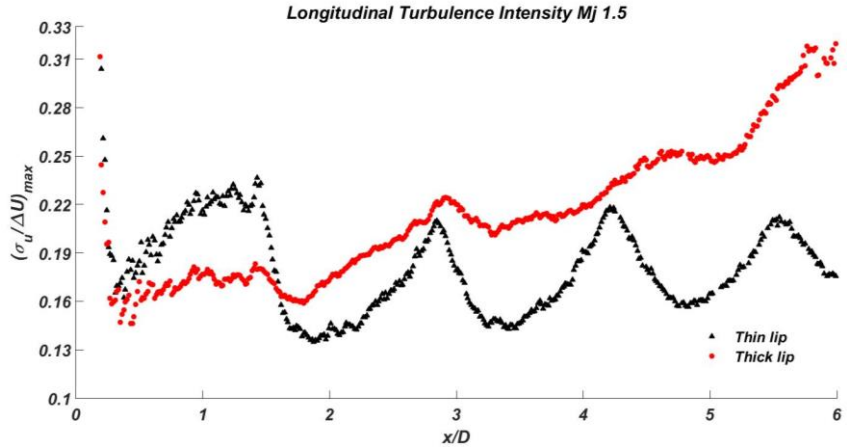

Figure 3. 24: maximum longitudinal turbulence intensity for *Mj=1.5*.

For M_j= *1.13*, the fig. 3.22 shows that the turbulence intensity reaches a plateau value of about 22% for both nozzles and smooth shock modulation is remarkable. This result is coherent with works of Tan *et al*. (2017) and André *et al.* (2014) where these authors found out that the turbulence is modulated by shocks. This modulation consists in turbulence suppression by shock.

One can notice in fig. 3.23 (M_j *=1.33)* that the jet generated by the thin lip presents a high modulation of the turbulence levels by the shock structure, contrary to the one generated by the thick lip that presents no remarkable modulations and a higher level of turbulence.

Interesting results can be seen in fig. 3.24, for M_j *=1.5*. We notice that up to second shock-cell, the turbulence seems to be modulated by shocks for both nozzles. However, beyond this location, no more modulation is observed for the thick lip. Moreover, similar to other *Mj* conditions, the thick lip generates turbulence intensities larger than the thin one. These high turbulence levels may be linked to large scale coherent structures which provide lower Screech frequencies for the thick lip, as noted in the acoustic results.

Regarding the transversal turbulence intensity, the results for the jet at *Mj =1.13, 1.33* and *1.5* are depicted in figs. 3.25-3.27, respectively. For M_j *=1.13* (fig. 3.25), the transversal turbulence reaches a plateau at 14% with the levels being very close for thin and thick lip, showing that both jets have similar behaviour as already observed from longitudinal turbulence intensity. The transversal turbulence intensity for the jets at M_j *=1.33* (fig. 3.26) and *1.5* (fig. 3.27) presents the same behaviour that the longitudinal intensities. Overall, we can observe that the thick lip nozzle generates flows more turbulent than the thin one.

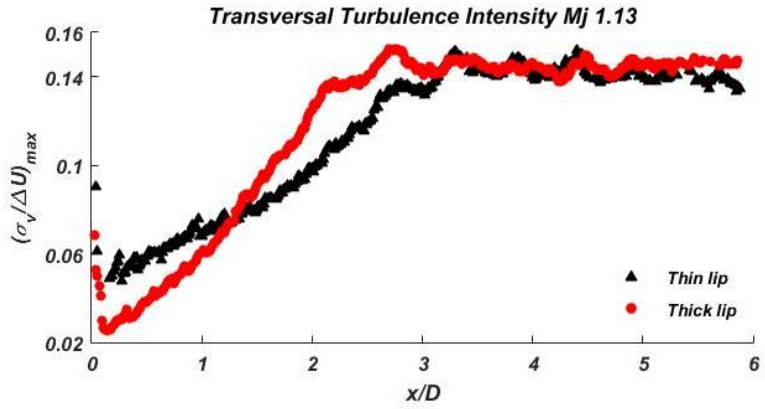

Figure 3. 25: maximum transversal turbulence intensity for *Mj = 1.13*

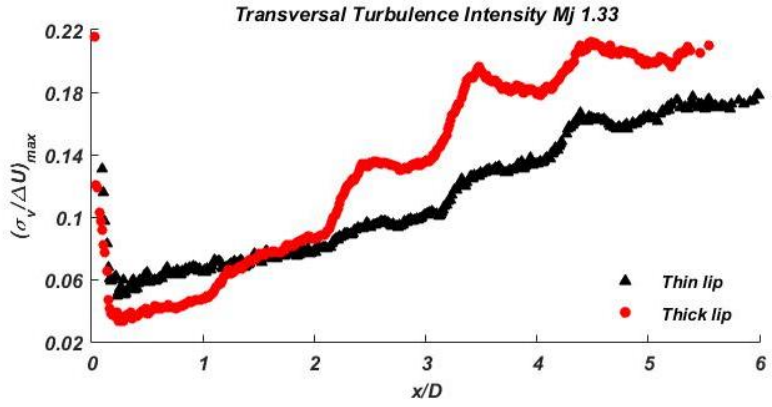

Figure 3. 26: maximum transversal turbulence intensity for *Mj=1.33*.

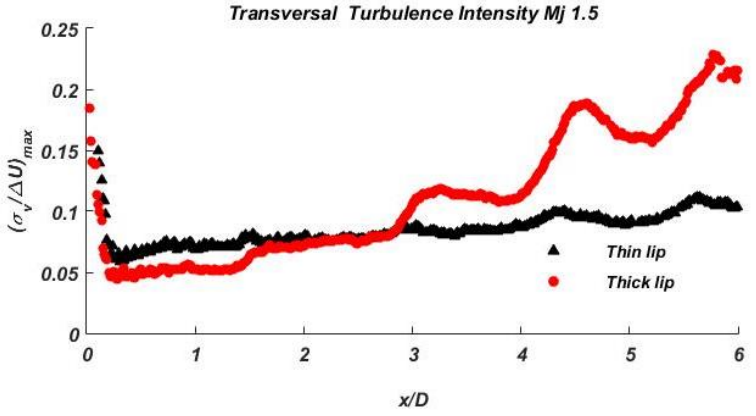

Figure 3. 27: maximum transversal turbulence intensity for *Mj=1.5*.

3.2.4.2 Reynolds Stress

In this section, the results obtained for the Reynolds stress $(\frac{\overline{u'v'}}{\Delta U^2})_{max}$ are plotted versus the axial coordinate (*x/D*). Similarly to the previous section, we evaluate the maximum shear stress value inside of the mixing layer at each axial coordinate.

The axial evolution of the maximum Reynolds stress $(\frac{\overline{u'v'}}{\Delta U^2})_{max}$ is presented in figs. 3.28-3.30, for the jet at *Mj=1.13*, *1.33* and *1.5*, respectively. Similarly to what has been observed in the turbulence intensity section, it is possible to notice that the thick lip nozzle yields larger Reynolds stress than the thin one. Again, we can infer that this behaviour is linked to the size of the coherent structures inside of the mixing layer.

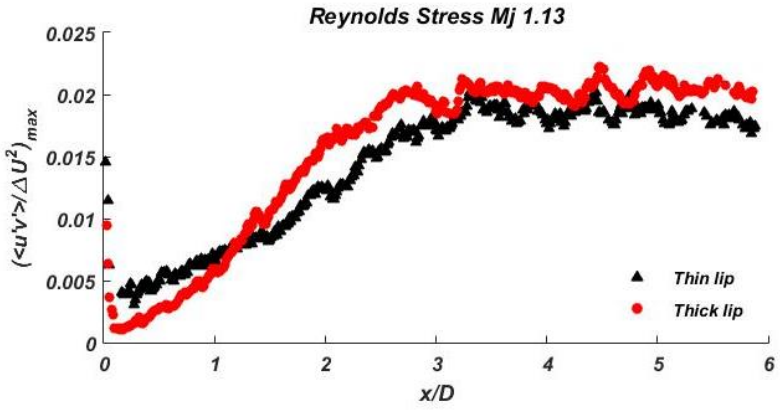

Figure 3. 28: maximum Reynolds stress in the mixing layer for *Mj =1.13*

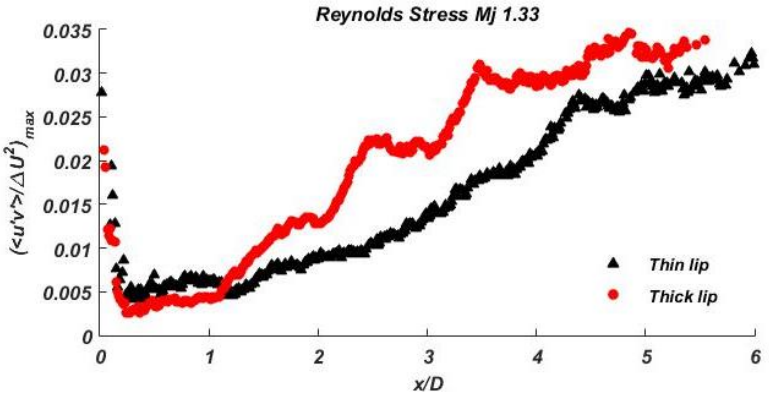

Figure 3. 29: maximum Reynolds stress in the mixing layer for *Mj=1.33*.

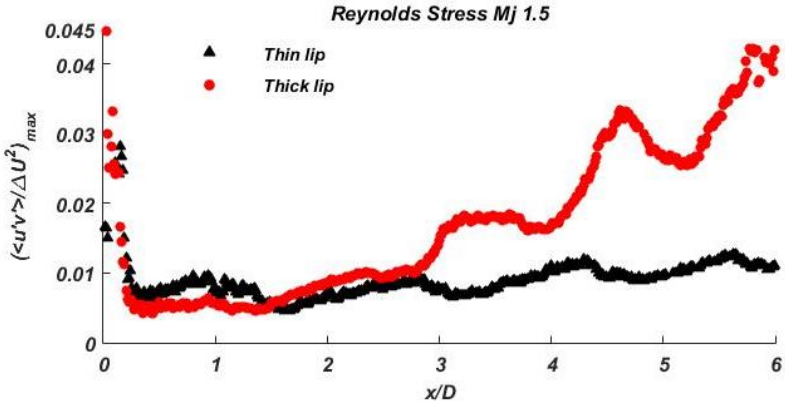

Figure 3. 30: maximum Reynolds stress in the mixing layer for *Mj=1.5*.

3.2.4.3 Compressibility Effects

In this section, we focus on the compressibility effects on the turbulence inside of the mixing layer. Firstly, the variation of the longitudinal turbulence intensity as a function of the Mach number is depicted in figs. 3.31 and 3.32, for the thick and thin lip nozzles, respectively.

We present these levels as a function of the average shock-cell length calculated by the Prandtl-Pack theory.

Analysing the results obtained with the thick lip nozzle (fig. 3.31), one can observe that the longitudinal turbulence levels increase from $M_j=1.13$ to $M_j=1.33$. In other words, the shifting between axisymmetric to flapping modes causes in general an increase in turbulence levels. Moreover, for higher *Mj* we can remark a slight decrease in the turbulence levels as expected by compressible effects (Samimy & Elliott, 1990, Pantano & Sarkar, 2002 and Fu & Li, 2006).

It is more problematic to analyse the compressibility effects (fig. 3.32) in the case of the thin lip due to shock-cell effects on the turbulence modulation. Indeed, contrary to the thick lip case, the jets generated by the thin lip nozzle present a strong modulation by the shocks. This behaviour may be explained by the thin mixing layer yielded by this nozzle which improves the turbulence modulation by the shocks. Moreover, the increase in the turbulence levels when the jets shifts from *Mj=1.13* to *1.33* is remarked, however less pronounceed that in the thick lip case.

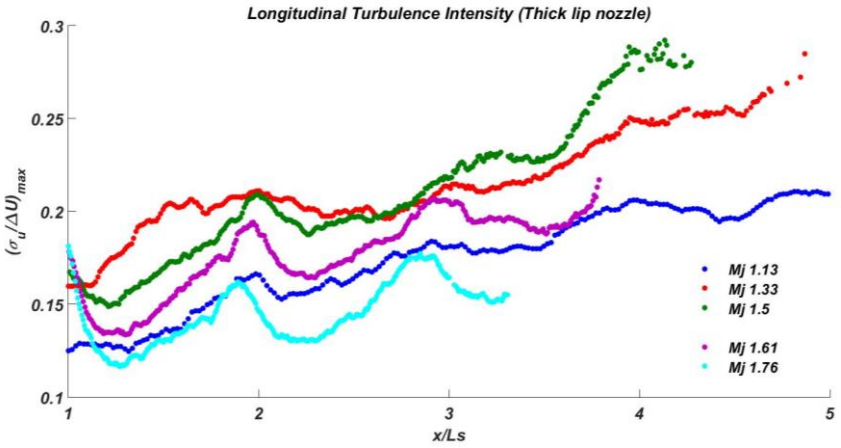

Figure 3. 31: maximum longitudinal turbulence vs shock-cell length for all *Mj* analysed conditions. Thick lip nozzle.

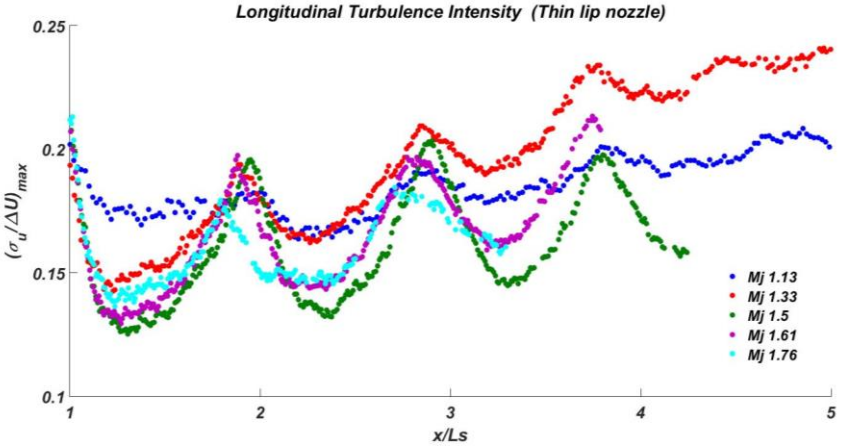

Figure 3. 32: maximum longitudinal turbulence vs shock cell length for all *Mj* analysed conditions. Thin lip nozzle.

In figs. 3.33 and 3.34 we present the transversal turbulence evolution as a function of the Mach number for both nozzles. It is possible to observe that again the turbulence levels increase when the jets shift from M_j *=1.13* to *1.33*, regardless the nozzle. The compressibility effects on the transversal turbulence, represented by the decrease in the turbulence levels as M_j increases, is more noticeable than for longitudinal turbulence intensity. This effect is much more pronounced in the case of the thick lip (fig.3.33) that may explain the abrupt reduction of the spreading rate with increasing Mach number for the jets generated by this nozzle (fig.3.15).

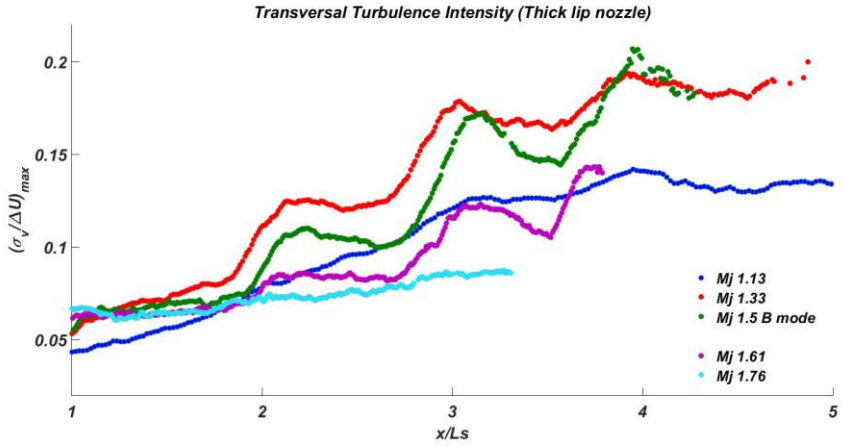

Figure 3. 33: maximum transversal turbulence vs shock cell length for all *Mj* analysed conditions. Thick lip nozzle.

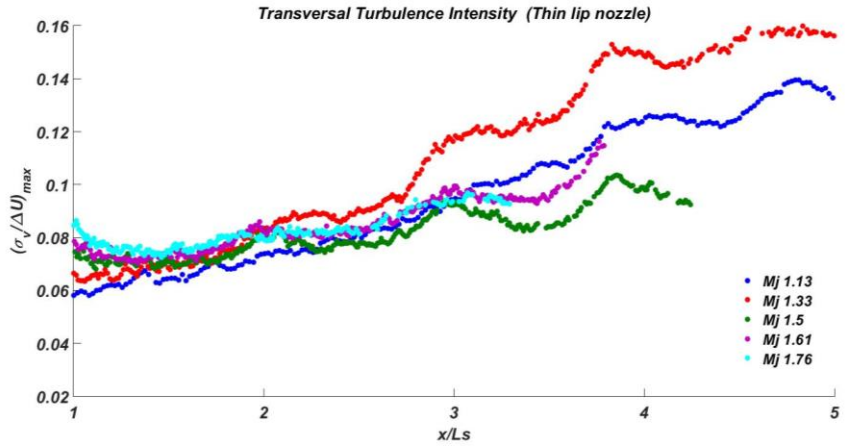

Figure 3. 34: maximum transversal turbulence vs shock cell length for all *Mj* analysed conditions. Thin lip nozzle.

The maximum Reynolds stress values are plotted as a function of x/L_s for all *Mj*, in figs. 3.35 and 3.36, for the thick and thin lip nozzles, respectively. We can see that for *Mj >1.33* the Reynolds stress level decreases with the Mach number, indicating a loss of production of turbulence in agreement with the lower turbulence intensity observed. Moreover, these effects are more pronounced in the flows generated by the thick lip nozzle (fig. 3.35) than the thin one (fig. 3.36), explaining the abrupt fall in the mixing layer spreading rate for the jets generated by the former (see fig. 3.15).

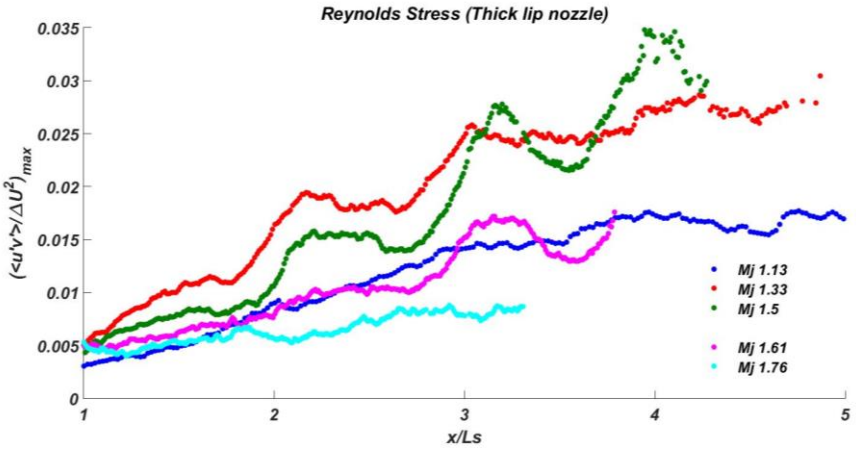

Figure 3. 35: maximum Reynolds stress vs shock cell length for all *Mj* analysed conditions. Thick lip nozzle.

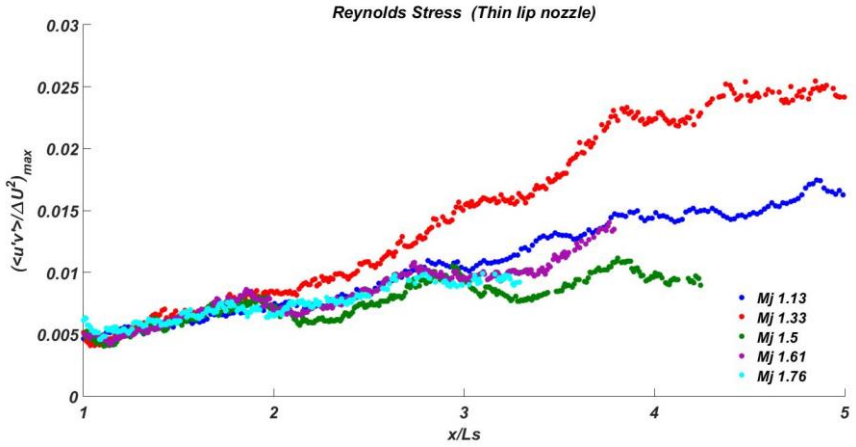

Figure 3. 36: maximum Reynolds stress vs shock cell length for all Mj analysed conditions. Thin lip nozzle.

3.2.5 Conclusion

The results in this section show that there is no important difference between the average shock-cell spacing generated by the thick and the thin lips, although the former presents slightly larger shock-cells. The wavelength of the standing waves are higher for the thin lip than for the thick one. It may mean that the thin lip generates jets with smaller coherent structures moving faster inside of the mixing layer. The thick lip nozzle provides mixing layers thicker than the thin one, in other words thick lip increases the jet spreading.

The compressibility effects on the mean fields are noticeable by the decrease of mixing layer spreading rate as M_j increased for both nozzles, except between *Mj =1.13* and *1.33* in the thick lip case where an increase in the jet spreading is observed. This might be due to a more pronounced Screech mode effect than the compressibility one.

The results also show that the turbulence levels are larger for the jets generated by the thick lip nozzle, suggesting that the associated coherent turbulent structures are larger too. This result is coherent with the standing waves measured where it was assumed that the small standing wavelength L_{sw} is due to slower and larger coherent structures propagating inside of the

mixing layer. Moreover, evaluation of compressibility effects on the turbulence reveals that the thick nozzle provides jets where these effects are much more pronounced.

3.3 Flow Structures

In this section we focus on the nozzle lip thickness effects on the coherent structures of the flow.

3.3.1 Hydrodynamic wavelength (L_h)

The passage of vortices generates density gradient fluctuations that are visible in the Schlieren images. In order to study the link between these vortices propagating inside of the mixing layer and the acoustic near-field, we calculate the correlation coefficient:

$$R(I')(x_0, x_n) = \frac{\overline{I'(x_0)I'(x_n)}}{\sigma_{I'(x_0)}\sigma_{I'(x_n)}} \qquad \text{eq. 3.2}$$

where R is the correlation coefficient, I' represents the grey level intensity fluctuations, x_0 and x_n are the reference and compared points, respectively. Moreover, the overbar is the average operator and σ is the *rms* value of the grey levels fluctuations.

Edgington-Mitchell *et al.* (2015) pointed out that the correlated images provide information about the hydrodynamic wavelength of the mixing layer structures. Furthermore, the authors observed that the space between the strong correlations peaks is the same placing the reference point either within the standing wave (lobes) or in the shear layer. Indeed, we observe in the fig. 3.37 that the distance between the correlation peaks in the near-fields are almost the same, considering the reference point in the shock line or in the standing waves lobes.

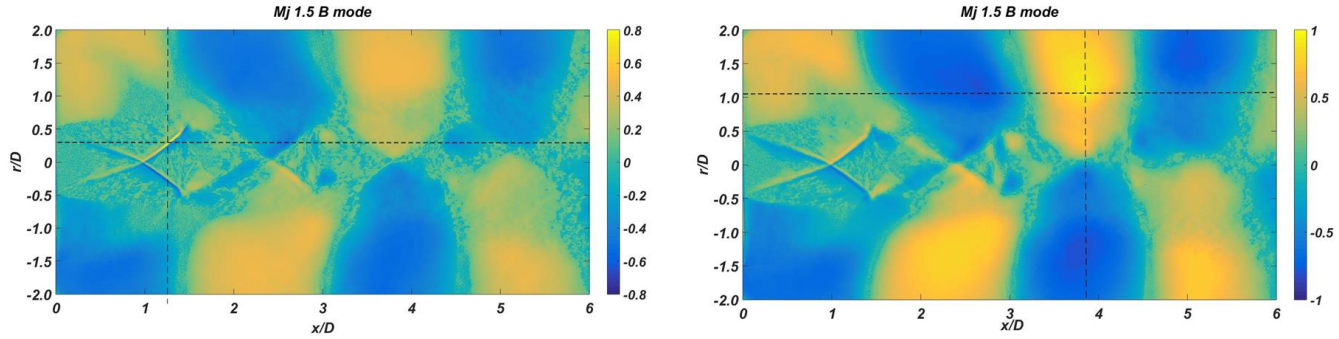

Figure 3. 37: correlation coefficient (R) for the jet at *Mj=1.5* generated by thick lip nozzle. The reference points are represented by intersecting dashed lines: shock line (left) and standing wave (right).

Hence, we can notice, in the same figure, that the shock motion is well correlated with the structures propagating inside of the mixing layer. Moreover, it is possible to remark that the correlation levels are higher when employing the standing waves as the reference point. This is due to the high fluctuations levels found in the lobes, providing an increase in the correlation coefficients.

The figs. 3.38 and 3.39 presents the results of the correlation for the jets at *Mj=1.33* and *1.5*, respectively. These images show the nozzle effect on the correlation maps when the

reference point is placed in the standing waves. It is interesting to notice that the topology of the images show the dominant Screech jet mode. Indeed, the correlations are opposite in phase, representing a sinuous motion linked to the flapping mode *B*.

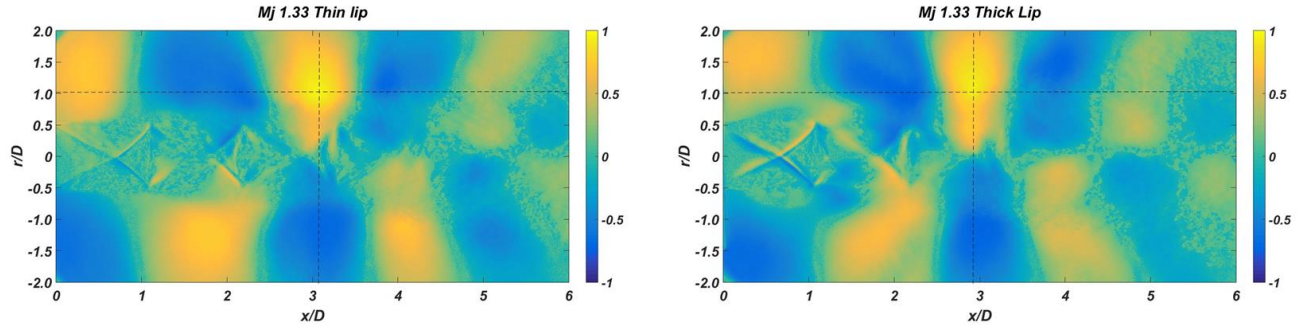

Figure 3. 38: correlation coefficient (*R*) for the jet at *Mj=1.33*. The reference point is located inside the standing waves and is represented by the intersecting dashed lines. Thin (left) and thick (right) lip nozzle.

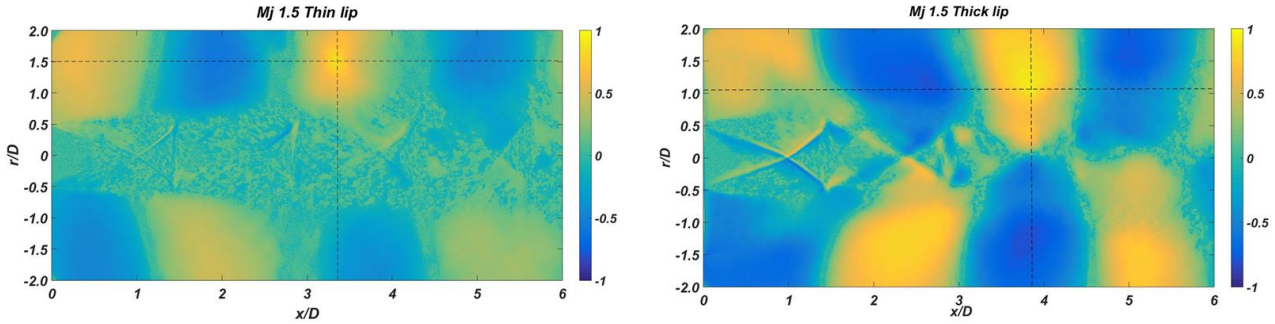

Figure 3. 39: correlation coefficient (*R*) for the jet at *Mj=1.5*. The reference point is located inside the standing waves and is represented by the intersecting dashed lines. Thin (left) and thick (right) lip nozzle.

The hydrodynamic wavelength (L_h) may be obtained measuring the spacing between the two correlation peaks in the fig. 3.38 and 3.39. The measured value of L_h/D was 2.7 and 2.3 for the jets at *Mj=1.33* generated by the thin and the thick lip nozzle, respectively. Similar trend was observed for the jets at *Mj=1.5* (fig. 3.39), where L_h/D*=3.1* and *2.84* are obtained for the thin and the thick lip nozzles, respectively.

Assuming that the structures are convected with the velocity $U_c = L_h f_s$, where *fs* is the Screech frequency and knowing that the frequency increases for the jets generated by thin nozzle (as seen in the section 3.1), we can infer that the thin lip generates structures with higher convection velocities in the mixing layer. This result agree with the standing wave observation. Unfortunately, the conditions *Mj=1.61* and *1.76* did not provide suitable correlation maps that enabled the evaluation of L_h. This forbid us to generalize these observations to other Mach numbers.

3.3.2 Structures Dynamics

The previous sections showed that the nozzle lip thickness induces changes in the Screech frequency. Moreover, it has been verified that the thick lip nozzle generates flows with

higher turbulence levels than the thin one, which can be associated to the fact that larger coherent structures are convected in the mixing layer. As larger structures are known to have smaller convective velocities (Kerhervé et al., 2006 and Panda, 2006), these observations are in agreement with the fact that the thick lip nozzle generates Screech with lower frequencies.

In order to evaluate the nozzle lip effect on structures dynamics, we propose here to carry out an investigation of the jets via POD (Proper Orthogonal Decomposition) on the PIV data. It was chosen to evaluate the data acquired at *Mj =1.13* and *1.5*, covering axisymmetric and flapping modes, for the reason that these conditions represent the two Screech modes studied in this chapter. Moreover, it was necessary to optimize the velocity field on which the POD is applied in order to obtain spatial modes (ϕ) that best represent the convective movement of the structures. However, for the jet at *Mj =1.13* generated by the thin lip, it was not possible to conduce the study of the streamwise components due to the fact that the spatial functions (ϕ) did not indicate a convective motion. Thus, for this *Mj* condition only the transversal fluctuations are considered.

The spatial functions of the two first modes (leading pair) are presented in figs. 3.40-3.43. The first and second POD modes represent the jet dominant instability and we can observe that the most important part of the energy is located in the mixing layer, characterizing the large coherent structures of the flow and associated to Kelvin-Helmholtz instabilities. It is possibe to notice that the modes seem to be in phase quadrature ($\pi/2$), a necessary condition for the POD modes to represent a convective movement. Moreover, we observe that the thick lip nozzle provides more energetic spatial functions than the thin one, for *Mj=1.5*. This observation may be linked to the fact that the thick lip nozzle generates larger coherent structures with higher turbulence intensity, leading to higher levels of the fluctuating energy capted by POD.

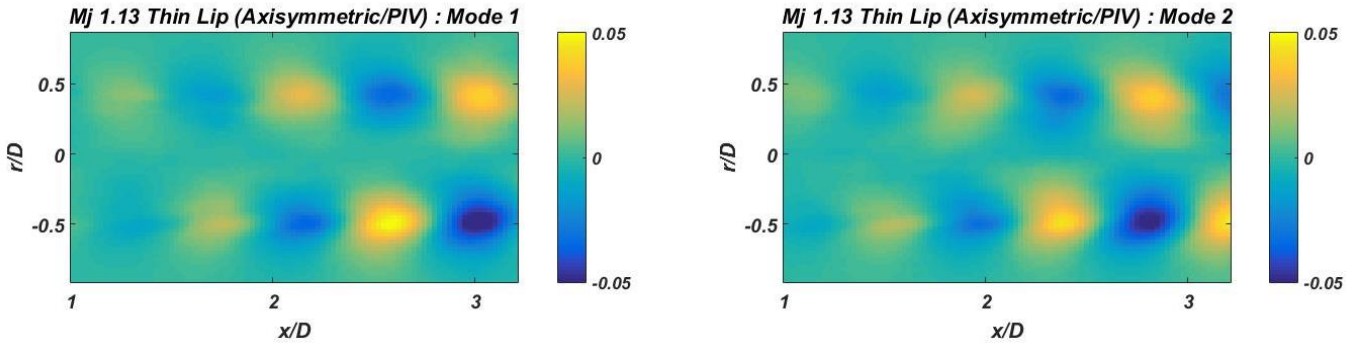

Figure 3. 40: transverse spatial (ϕ_1 and ϕ_2) POD modes for *Mj =1.13*, thin lip nozzle.

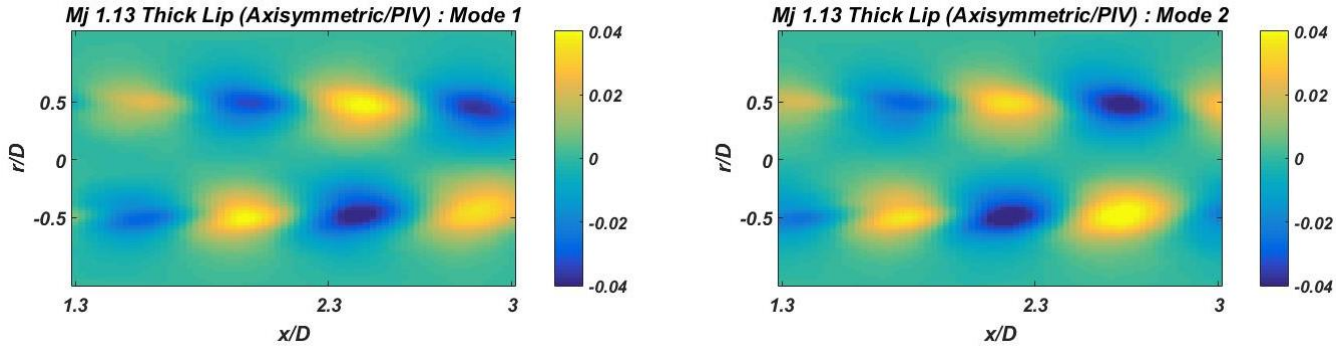

Figure 3. 41: transverse spatial (ϕ_1 and ϕ_2) POD modes for *Mj=1.13*, thick lip nozzle.

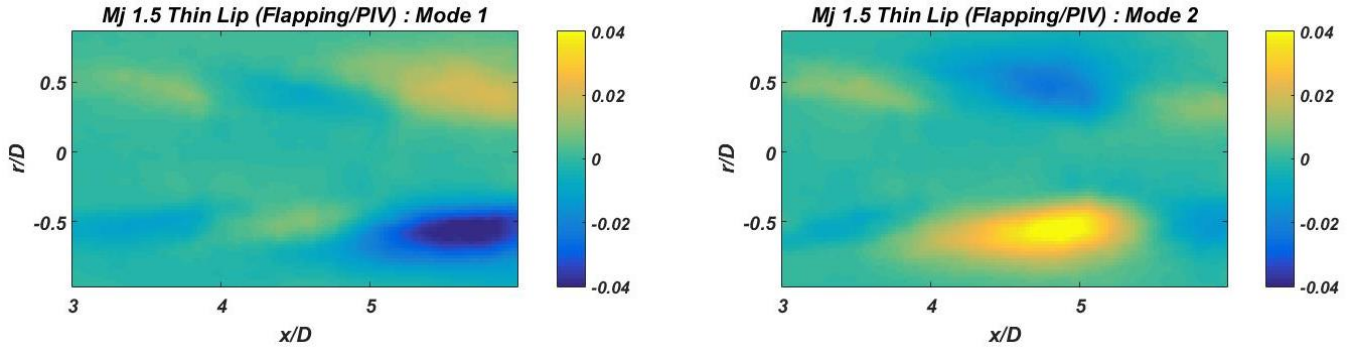

Figure 3. 42: streamwise spatial (ϕ_1 and ϕ_2) POD modes for *Mj =1.5*, thin lip nozzle.

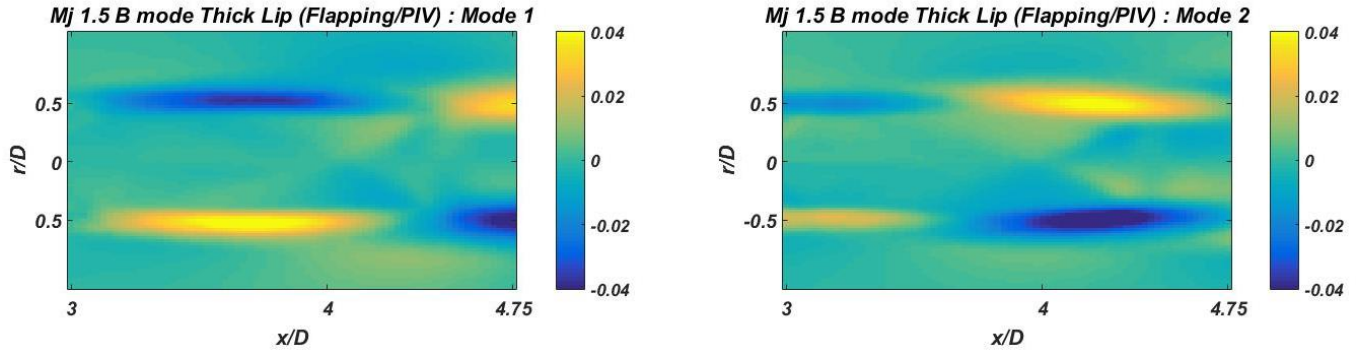

Figure 3. 43: streamwise spatial (ϕ_1 and ϕ_2) POD modes for *Mj =1.5*, thick lip nozzle.

In order to evaluate the temporal relation between the two first modes and their relative energy, the figs. 3.44-3.47 are presented below. In figs. 3.44 and 3.45 it is possible to observe that flow structures under axisymmetric Screech mode have a leading POD modes pair possessing almost the same relative energy. Moreover, one can observe in the same figures a clear temporal organization of the temporal POD modes highlighted by the fact that they scatter to form a Lissajous curve. Since no difference in the organization of the two first temporal modes is visible regardless the kind of nozzle, we can argue that the nozzle lip thickness does not seem to influence the dynamics of the coherent structures for the jets under axisymmetric Screech mode.

The results for the flapping mode (*Mj =1.5*) are presented in the figs. 3.46 and 3.47. It is possible to notice a leading pair modes with a similar and representative energy for the jet

generated by the thick lip, contrary to the thin one for which three modes with similar relative energy dominate the flow fluctuations. However, even though no shown here, the third POD mode does not present any organization of coherent structures and from the associated spatial POD functions (fig. 3.42) we have observed that the flow structures issued from the thin lip nozzle are organized similarly to those from the thick lip one. As such, we can also argue that the structures dynamics are not influenced by the nozzle lip thickness for the jets under flapping Screech mode.

Concerning the temporal coefficients, the flapping modes (figs. 3.46 and 3.47) does not present a clear organization of the coherent structures. This fact may be due to the disorganized precession movement which causes a mismatch between the temporal coefficients, providing penalties in the correlation. Indeed, the flapping *B* mode is characterized by sinuous oscillation of the jet. Then, when these oscillations are in the plane *r-x* (parallel camera sensor) the POD is able to capture the temporal coefficients and these ones present a clear organization. However, in the case where the jet oscillation occurs in the plane perpendicular to the camera, the POD is no more able to capture the temporal coefficients, attributing lower values, even zero. This explain the large amount of points in the center of the temporal coefficients maps (a_1,a_2) for flapping modes.

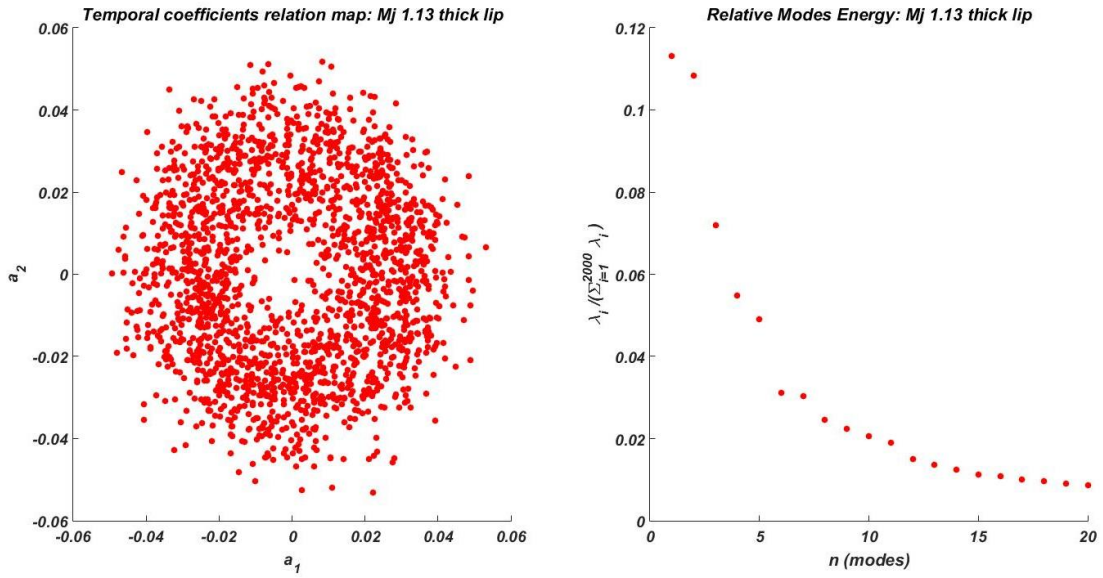

Figure 3. 44: phase portrait of the temporal coefficients *a1* and *a2* (left). Relative POD modes energy (right) for *Mj =1.13*, thick lip nozzle.

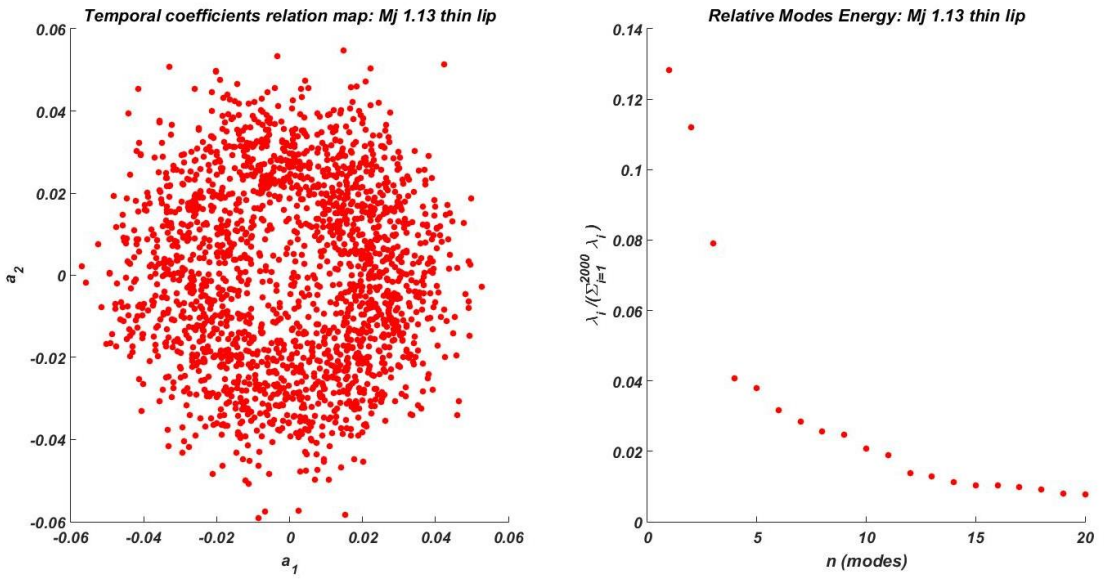

Figure 3. 45: phase portrait of the temporal coefficients *a1* and *a2* (left). Relative POD modes energy (right) for *Mj=1.13*, thin lip nozzle.

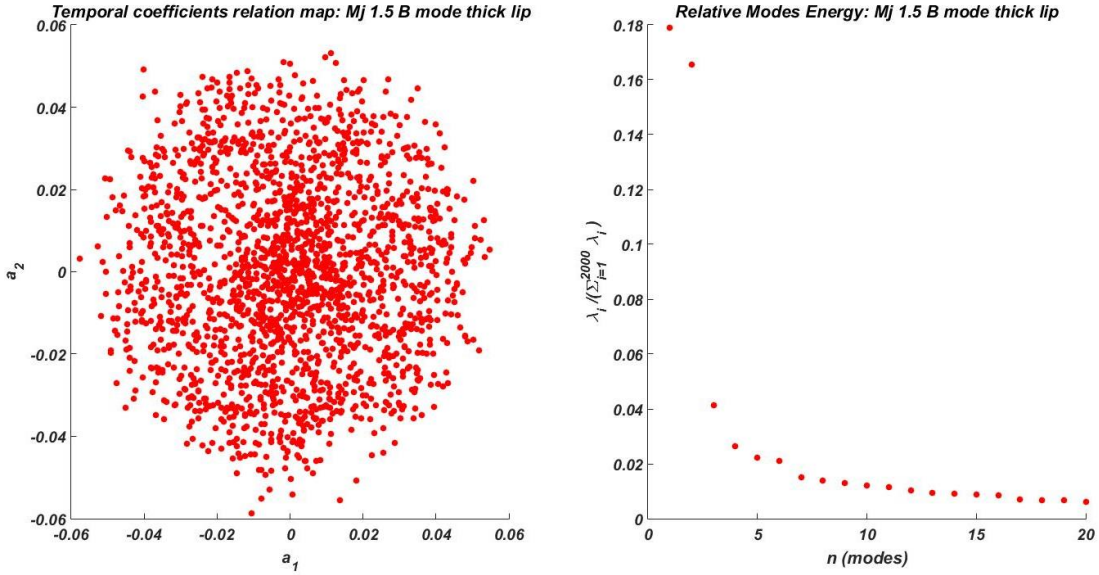

Figure 3. 46: phase portrait of the temporal coefficients *a1* and *a2* (left). Relative POD modes energy (right) for *Mj=1.5*, thick lip nozzle.

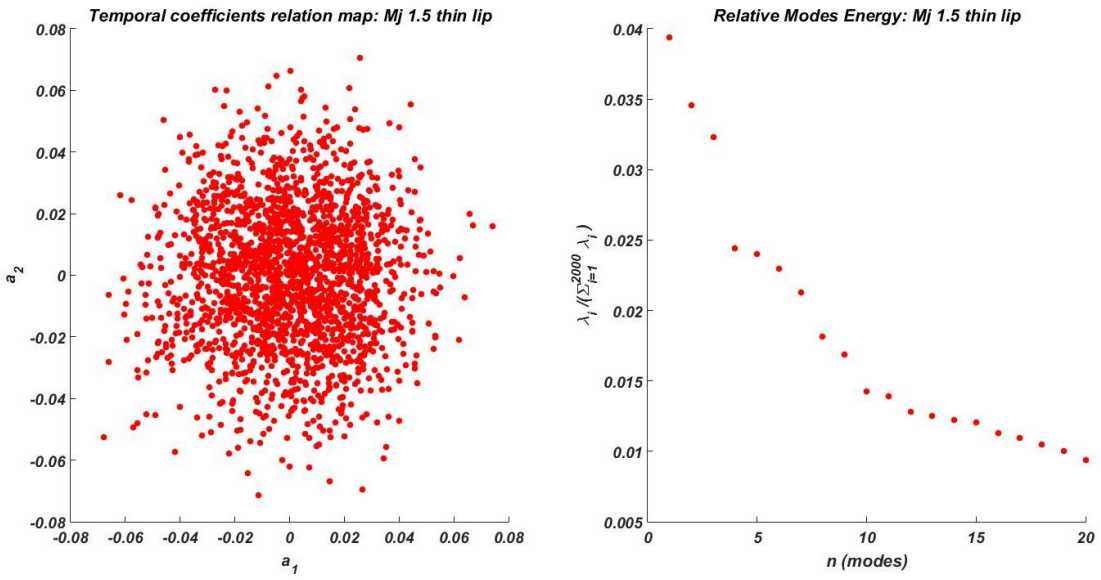

Figure 3. 47: phase portrait of the temporal coefficients *a1* and *a2* (left). Relative POD modes energy (right) for *Mj= 1.5*, thin lip nozzle.

3.3.3 Conclusion

The hydrodynamic wavelength results suggest that the vortices are convected with higher velocities in the jets generated by the thin lip nozzle than by the thick one. This observation agrees with the standing waves measured and reinforces the idea that the thick lip nozzle produces larger and slower coherent structures than the thin lip one. Moreover, the correlation maps show that the shock and flow structures are correlated.

The POD analysis shows that the thick lip nozzle provides more energetic spatial functions than the thin one. This fact may be linked to larger coherent structures with higher turbulence intensity propagating in the mixing layer, leading to higher levels of the fluctuating energy capted by POD. Finally, the results suggested that globally the dynamics of the coherent structures of the flow are the same, regardless of the nozzle. It means that the both nozzles generate jets with a leading pair modes with noticeable and similar relative energy, representing a convective motion of the structures attributed to Kelvin-Helmholtz instabilities. In other words, the nozzle thickness lip does not appear to have any effect on the structures dynamics.

Summarizing the results of this chapter, we have observed that, as expected, the nozzle lip thickness causes effects on the Screech. Moreover, the mean velocity fields and the turbulence are affected too, meaning that the Screech is linked to the characteristics of the coherent structures such as size and convection velocity. Nevertheless, the dynamic of these structures seem to be not affected by the nozzle thickness. Therefore, the next chapter we carry on the study, focusing on the Screech dominant modes effects, in order to understand the staging phenomenon (frequencies shift).

4 SCREECH MODES EFFECTS

We have seen in the chapter 3 that the jet turbulence is affected by the nozzle lip thickness and subsequently that the lip thickness affects the Screech frequency. This suggests, as expected, that the Screech is linked to flow coherent structures. Moreover, we have shown, however, that the underlying dynamics remain independent of the nozzle lip thickness. Now, we focus on the effects of a given Screech mode on the flow characteristics. For this we use the fact that the thick lip nozzle is able to generate two types of modes at same Mach number *Mj=1.5*. Thus, this part of the work presents how the topology and the flow structures may be influenced by the two different dominant Screech modes *B* and *C*.

4.1 Flow Topology

This part of the work presents the results of the Screech modes effect on the general flow topology of the jets.

4.1.1 Average Flow Topology and Shock-Cell Spacing

The average density gradient is provided in fig. 4.1, for both Screech modes. At frst glance, no difference on the shock-cells structure can easily be seen between the two images. Indeed, measuring the average shock-cell spacing (L_s/D), we obtain the values of *1.42* and *1.43* for the flow under *B* and *C* Screech dominant modes, respectively. Hence, this small difference can not explain the Screech frequency changes due to this mode shifting, where the Strouhal number varies from *St=0.27* (flapping *B* mode) to *0.32* (helical *C* one). The result agrees with the observations of Clem *et al.* (2016), who did not observe brutal changes in the shock-cell spacing during Screech jumps.

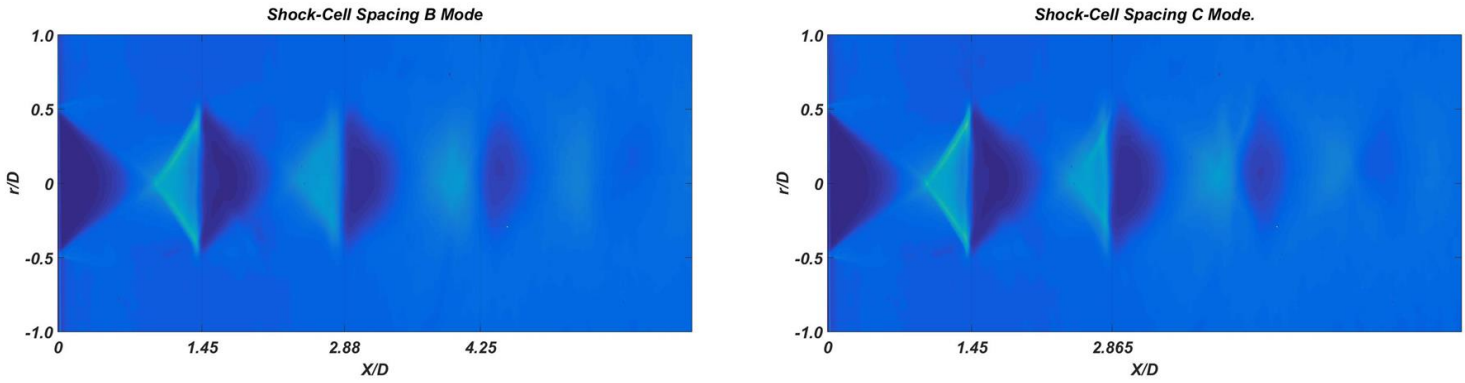

Figure 4. 1: mean density gradient for *Mj = 1.5*. Flapping (left) and helical (right) Screech modes. Shock-cell spacing represented in axial coordinate.

4.1.2 Standing Wavelength

The *rms* values of grey level fluctuations for each Screech mode are shown in fig. 4.2. At first glance, it is not possible to remark large differences between the two flows, maybe except for the second shock-cell under helical mode that presents slightly higher fluctuation level. One can see, for both jets, high fluctuations levels in the near-field, represented by bright

and dark bands. As already mentioned, these lobes are due to standing waves formation (Panda, 1999, Edgington-Mitchell *et al.*, 2015 and Gojon *et al.*, 2018).

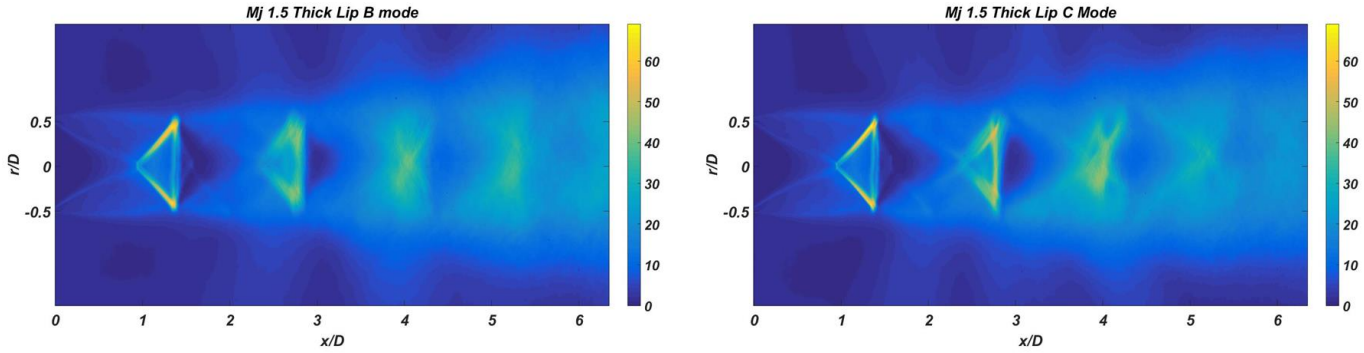

Figure 4. 2: *rms* intensity of grey level fluctuations. *B* flapping (left) and *C* helical modes (right).

As mentionned in section ***4.1.1,*** the shock-cell spacing is not representative of Screech jet modes. It means that there is no link between modal change and shock-cell spacing, but shock-cells are necessary for Screech jets. Regarding the standing waves, the measured wavelength are $L_{sw}/D=1.16$ and *0.93* for flapping and helical modes, respectively. Thus, contrary to the average shock-cell spacing where there is almost no difference, the standing wavelength ratio between the *C* and *B* mode is about *80%*. Considering that the ratio between the Strouhal numbers for *B* ($St=0.27$) and *C* modes ($St=0.32$) is *84%* , we can notice that the L_{sw} reflects the fact that a higher Screech frequency is observed for the *C* mode than for the *B* one. This result agrees with the work of Panda et al. (1997).

4.1.3 Mean Velocity Fields

The longitudinal and transversal mean velocity fields, normalized by *Ue* (jet velocity at the nozzle exit) are presented in figs. 4.3 and 4.4. At first glance, there is almost no difference in the flow topology and the mean velocity fields for the jets under flapping and helical modes. This behaviour is coherent with Schlieren observations. The profile of mean axial velocity ($r/D=0$) is depicted in fig. 4.5. We observe that the profiles are almost the same up to the second shock-cell ($x/D\cong 2.8$). However, from this point the profiles differ slightly and the *B* mode presents larger shock-cell spacing than the *C* one.

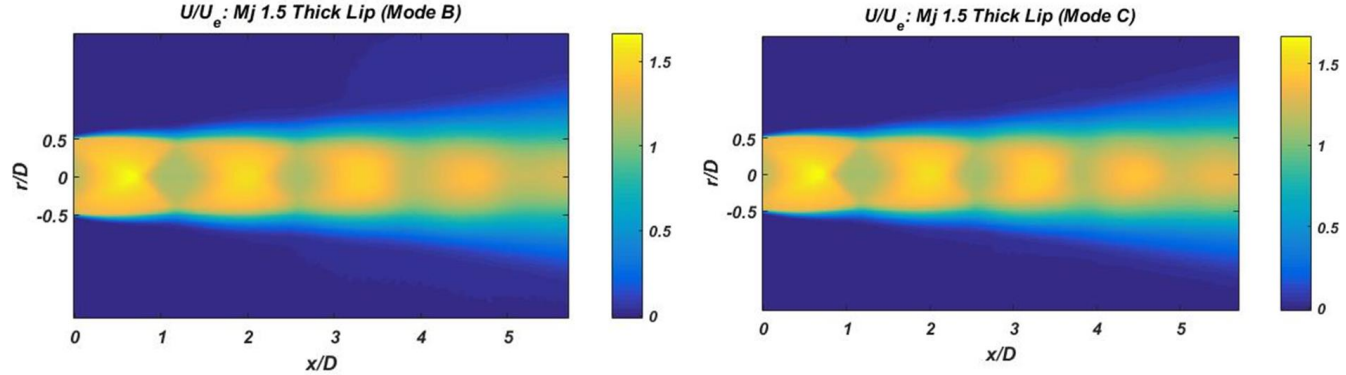

Figure 4. 3: longitudinal mean velocity (*U*) normalized by *Ue*. Flapping (left) and helical (right) Screech modes.

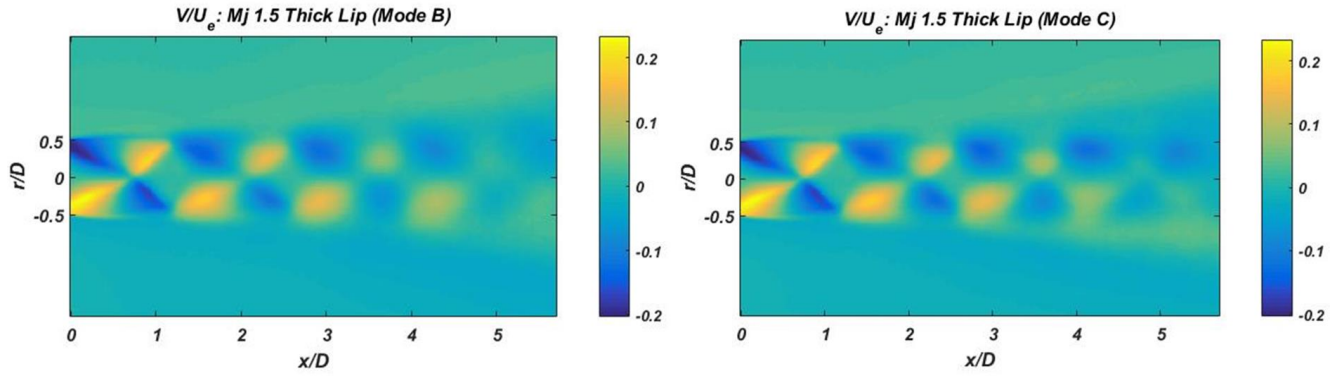

Figure 4. 4: transversal mean velocity (*V*) normalized by *Ue*. Flapping (left) and helical (right) Screech modes.

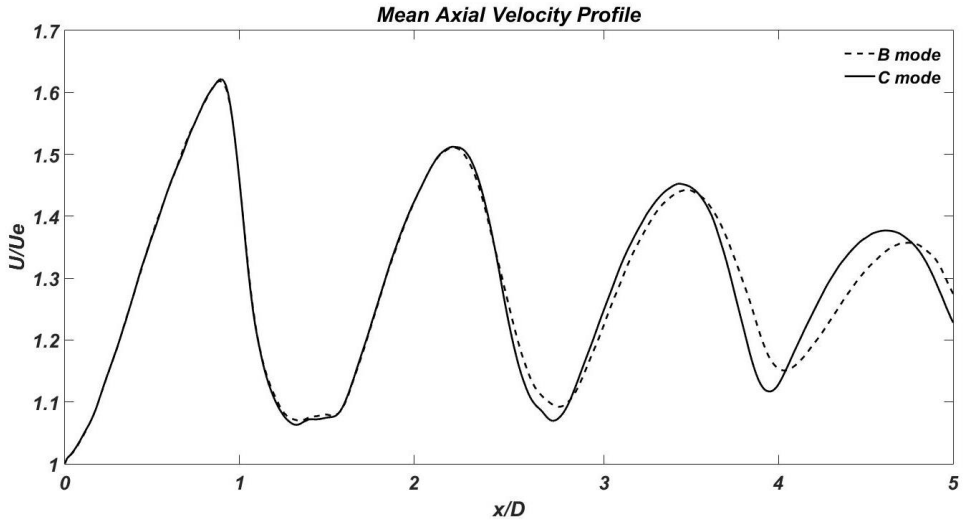

Figure 4. 5: mean axial velocity profile, normalized by *Ue*, for the jet at *Mj=1.5*.

The velocity profiles of the mixing layer, for 4 jet axial positions (*x/D=2, 3, 4 and 5*), are presented in fig. 4.6. The velocity and coordinates are normalized as:

$$U^* = (U - U_2)/(U_1 - U_2) \qquad \text{eq. 4.1}$$

$$y^* = (y - y_{ref})/\delta_\omega \qquad \text{eq. 4.2}$$

where y_{ref} is the coordinate at half velocity of the profile. It needs to be stressed that due to the presence of shocks, the velocity is not constant along the radial coordinate in the potential core of the jet. This explain why the velocities are not taken into account until the jet center line. Analysing the fig. 4.6 we can observe that at *x/D=2.0* the profiles shape are independent of the Screech mode. Although downstream we can notice small differences, coherent with the observations of the the average velocity centerline profile (fig. 4.5).

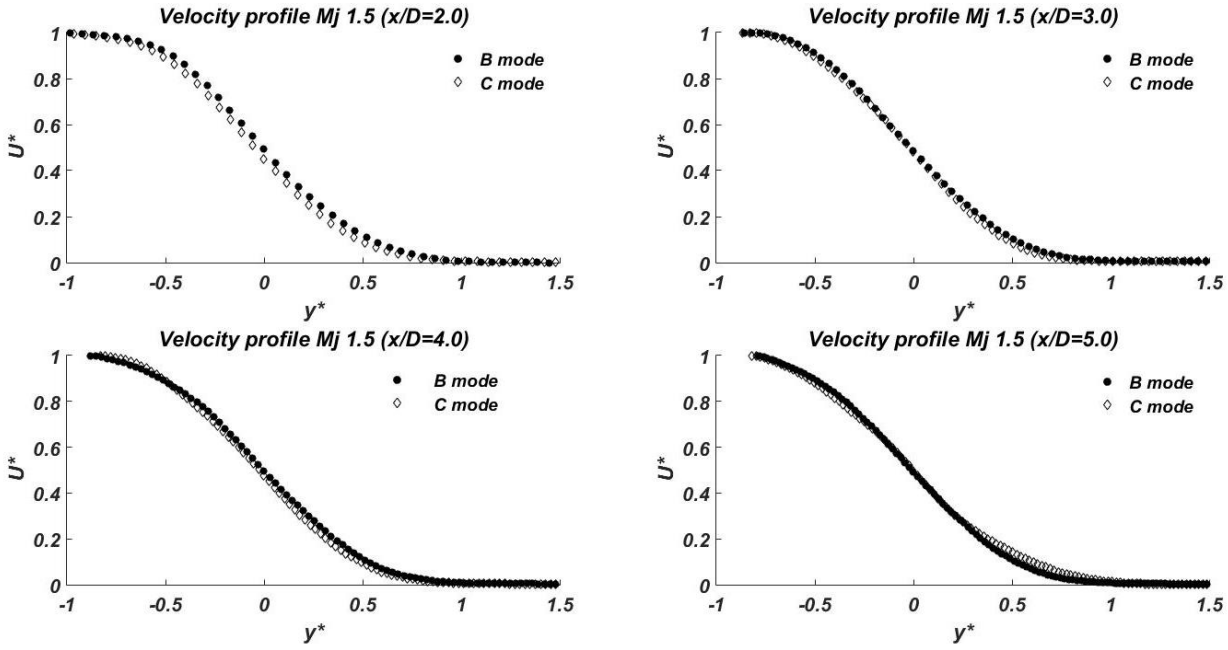

Figure 4. 6: mixing layer velocity profiles.

We present in fig. 4.7 the evolution of the mixing layer vorticity thickness for the jets under dominant *B* and *C* Screech modes. As expected, the mixing layer evolves in a similar way for the two conditions, in the field of view analysed. Hence, no substantial changes are remarked in the mean velocity fields that can explain the frequencies jumps observed between these to Screech modes.

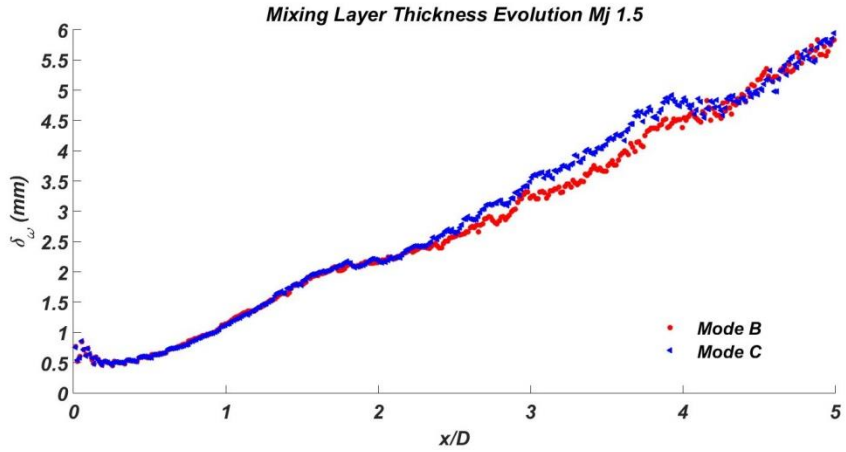

Figure 4. 7: mixing layer thickness evolution. Flapping (red) and helical Screech mode (blue).

4.1.4 Velocity Fluctuations Fields

The figures (4.8-4.9) present comparisons between normalized longitudinal and transversal fluctuations for flapping and helical modes. One can notice that the flows present different turbulent fields: higher turbulence levels are observed for the *B* mode than for the *C* one. This is visible for the both velocity components. As such, a study about turbulence in the mixing layer is carried out.

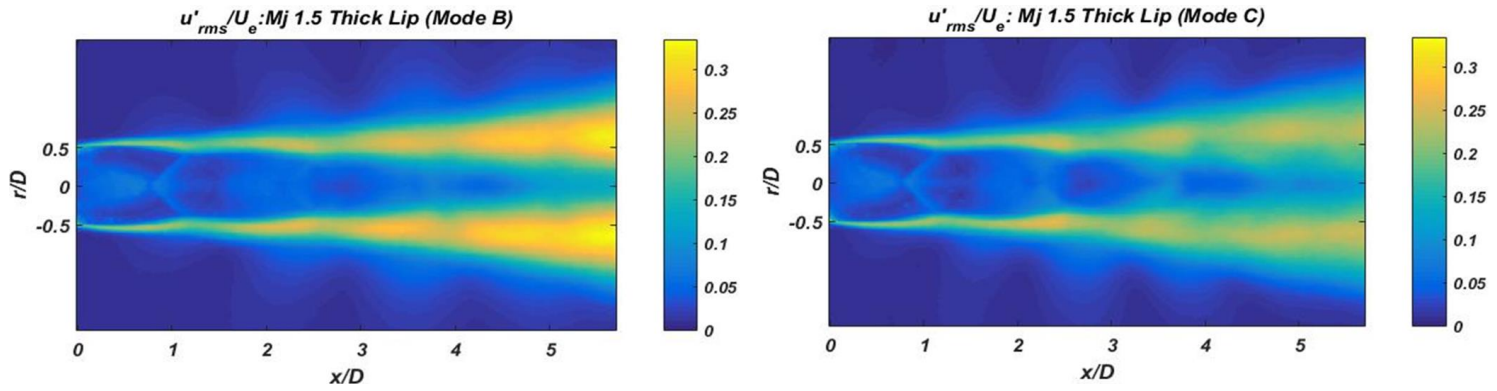

Figure 4. 8: longitudinal *rms* velocity fluctuation (u'_{rms}) normalized by *Ue*. Flapping (left) and helical (right) Screech mode.

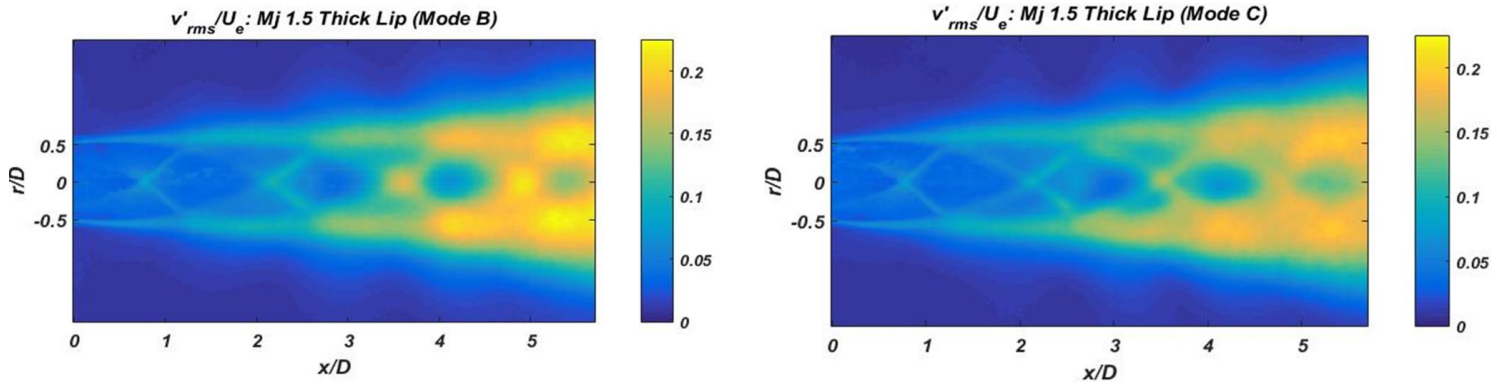

Figure 4. 9: transversal *rms* velocity fluctuation (v'_{rms}) normalized by *Ue*. Flapping (left) and helical (right) Screech mode.

4.1.4.1 Turbulence Intensity

We present in fig. 4.10 and 4.11 the longitudinal ($\sigma_u = \sqrt{\overline{u'^2}}$) as well as the transversal ($\sigma_v = \sqrt{\overline{v'^2}}$) turbulence levels normalized by the local difference of velocities $\Delta U = U_1 - U_2$, for both Screech modes. As mentioned, due to fact that the underexpanded jets are not adapted flows, this study focuses on the $(\sigma_u/\Delta U)_{max}$ and $(\sigma_v/\Delta U)_{max}$ for each considered axial coordinate which corresponds to strongest fluctuations measured in the mixing layer. It is possible to notice that the longitudinal turbulence intensity (fig. 4.10), from *x/D=1.5*, reaches levels varying between 17%-25% for the mode *B* and 18%-22% for the *C* one.

Another meaningful feature which is possible to notice in this figure is that, up to the second shock-cell (*x/D≅ 2.8*), the turbulence for both conditions seems to be modulated by shocks. However, this behaviour changes for the flapping mode downstream of this position. This behaviour is coherent with the fact that almost no differences are remarked up to the second shock-cell in the average velocity centerline profile. Similarly to the longitudinal intensity, the transversal turbulence (fig. 4.11) reaches values larger for the flapping *B* mode (*18%*) than for *C* (*15%*) one.

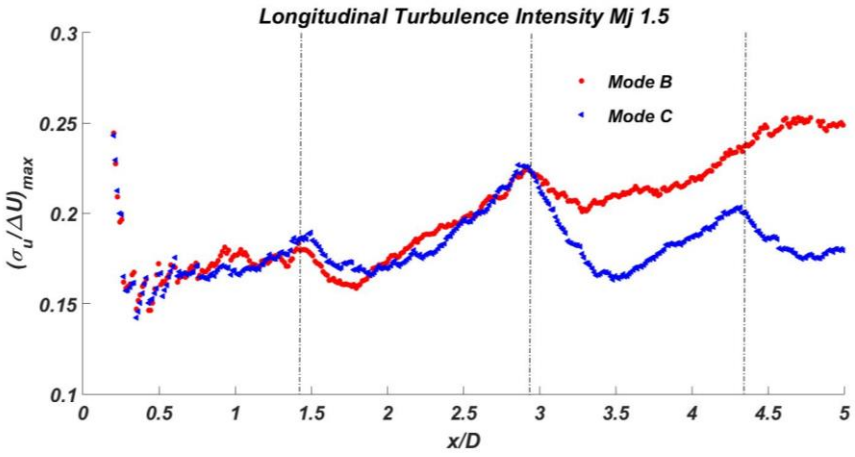

Figure 4. 10: maximum longitudinal turbulence intensity. Flapping (red) and helical Screech mode (blue). The shock positions are represented by dashed lines from Prandt-Pack's theory.

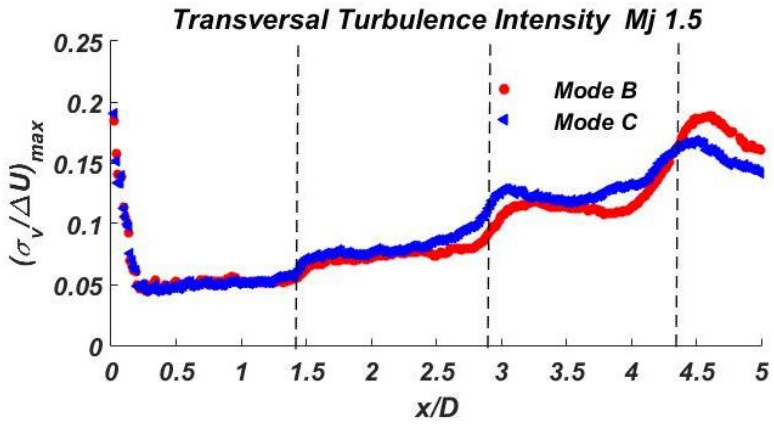

Figure 4. 11: maximum transversal turbulence intensity. Flapping (red) and helical Screech mode (blue). The shock positions are represented by dashed lines from Prandt-Pack's theory.

Overall, contrary to the mean velocity fields observations, where no appreciable Screech modes effects are noticed, the different dominant modes cause remarkable changes in the mixing layer turbulence. The explanation for this behaviour is underpinned by differences in the coherent structures (Kelvin-Helmholtz instabilities) convected inside of the mixing layer. In other words, the Screech modes excite differently the initial instabilities, causing differences in the amplification of these ones, with important consequences in the turbulence levels inside of the shear-layer.

4.1.4.2 Reynolds Stress and Anisotropy

The maximum value of the Reynolds stress $(\frac{\overline{u'v'}}{\Delta U^2})_{max}$ and anisotropy $(\sigma_u/\sigma_v)_{max}$, inside of the mixing layer, are plotted as a function of the axial coordinate (*x/D*), as can be seen in the figs. 4.12 and 4.13. The fig. 4.12 shows that the Reynolds stress does not change for both modes up to *x/D=2.0*. After this point it reaches a plateau of about 1.5% for the helical mode, meanwhile under the flapping mode it still increases up to 3.4% in the field of analysis. This difference in the levels may be linked to different instabilities propagating downstream in the

mixing layer, as explained in the previous section. Concerning the flow anisotropy, in the fig. 4.13 one can see that both flows tend to value of 1.65, coherent with the results of Bellaud (1999) and agreeing with the literature that shows that jets are non isotropic flows.

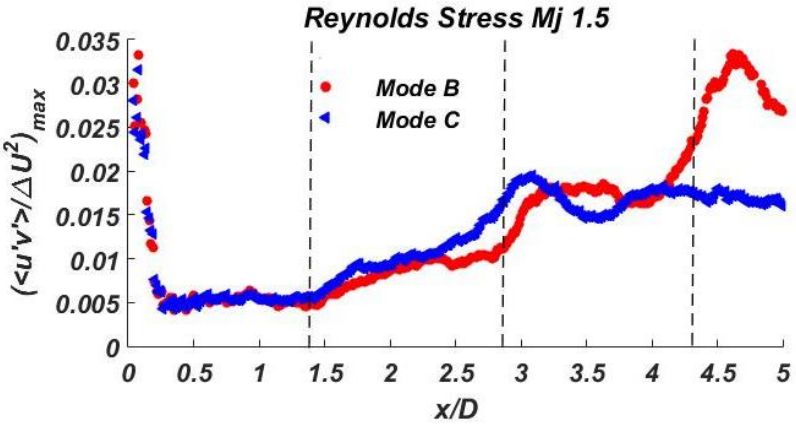

Figure 4. 12: maximum Reynolds stress in the mixing layer. Flapping (red) and helical (blue) modes. Shock positions represented by dashed lines from Prandt-Pack's theory.

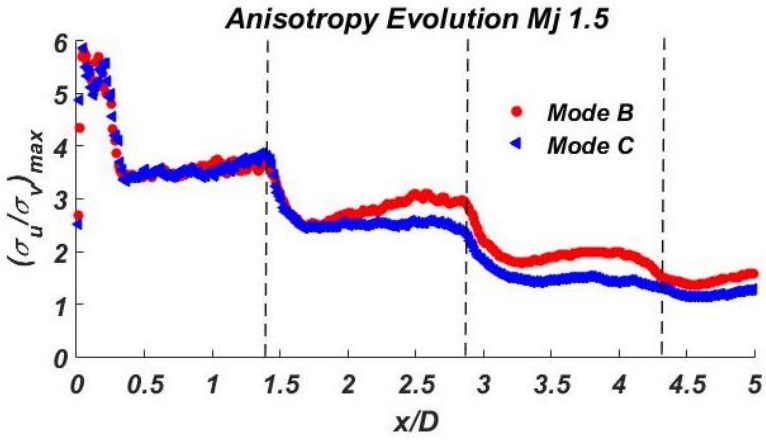

Figure 4. 13: maximum Anisotropy in the mixing layer. Flapping (red) and helical (blue) modes. Shock positions represented by dashed lines from Prandt-Pack's theory.

4.1.5 Conclusion

We have shown that the Screech jet dominant instability does not influence considerably the mean flow fields. No differences in the shock-cell spacing and in the overall flow topology were observed in the spatial window of analysis. Moreover, no large differences were noticeable in the evolution of the mixing layer. The standing wavelength measured for the helical mode represents 80% of the flapping mode, which is related to the fact that the Screech frequency is higher for the former mode. Furthermore, it was noticed that up to the second shock-cell the turbulence of both jets behave in a similar way, but downstream of this point the turbulence levels for the jet under flapping mode are higher than for the jet undergoing helical motion.

Hence, the results indicate that in the general way the Screech mode instability does not influence the mean flow topology but actually modifies characteristics of the fluctuating velocity. This behaviour may be explained by the differences in the coherent structures propagating in the mixing layer due to a different amplification of these ones according to different frequencies of the Screech.

4.2 Flow Structures

In this section we focus on the Screech mode effect on the coherent structures of the flow.

4.2.1 Hydrodynamic wavelength (L_h)

As exposed in the section **3.3.1**, we carry out an evaluation of the hydrodynamic wavelength (L_h) of the mixing layer structures in order to analyse the Screech modes effect. The fig. 4.14 presents the results of the correlation for the jets under *B* and *C* dominant Screech modes. The reference point is located in the standing waves. For both jets, the correlation coefficients are opposite in phase with reference to the jet axis, indicating the dominant instability of the flows. Moreover, interesting notice in this image that for the mode *C* the near-field is sloped downstream, a feature that can identify the helical dominant instability.

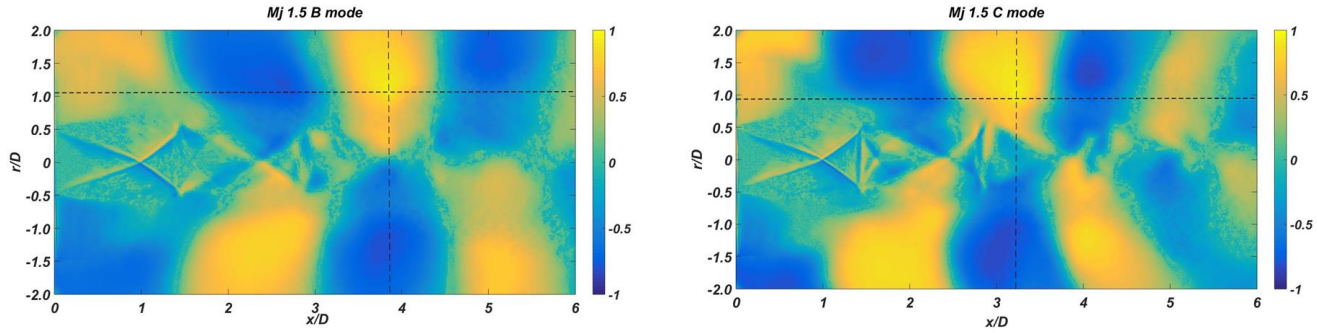

Figure 4. 14: correlation coefficient (*R*). The reference point is placed in the standing waves and represented by intersecting dashed lines. Jet under dominant flapping *B* (left) and helical *C* (right) Screech mode.

Measuring the spacing between the two peaks of the correlation in the fig. 4.14 the hydrodynamic wavelength (L_h) may be acquired. Thus, we obtain the values of $L_h/D=2.84$ and 2.30 for the jets under flapping and helical modes, respectively. This result reinforces the assumption that the different dominant Screech modes are linked to different coherent structures propagating in the flow.

4.2.2 Structures Dynamics

We evaluate in this section the dominant Screech mode effect on the coherent flow structures. To this end, POD (Proper Orthogonal Decomposition) is employed to extract the coherent structures of the flow. We then evaluate the influence of the flapping and helical modes on their characteristics. The field of view evaluated was $0 \leq x/D \leq 4$ and $-1 \leq r/D \leq 1$. This analysis window was chosen to enhance the representativity of the first POD modes as main coherent structures. The figs. 4.15 and 4.16 show the spatial POD functions of the two

first modes (leading pair), for jets under flapping and helical dominant Screech modes, respectively. Observing these images, we can notice that the energy is concentred inside of the mixing layer, corresponding to large coherent structures. It is also possible to see that the spatial functions depict the dominant mode instability of the jet (*m=1*) due to the fact that they are in opposite phase with reference to the jet axis. Moreover, the modes seem to be in phase quadrature, a necessary condition for the two modes to represent a convective motion. These two modes hence represent the coherent structures involved in the Screech feedback process, as already mentioned by Edgington-Mitchell et al. (2014a).

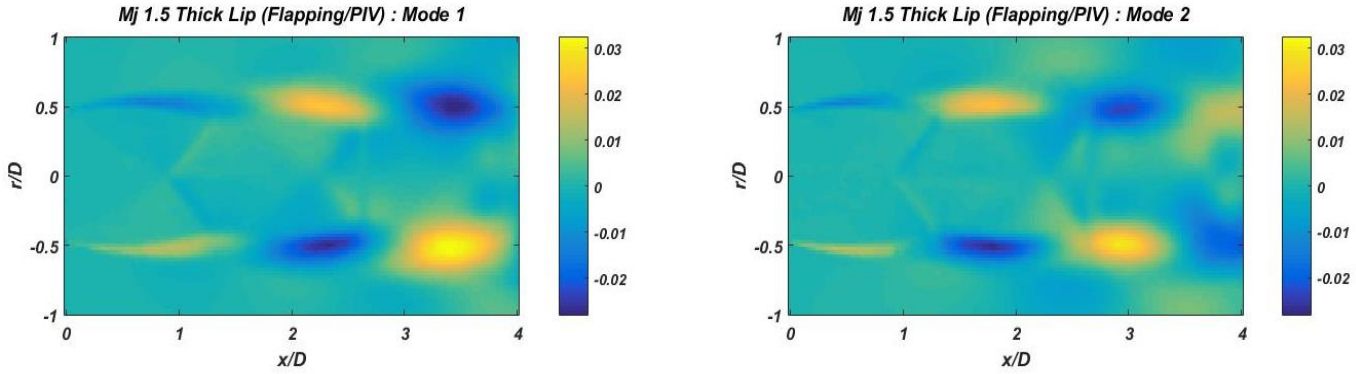

Figure 4. 15: streamwise spatial (ϕ_1 and ϕ_2) POD modes for *B* mode.

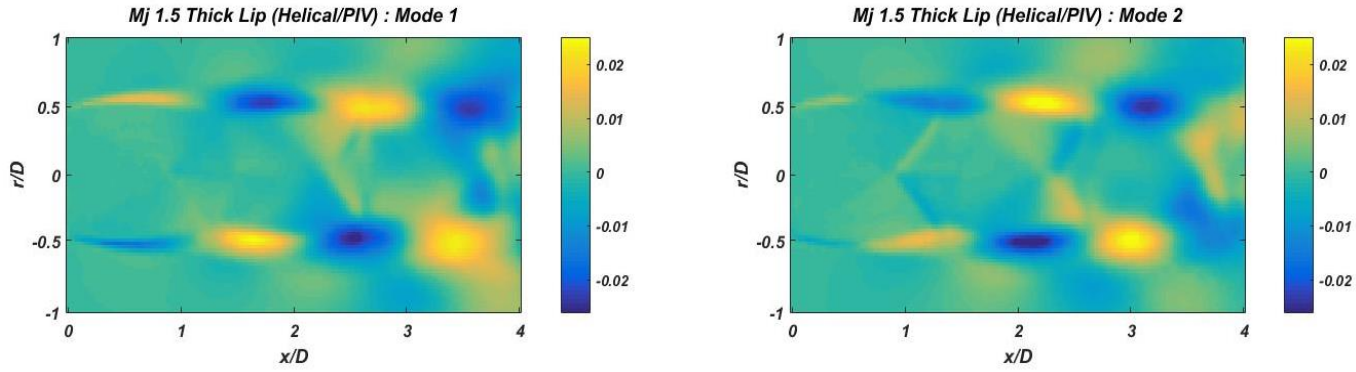

Figure 4. 16: streamwise spatial (ϕ_1 and ϕ_2) POD modes for *C* mode.

In order to evaluate the relation between the temporal coefficients of the leading pair (a_1,a_2) and the relative energy of these modes, the figs. 4.17 and 4.18 are presented. We oberserve that, regardless the Screech mode, the energy levels of the leading modes are similar and prominent compared to the other ones. Indeed, we can observe in the fig. 4.17, for mode *B*, that the first and second mode represent *18%* and *13%* of the total energy, respectively. For the Screech mode *C* (fig. 4.18) these levels reach *19%* and *16%* for the first and second POD modes, respectively. This means that both jets have coherent structures with similar dynamics, regardless of the Screech dominant mode.

As previously observed, the two first temporal POD modes of the jet undergoing flapping motion do not show a clear organization. The phase portrait (a_1,a_2) seems rather random as can be seen in fig. 4.17, contrary to the helical *C* mode (fig. 4.18) that scatters to form a Lissajous curve. This effect was already explained in the section ***3.3.2*** and is due to the disorganized precession movement of the jet associated to the flapping mode.

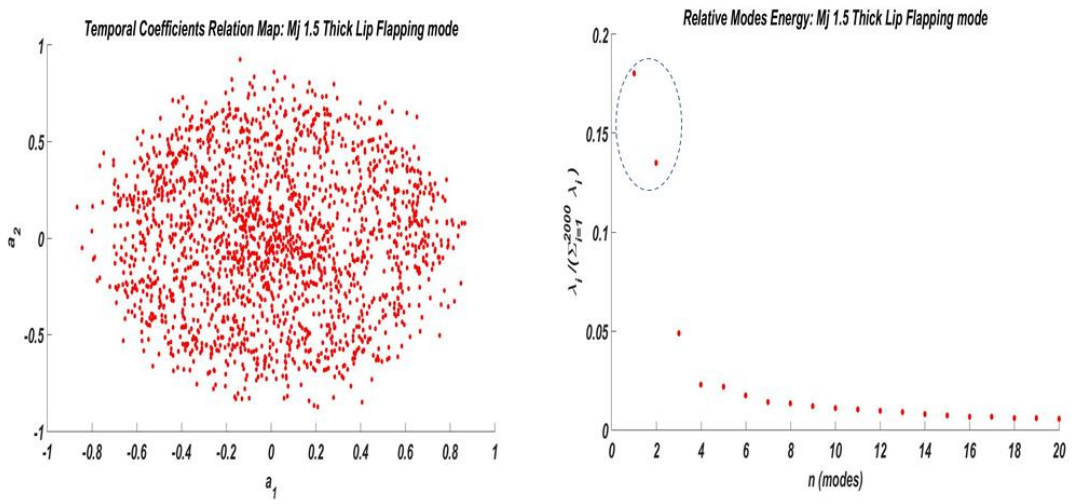

Figure 4. 17: phase portrait of the temporal coefficients *a1* and *a2* (left). Relative POD modes energy (right) for the flapping *B* Screech mode.

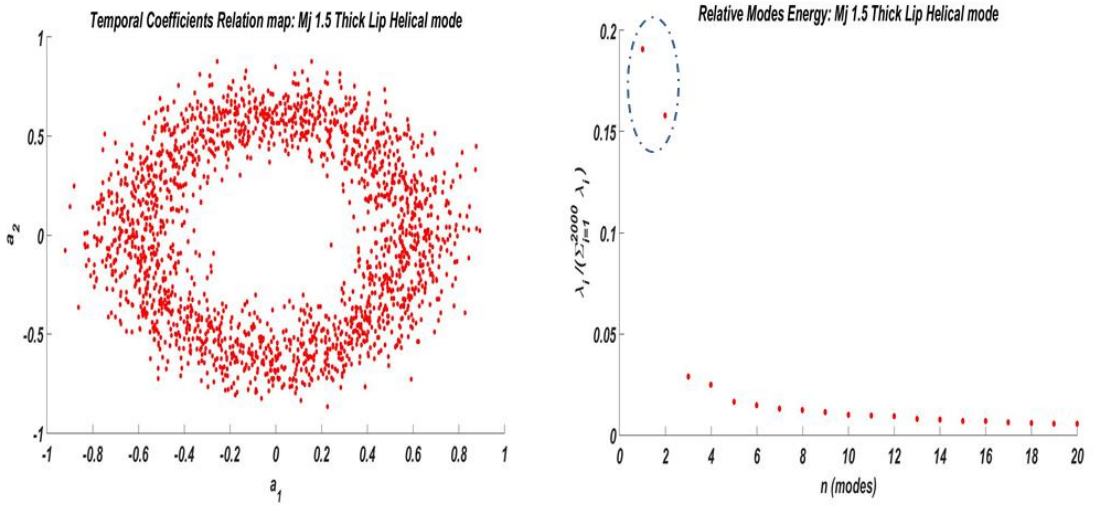

Figure 4. 18: phase portrait of the temporal coefficients *a1* and *a2* (left). Relative POD modes energy (right) for the helical *C* Screech mode.

4.2.3 Conclusion

The hydrodynamic wavelength measured suggested that the jets have different coherent structures propagating in the mixing layer. This result reinforces our previous observations that the dominant Screech mode affects the instabilities in the shear layer.

We observed, for both Screech modes, that the two first POD modes have non negligible relative energy level, compared to the other higher order POD modes, and the spatial POD functions are organized in such a way that they represent a convective motion. These two flows hence possess a similar dynamics of their coherent structures propagating inside of the mixing layer. Concerning the temporal coefficients, it was showed that the helical mode forms a Lissajous curve in the portrait (a_1,a_2), contrary to flapping one which shows a disorganized behaviour, as already presented in the nozzle lip thickness effect chapter.

Therefore, we could observe in this chapter that the dominant Screech mode have no large influence on the mean fields of the flow. However, when anaysed the fluctuation fields we notice that these effects are clearly remarked. Even though presenting similar dynamics, these coherent structures seem to be differents, maybe influenced by the different Screech frequencies of the modes. Thus, we can argue that the frequencies change the coherent structures of the mixing layer, but a question remains still open: which causes this frequencies changes? In the next chapter we investigate the possible mechanisms of Screech closure in order to give a suitable answer to this question.

5 CLOSURE MECHANISMS INVESTIGATION

In the previous chapters we have observed that the nozzle lip thickness affects the Screech (frequency and modes) as well as the flow characteristics (mixing layer thickness and turbulence intensity). Moreover, we also pointed out that the Screech mode influences the mixing layer turbulence, a behaviour that may be linked to the convection of different coherent structures excited at different frequencies. However, a question remains open: what mechanisms drive these Screech modes changes? This part of the present work attempts to provide an explanation to this particular behaviour.

To this aim, a study of a possible Screech closure mechanism by upstream-travelling waves, guided by the jet, is carried out. We make use of data obtained from the thick lip nozzle as we obtained suitable temporal coefficients and spatial POD functions for the analysis we want to conduct here. The Screech modes investigated are the axisymmetric (*A2*), helical (*C*) and the flapping mode (*B*), even though this latter presents a different feedback mechanism according to Shen & Tam (2002).

5.1 Upstream Neutral Waves Theory

Before exploring the upstream-travelling instabilities, it is worth presenting the theory about these neutral waves and their existence conditions. As already mentionned in the chapter 1, according to Shen & Tam (2002) the feedback Screech mechanism may be closed in two distinct ways. The first one consists of acoustic waves propagating outside of the jet. According to the authors, this model allows an accurate prediction of the Screech frequencies of the *A1* and *B* modes but not of the *A2* and *C* ones. The second closure mechanism supposes the existence of neutral waves, propagating upstream, with spatial support inside and outside of the flow. These neutral propagating instabilities, similar to acoustic waves, are characterized by real wavenumbers ($\kappa_i=0$) and angular frequencies ($\omega_i=0$). In this work, we label these kind of instabilities as "*neutral jet modes*".

The upstream travelling neutral jet modes were pointed out in the work of Tam & Hu (1989). Considering a simple vortex-sheet model they noticed the presence of these instabilities in supersonic flows. In the fig. 5.1 we can see the pressure eigenfunction of these waves, for a Mach number of $M=1.5$. One can remark that these instabilities have a signature inside and outside of the jet, enabling upstream information propagation even for supersonic flows. This enables a feedback closure mechanism. It is important to recall that these waves form the pair mode (*m,n*), corresponding to the azimuthal mode instability and the radial wavenumber, respectively. The radial wavenumber *n*, as observed by Towne *et al*. (2017), plays a role determining the number of the anti-nodes (lobes) in the pressure distribution. In other words, for each azimuthal wavenumber *m*, there is a countably infinite set of solutions $n=1,2,3,\ldots$ that are classified with effective radial wavenumber *n*, characterizing one pair (*m,n*) of neutral families. It is important to notice that Tam & Hu (1989) named this kind of instability as "*subsonic waves*". An important feature of these instabilities is that they only exist at narrow frequency ranges. This is their main difference to acoustic waves which exist for all frequencies.

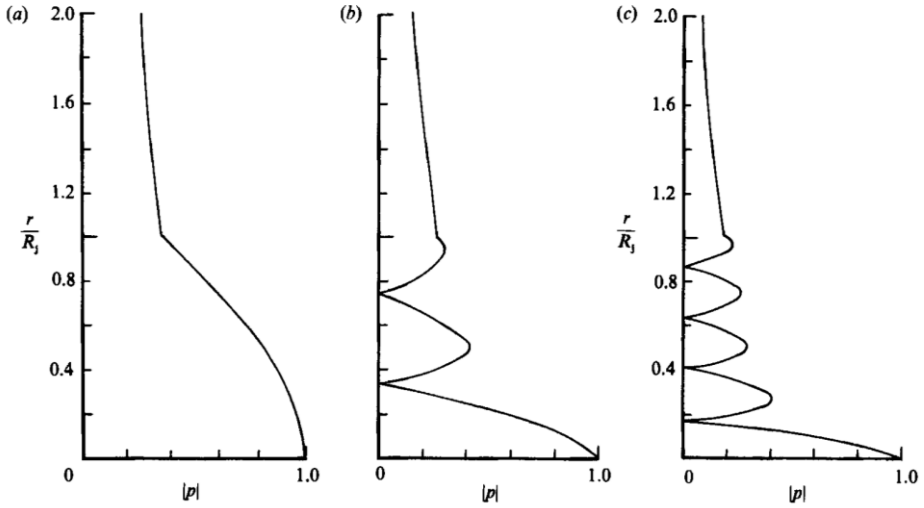

Figure 5. 1: pressure eigenfunction of upstream subsonic waves. Cold jets, Mach number 1.5. a) (0,1) mode, κRj=0.7, b) (0,3) mode, κRj=3.0, and c) (0,5) mode, κRj=5.5. Tam & Hu (1989).

As mentioned, the upstream travelling jet modes may be evaluated employing a cylindrical vortex-sheet model, considering a supersonic jet of velocity U_j and radius R bounded by a vortex-sheet (fig. 5.2). As such, this model constitutes an inviscid idealization of the jet as an infinitely thin vortex-sheet which separates the interior flow from the surrounding quiescent fluid. This model is based on the fact that perturbubations outside and inside of the flow are naturally linked by the continuity of the presure at the shear layer. Indeed, the radial profile of pressure *p(r)* does not present any discontinuity at the vortex sheet, in other words $p_i = p_o$ at *r/D=0.5*, where the subscripts "*i*" and "*o*" refer to conditions inside and outside of the flow, respectively. This is of course not the case for the radial velocity profile *u(r)*, where the model involves a discontinuity at *r/D=0.5*. Indeed, due to the infinitely thin shear-layer, $\partial u(r)/\partial r$ tends to infinity at the mixing layer. Moreover, one assumes that $U(r)=U_j$, $\rho(r)=\rho_j$, and $a(r) = a_j$ for $r<R$ as well as $U(r)=0$, $\rho(r)=\rho_\infty$, and $a(r) = a_\infty$ for $r>R$ (Michalke, 1970).

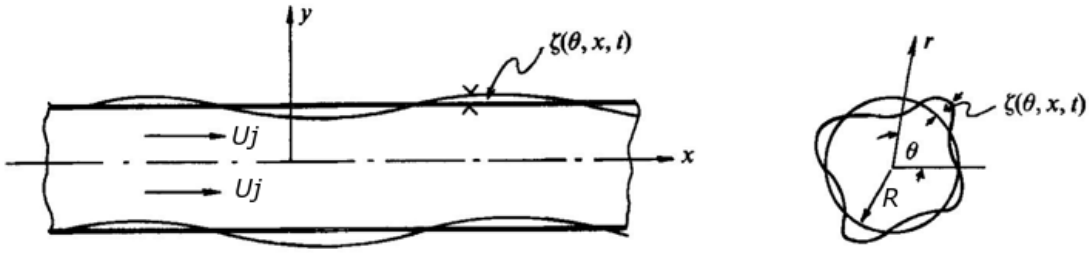

Figure 5. 2: sketch of cylindrical vortex-sheet. Tam & Hu (1989) modified.

Considering infinitely small disturbances superimposed on the basic flow, such that disturbed quantities may be written as $u_x = U_j + u'_x$, $u_r = u'_r$, $u_\theta = u'_\theta$, $p = \bar{p} + p'$, $T = \bar{T} + T'$ and $\rho = \bar{\rho} + \rho'$ where the "prime" represents the disturbance of the components of velocity, pressure, temperature and density respectively, and where the "overbar" is the average operator applied to the corresponding flow variables. As such, the linearized disturbance equations for an isentropic flow of a perfect gas are obtained (Lessen *et al*., 1965):

Continuity

$$\frac{\partial \rho'}{\partial t} + U_j \frac{\partial \rho'}{\partial x} = -\bar{\rho}[\frac{\partial u_x'}{\partial x} + \frac{1}{r}\frac{\partial (r u_r')}{\partial r} + \frac{1}{r}\frac{\partial u_\theta'}{\partial \theta}] \quad \text{eq. 5.1}$$

Momentum

$$\bar{\rho}\left(\frac{\partial u_x'}{\partial t} + U_j \frac{\partial u_x'}{\partial x}\right) = -\frac{\partial p'}{\partial x} \quad \text{eq. 5.2}$$

$$\bar{\rho}\left(\frac{\partial u_r'}{\partial t} + U_j \frac{\partial u_r'}{\partial x}\right) = -\frac{\partial p'}{\partial r} \quad \text{eq. 5.3}$$

$$\bar{\rho}\left(\frac{\partial u_\theta'}{\partial t} + U_j \frac{\partial u_\theta'}{\partial x}\right) = -\frac{1}{r}\frac{\partial p'}{\partial \theta} \quad \text{eq. 5.4}$$

Energy

$$\bar{\rho} c_v \left(\frac{\partial T'}{\partial t} + U_j \frac{\partial T'}{\partial x}\right) = -\bar{p}(\frac{\partial u_x'}{\partial x} + \frac{u_r'}{r} + \frac{\partial u_r'}{\partial r} + \frac{1}{r}\frac{\partial u_\theta'}{\partial \theta}) \quad \text{eq. 5.5}$$

State

$$\frac{p'}{\bar{p}} = \frac{\rho'}{\bar{\rho}} + \frac{T'}{\bar{T}} \quad \text{eq. 5.6}$$

The disturbances are considered to have a wave behaviour, so that they can be inferred as:

$$[u_x', u_v', u_\theta', p', \rho', T'] = [\alpha(r),\ \beta(r),\ \delta(r), \pi(r), \varepsilon(r), \mu(r)] e^{i(\kappa x + m\theta + \omega t)} \quad \text{eq. 5.7}$$

where in the above equation, κ is the axial wavenumber, *m* the azimuthal mode and ω the angular frequencies. Moreover, the functions $\alpha(r)$, $\beta(r), \delta(r), \pi(r), \varepsilon(r)$ and $\mu(r)$ are the disturbance complex amplitudes of the physical quantities.

Developping the eq. 5.7 Lessen *et al.* (1965), as well as Michalke (1970), pointed out that the pressure amplitude function $\pi(r)$ is governed by a classical wave equation in a fluid at rest outside of the jet and by a convective one inside of this one. In addition to these differential equations, the problem is closed by the conditions of continuity at the vortex-sheet. As seen previously, the first one is the dynamic condition that imposes the pressure disturbances to be equal on both sides of the vortex-sheet, in other words such that $p_i = p_o$ $(\pi_i(R) = \pi_o(R))$ at *r/D=0.5*. The second one is a kinematic condition that takes into account that the rate of change of the radial displacement $\zeta(\theta, x, t)$ is equal to the radial velocity disturbance at the vortex-sheet (see fig. 5.2). This yields, at *r = R*:

$$p_i = p_o \quad \text{eq. 5.8}$$

$$\frac{1}{\overline{\rho_o}}\frac{\partial p_o}{\partial r} = \frac{\partial^2 \zeta}{\partial t^2} \quad \text{eq. 5.9}$$

$$-\frac{1}{\overline{\rho_i}}\frac{\partial p_i}{\partial r} = (\frac{\partial}{\partial t} + U_j \frac{\partial}{\partial x})^2 \zeta \quad \text{eq. 5.10}$$

This set of equations then leads to the resolution of an eigenvalue problem conducting to a dispersion relation giving the pair κ-ω that characterizes the nature of the waves in the flow. Therefore, the upstream travelling neutral jet modes are part of the solution of the vortex-sheet dispersion relation, (eq. 5.11 and 5.12), first derived by Lessen *et al.* (1965):

$$\mathcal{D}_j(\kappa, \omega, M, T, m) = 0 \qquad \text{eq.5.11}$$

with

$$\mathcal{D}_j = \frac{1}{(1-\frac{\kappa M}{\omega})^2} + \frac{1}{T}\frac{I_m\left(\frac{\gamma_i}{2}\right)\left[\frac{\gamma_0}{2}K_{m-1}\left(\frac{\gamma_0}{2}\right)+mK_m\left(\frac{\gamma_0}{2}\right)\right]}{K_m\left(\frac{\gamma_0}{2}\right)\left[\frac{\gamma_i}{2}I_{m-1}\left(\frac{\gamma_i}{2}\right)+mI_m\left(\frac{\gamma_i}{2}\right)\right]} \qquad \text{eq.5.12}$$

where $\gamma_0 = \sqrt{\kappa^2 - \omega^2}$ and $\gamma_i = \sqrt{\kappa^2 - \frac{1}{T}(\omega - M\kappa)^2}$. In the equations above I_m and K_m are m^{th} order modified Bessel functions of the first and second kind, respectively, and m is the azimuthal wavenumber. M is the acoustic Mach number (U_j/a_∞) and T is the jet temperature ratio (T_j/T_∞). The jet Mach number is a function of the acoustic Mach number and the temperature ratio: $M_j = Uj/aj = M/\sqrt{T}$. It needs to be stressed that this model has been widely used for stability analysis of subsonic and supersonic jets among which one can cite Michalke, (1970), Towne *et al.* (2017) and Jordan *et al*. (2018). It is important to notice that the dispersion relation depends on the jet Mach number. Subsequently the frequencies and wavenumber of the waves solutions of the eq. 5.12 are also dependent on *Mj*. In other words, the condition of existence of the upstream neutral waves depends on the flow conditions considered. Solving the eq. 5.12, we obtain the dispersion curve as shown in fig. 5.3 for *Mj=1.5*, where we present the roots of the dispersion relation in the κ-ω plane. Moreover, for a given κ-ω pair, the corresponding eigenfunctions are obtained for the streamwise velocity component:

$$\hat{u}(r) = \begin{cases} \frac{-\kappa I_m(\gamma_i r)}{M\kappa-\omega} & for\ 0 \le \frac{r}{D} \le 0.5 \\ \frac{\kappa K_m(\gamma_o r) I_m(\frac{\gamma_i}{2})}{\omega K_m(\frac{\gamma_o}{2})} & for\ \frac{r}{D} \ge 0.5 \end{cases} \qquad \text{eq. 5.13}$$

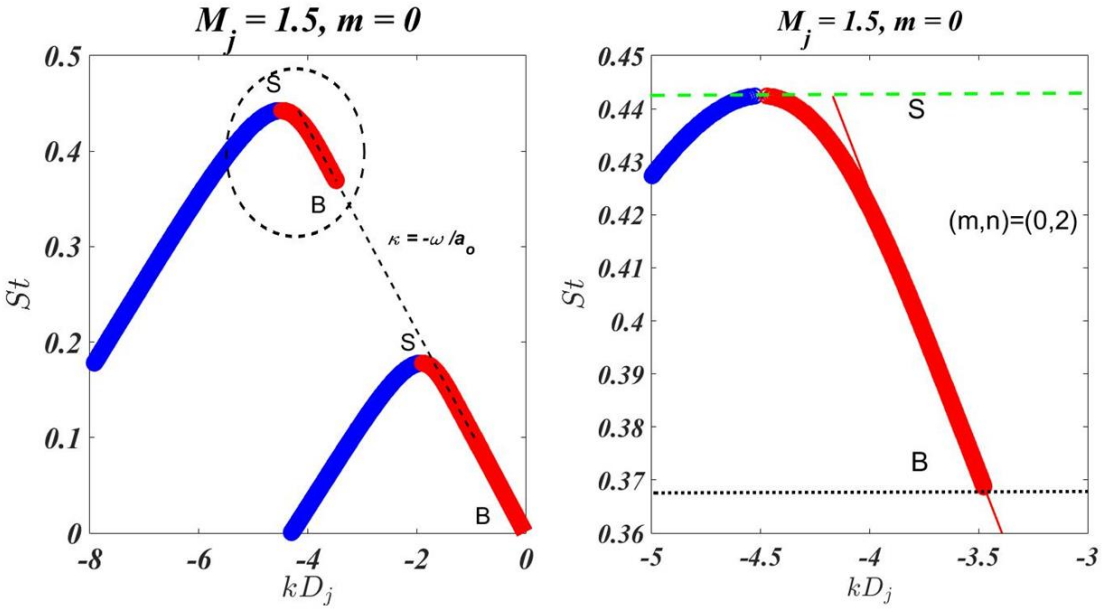

Figure 5. 3: Left: dispersion relations of axisymmetric jet neutral modes for *Mj* =1.5 and Temperature ratio (T) equals to 1. Dashed line represents the sonic condition ($\kappa=-\omega/a_0$), S and B represent the saddle and branch points, respectively. Right: allowable frequencies of upstream neutral waves (*m,n=0,2*). Green dashed line represents the upper frequency limit (saddle point) and black dashed line represents the bottom frequency limit (branch point). Taken from Mancinelli (2018), internal report.

It is possible to notice in fig. 5.3 that the jet neutral modes are constitued by instabilities propagating downstream (κ+) and upstream (κ-), where we consider here the fully expanded jet diameter D_j to get the nondimensional wavenumber κD_j. The direction of energy propagation is given by the sign of the slopes of the dispersion curves, i.e. the group velocity. For instance, waves with $\Delta St/\Delta\kappa D_j > 0$ are able to propagate energy downstream and those with $\Delta St/\Delta\kappa D_j < 0$ propagate energy upstream of the jet. The points of zero slope ($\Delta St/\Delta\kappa D_j = 0$) represents saddle points (*S*) in the complex κ plane, where the instabilities κ+ and κ- coalesce (Towne *et al*., 2017). Saddle points are important as they represent cut-on frequencies region in the jet resonance study, or more precisely here the cut-on frequency of upstream-travelling waves (κ-). In other words, they give the upper limit of the allowable frequencies for which the upstream neutral jet waves can exist. On the other hand, the bottom limit of these waves existence are the branch points (*B*), representing the cut-off frequencies for the jet resonance. They give the lower limit of the allowable frequencies for which the upstream neutral jet waves can exist. We can observe in fig. 5.3 that for the jet at *Mj =1.5* the dispersion model predicts for the instablity (*m=0,n=2*) a cut-on frequency (*St*) of 0.442 and a cut-off of 0.368, approximately.

Therefore, from the cylindrical vortex-sheet model, it is possible to find out the branch and saddle points that delimits the non-dimensional frequencies (*St*) where these upstream neutral waves (axisymmetrics and helical) can exist. Gojon *et al*. (2018) used this model to compare the experimental data from Ponton & Seiner (1992) and Powell *et al*. (1992) with the dispersion relation. They observed an appreciable agreement between the Screech frequencies of the axisymmetric and helical modes with the upstream travelling waves families. Moreover, from numerical simulations at $M_j = 1.56$, under *C* and *u* modes, they pointed out the presence of upstream waves propagating at the ambient speed of sound, consistent with the jet neutral

modes. However, an experimental observation of these waves and their possible relation with Screech phenomenon is still lacking.

This task was carried out by Edgington-Mitchell *et al.* (2018) for *A1* and *A2* Screech modes. The authors, employing a spatial Fourier decomposition of POD obtained from the velocity fluctuations, observed the signature of the upstream travelling waves in excellent concordance with vortex sheet eigenfunctions (eq. 5.13). This provides a strong evidence that these waves exist and are very likely used as Screech closure mechanism for both axisymmetric modes. This contradicts Shen & Tam (2002) that mentioned that only the mode *A2* is driven by this kind of instabilities.

Following Shen & Tam (2002) and Edgington-Mitchell *et al.*, (2018), the Screech tones *A1*, *A2* and *C* may be the result of a resonance between Kelvin-Helmholtz instabilities and upstream-travelling neutral jet waves, where the boundary conditions for the resonance are the nozzle and a shock location (Mancinelli, 2018 internal report). The fig. 5.4 presents a sketch of the jet with the presence of these mentioned waves. Thus, the focus of the following work is to investigate experimentally the presence of these upstream neutral instabilities in the jet for various NPR in order to evaluate their possible involvement in the Screech closure mechanism.

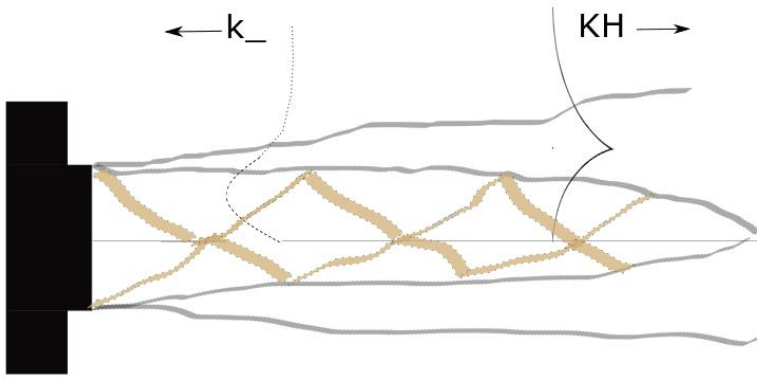

Figure 5. 4: sketch of Kelvin-Helmholtz (*KH*) and upstream travelling neutral waves (κ-).

5.2 Upstream Neutral Jet Waves and Screech Modes

In this section, we present a comparison between the allowable frequencies of the neutral waves (κ-) and the acoustic pressure (PSD) radiated by the jet obtained in the chapter 3. The limits of the allowable frequencies range (saddle and branch points) are ploted onto the Screech cartography of the two first azimuthal modes (*m=0* and *m=1*), as can be seen in figs. 5.5 and 5.6.

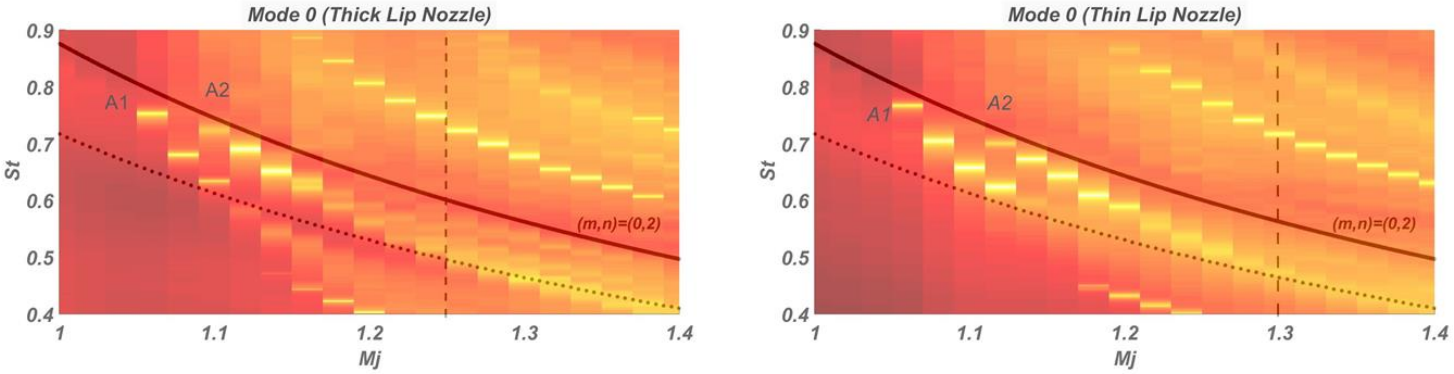

Figure 5. 5: allowable frequency ranges for axisymetric (*m=0,n=2*) upstream-travelling jet neutral waves overlaped on the PSD of the acoustic pressure cartography of the axisymmetric azimuthal Fourier mode. Thick (left) and thin (right) lip nozzle. Solid and dashed lines represent saddle and branch points, respectively.

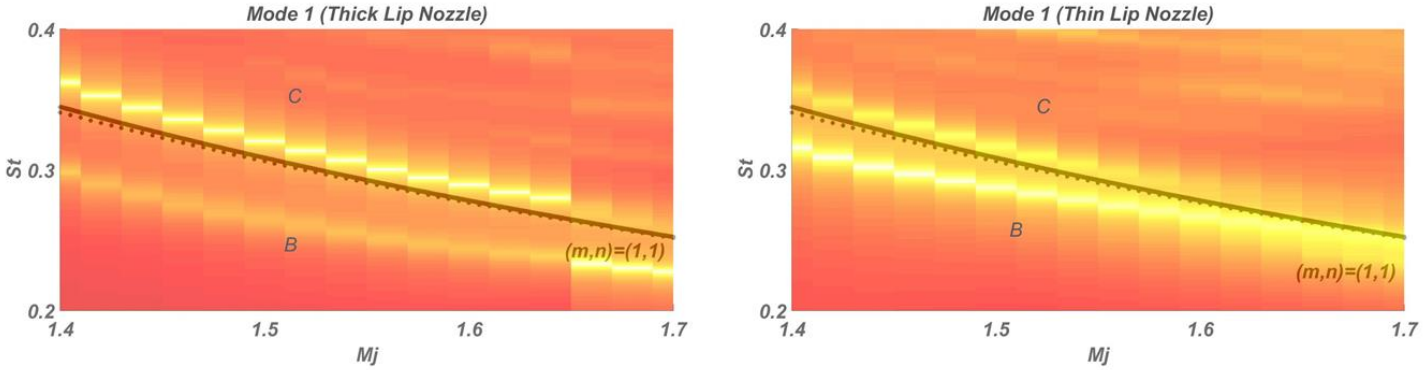

Figure 5. 6: allowable frequency ranges for helical (*m=1,n=1*) upstream-travelling jet neutral waves overlaped on the PSD of the acoustic pressure cartography of the azimuthal Fourier mode 1. Thick (left) and thin (right) lip nozzle. Solid and dashed lines represent saddle and branch points, respectively.

In the figures above, the region of the allowable frequencies of the upstream instabilities are delimited by dashed lines, representing the branch points (*B*), and by solid lines which correspond to the saddle points (*S*). In fig. 5.5, an excellent agreement is found between the axisymmetric modes *A1* and *A2* with the family of upstream-travelling waves (*m=0,n=2*): these modes are inside of the allowable frequencies region, regardless of the lip thickness. This result is coherent with the work of Edgington-Mitchell *et al*. (2018). In other words, it suggests that the axisymmetric upstream-travelling waves can drive the Screech feedback mechanism for the *A1* and *A2* modes. The fact that *A1* and *A2* arise in between the branch and the saddle points tracks is a solid argument for the fact that axisymmetrics modes can not be driven by acoustic waves: acoustic wave does not have narrow frequency range existence.

Another insightful result that can be remarked from the fig. 5.5 is that the concordance between the model and the experimental results match differently, according to the nozzle: we can observe that the concordance between the experimental results and the vortex sheet model extends up to $M_j=1.3$ for the thin lip nozzle, whereas value is about *1.25* in the thick lip case. This behaviour evidences that the model agrees well with experimental data when the initial theoretical assumptions are satisfied. Indeed, the effects of the nozzle lip on the spreading of the

mixing layer (as already mentioned in the chapter 3) induce differences between the real shear layer thickness and the assumptions considered in the model (infinitely thin shear layer). This may explain the better concordance between the model and the Screech frequencies generated by the thin lip nozzle as well as corroborate with the observations made in the chapter 3: the signature for the mode *A2* is much more remarkable for the jets generated by the thin lip nozzle. Moreover, this fact may also explain the modal changes in the screeching jets (*A1*, *A2* and *C*) observed by previous authors. For example, Ponton & Seiner (1992) observed different transitions between *B*-*C* Screech modes varying with the lip thickness.

Considering the azimuthal mode *1*, we can see in fig. 5.6 that the model does not provide a correct prediction neither helical (*C*) nor flapping (*B*) Screech modes, even though the former is closer to the upstream instability allowable frequencies (*m=1,n=1*) than the latter. It is worth mentioning that the vortex-sheet model predicts a range of allowable frequencies for this family of instabilities very narrow. Furthermore, as the helical *C* Screech mode frequency obtained experimentally is extremely close to the theoretical region of allowable frequencies, one can ask the question whether or not this upstream instability may play a role as closure mechanism.

Summarizing, it is possible to constate that the *A1* and *A2* Screech modes seem to be conditioned by the presence of the upstream-travelling jet neutral waves, indicating that these instabilities may be responsible for the closure of the Screech feedback loop. The mismatch between the helical (*C*) as well as the flapping (*B*) Screech mode and the predicted allowable frequency range was observed, even though the Screech frequency of the helical (*C)* mode is very close to the region (*m=1, n=1).* Nevertheless, we will carry out in the next section a study to extract the support of the upstream waves in the experimental data to verify if the frequency mismatch is more than fortuitous.

5.3 Signature of Upstream Neutral Waves in the Flow

In this part, we try to extract information about the upstream neutral waves in the jet flow. For this, we consider the Screech modes *A2* (axisymmetric), *C* (helical) and *B* (flapping), corresponding to *Mj=1.13* and *1.5*. The next section presents the background theory to transform the POD spatial functions in the Fourier domain in order to separate the upstream- and downstream-propagating instabilities. This method of analysis was employed by Edgington-Mitchell *et al*. (2018) for axisymmetrics *A1* and *A2* screeching jets. Afterwards, the upstream and the downstream coherent waves associated to the Screech phenomenon are presented. Finally, the upstream instabilities obtained are compared with streamwise velocity eigenfunction associated to the upstream neutral jet modes of the vortex-sheet dispersion relation, in order to verify the presence of these instabilities for several *NPR* conditions.

5.3.1 Spatial Fourier Decomposition (κ-ω_s Decomposition)

The coherent fluctuations associated with the Screech tones in the PIV data are obtained by a snapshot Proper Orthogonal Decomposition (POD). Assuming that the first two POD modes represent the coherent structures associated with the aeroacoustic feedback process (Edgington-Mitchell *et al.* 2014a) and that the modal pair represents a periodic phenomenon at the angular Screech frequency ($\omega_s=2\pi f_s$) (Jaunet *et al*., 2016), it is possible to obtain the velocity field ($U^c(x,y,t)$) associated with these structures by forming a low order reconstruction:

$$U^c(x,y,t) = \sum_{n=1}^{2} a_n(t)\Phi_n(x,y) \quad \text{eq. 5.14}$$

If both, a_1 and a_2, and, Φ_1 and Φ_2, are in phase quadrature, we can form the complex coefficients $\alpha = a_1 - ia_2 = \hat{a}e^{-i\omega_s t}$ and eigenfunctions $\varphi = \Phi_1 + i\Phi_2$, allowing the eq. 5.14 to be rewriten as:

$$U^c(x,y,t) = \mathcal{R}e(\hat{a}e^{-i\omega_s t}\sum_{\kappa}\hat{q}_k^c(y)e^{i\kappa x}) \quad \text{eq. 5.15}$$

where $\mathcal{R}e()$ is the real part of the complex number and

$$\hat{q}_k^c(y) = \sum_x \varphi\,(x,y)e^{-ikx} \quad \text{eq. 5.16}$$

The eq. 5.16 is the spatial Fourier transform of the complex POD functions φ. Applying this transform, the wavenumbers spectrum associated with the streamwise and transverse velocity fluctuations ($\hat{u}_k^c$ and $\hat{v}_k^c$, respectively) at the Screech frequency can be obtained. Since the wavenumbers spectrum is known, the Screech instabilities can be separated according to their propagation direction where negative phase speeds require $\kappa<0$, contrary to the positive case where $\kappa\geq 0$. As such, the downstream and upstream propagative coherent velocity fluctuations, $u_d^c(x,y,t)$ and $u_u^c(x,y,t)$, respectively, are obtained using the following equation:

$$U^c(x,y,t) = \mathcal{R}e(\hat{a}e^{-i\omega_s t}[\sum_{\kappa<0}\hat{q}_k^c(y)e^{i\kappa x} + \sum_{\kappa\geq 0}\hat{q}_k^c(y)e^{i\kappa x}]) \quad \text{eq. 5.17}$$

and:

$$u_u^c = \mathcal{R}e\left(\hat{a}e^{-i\omega_s t}\hat{u}_u^c\right) = \mathcal{R}e\left(\hat{a}e^{-i\omega_s t}\sum_{\kappa<0}\hat{q}_k^c(y)e^{i\kappa x}\right) \quad \text{eq. 5.18}$$

$$u_d^c = \mathcal{R}e\left(\hat{a}e^{-i\omega_s t}\hat{u}_d^c\right) = \mathcal{R}e\left(\hat{a}e^{-i\omega_s t}\sum_{\kappa\geq 0}\hat{q}_k^c(y)e^{i\kappa x}\right) \quad \text{eq. 5.19}$$

The next sections present the downstream- and upstream-propagative waves ($\hat{u}_d^c$ and $\hat{u}_u^c$) obtained experimentally. Then, the upstream coherent waves $\hat{u}_u^c$ are compared to the streamwise velocity eigenfunction associated to the upstream jet neutral modes.

5.3.2 Axisymmetric Screech Mode (A2)

The results of the κ-ω_s decomposition are presented in this section for the jet at *Mj = 1.13*, corresponding to the axisymmetric Screech mode *A2*. The field analysed is between *x=0* and *x=3.5D*, as such a spatial window enables to acquire spatial POD functions (Φ) and temporal coefficients representing at the best the convective movement of the structures. The first and second spatial POD modes are depicted in fig. 5.7, where it is clear that the jet undergoes an axisymmetric motion. The phase relation between the temporal coefficients a_1a_2 as well as the relative modes energy are depicted in fig. 5.8. In this figure, one can notice that the leading modes have a similar and noticeable energy and that the two temporal coefficients are in phase quadrature, reinforcing the fact that these POD modes represent the coherent structure associated with the aeroacoustic feedback process.

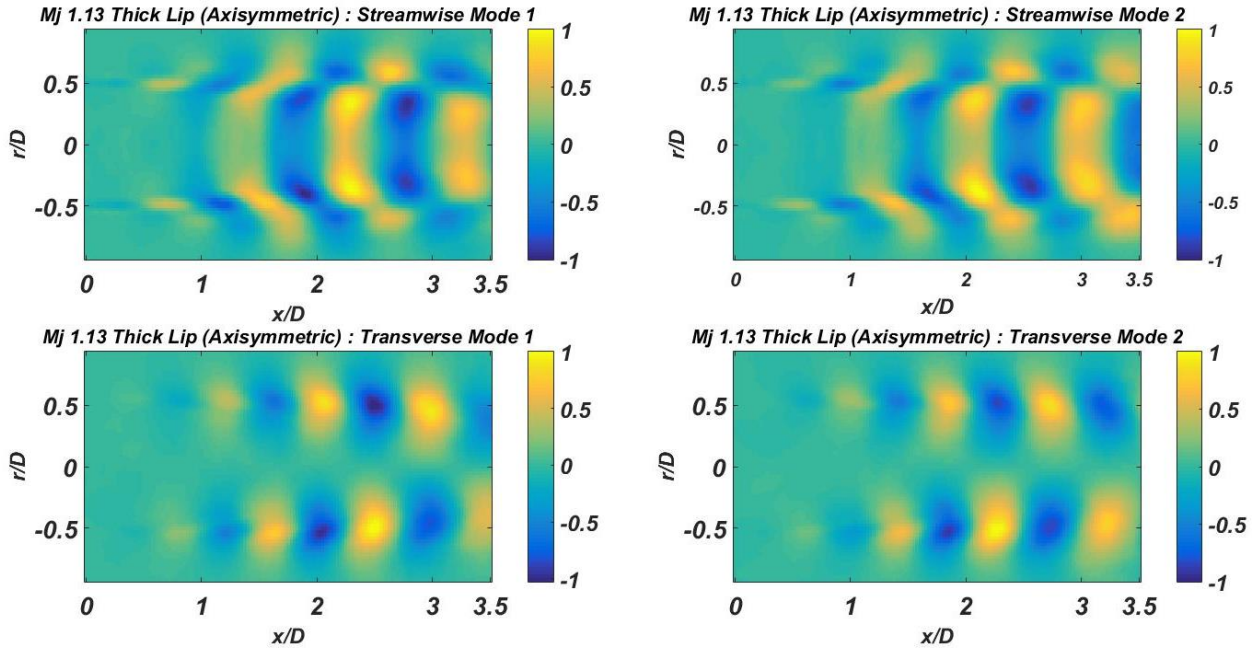

Figure 5. 7: spatial POD functions (Φ) of the modes 1 and 2, for the streamwise (top) and transverse (bottom) velocity components. Each mode is individually normalized by its respective maximum value of Φ .

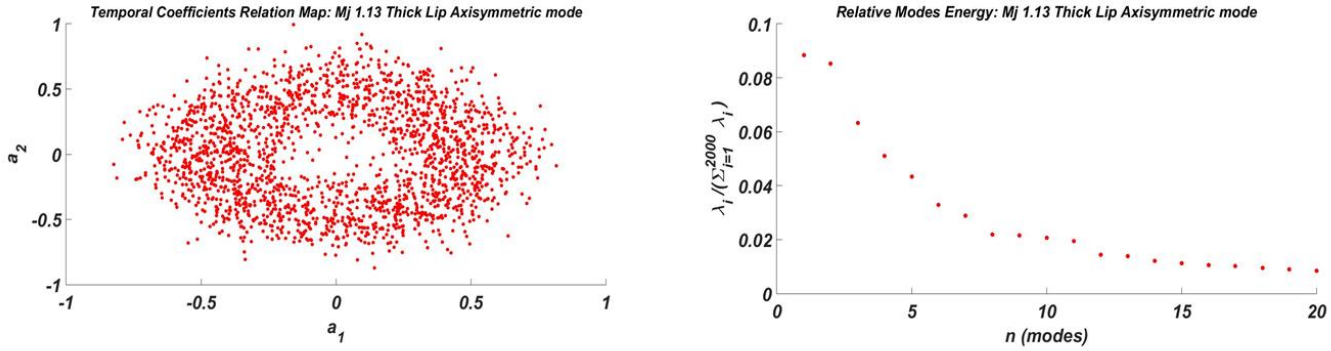

Figure 5. 8: temporal coefficients a_1a_2 (left) and relative modes energy (right) for *Mj=1.13*, *A2* mode, thick lip nozzle.

The spatial Fourier transform (eq. 5.16) is applied to the composed function $\varphi = \Phi_1 + i\Phi_2$. Then, the spatial wavenumbers associated to the streamwise component of velocity ($\hat{u}_k^c$) are obtained. In the fig. 5.9 we plot the amplitude of $\hat{u}_k^c$ as a function of the spatial wavenumber kD_j where the sign of the kD_j determines the sign of the phase velocity, indicating the direction of the propagation. In other words, the sign of kD_j indicates the waves travelling direction. From this figure it is possible to notice a remarkable energy for positive phase speed ($\kappa>0$), at a velocity lower than the speed of sound. Note that the sound waves at the Screech frequency have a wavenumber of $\kappa D_j = 4.1$. Moreover, in the fig. 5.9 we observe that the peak ampltitude is located in the mixing layer ($r/D \approx 0.5$). This is associated to the propagation of Kelvin-Helmholtz instabilities. Unfortunately, due to resolution restrictions, it is not possible to perform a suitable estimation of the convective velocity (U_c) of the Kelvin-Helmholtz instabilities. Indeed, due to the large value of ΔkDj, the incertitude in the phase

velocity of Kelvin-Helmholtz instabilities $\Delta U_c=\omega_s/\Delta k$ is too high to enable an accurate estimation of the convective velocity. There is also a noticeable energy in the negative k region, associated to upstream propagation (dashed ellipse in figure). Note that this propagation occurs at a phase velocity near to the sound velocity (vertical dashed line, at $\kappa D_j = -4.1$). Since the energy is located outside and inside of the jet, this suggests the presence of the upstream jet neutral instabilities (*k-)*.

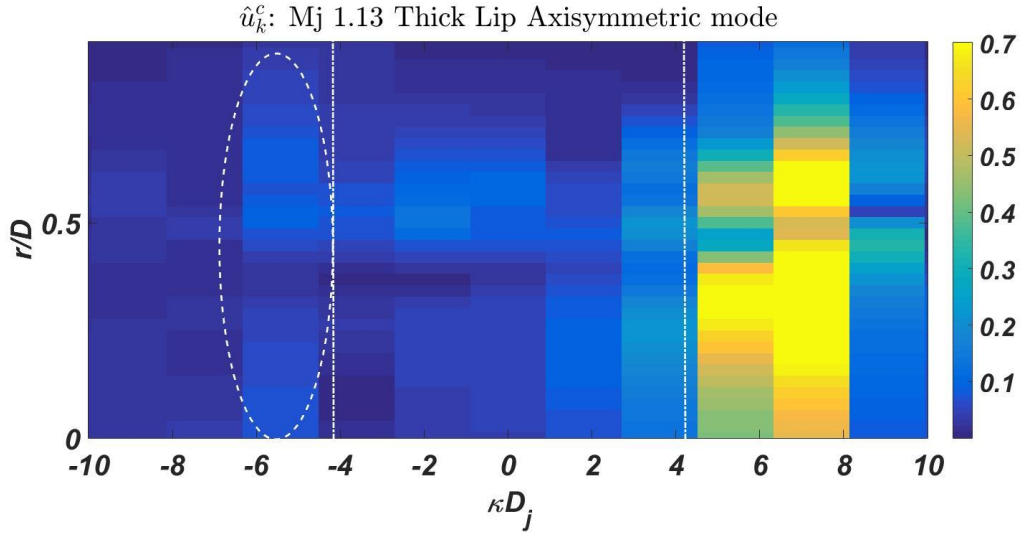

Figure 5. 9: wavenumber spectrum of the coherent streamwise velocity ($\hat{u}_k^c$). Vertical dashed lines represent the wavenumbers associated to the speed of sound at the Screech frequency in the upstream (negative values) and downstream (positive values) directions.

Since the wavenumber spectrum is known, the downstream and upstream coherent waves, $\hat{u}_d^c$ and $\hat{u}_u^c$, respectively, can be obtained. In the case of downstream waves this is made from the inverse Fourier transform of the positive wavenumbers ($kD_j \geq 0$). The result is plotted in the fig. 5.10. One can remark that this downstream wave, propagating in the mixing layer, is very similar to the waves associated to the Kelvin-Helmholtz instabilities. Indeed, it is possible to notice in this figure the growth, saturation and decay of this instability, consistent with the Kelvin-Helmholtz behaviour.

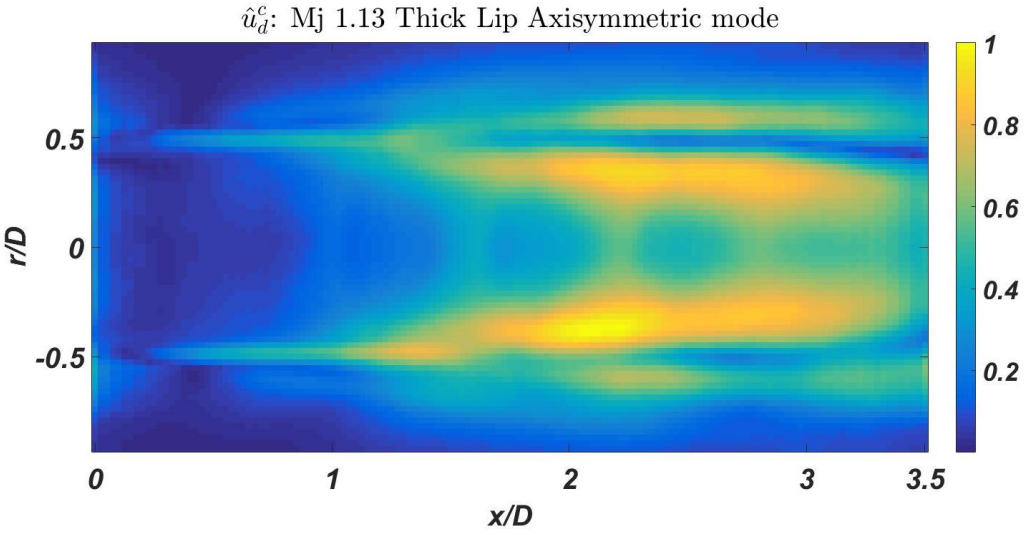

Figure 5. 10: amplitude of the downstream travelling waves normalized by the maximum value.

In order to reconstruct the upstream travelling neutral waves, two discrete values of kD_j=-5.45 and -7.25 were considered before Fourier inversing. These points were chosen because they are the closest availabe to the wavenumber of the sound waves kD_j=*-4.1*, where we expect, as showed in fig. 5.3, the jet modes to lie in. The upstream-travelling waves are depicted in fig. 5.11. The results show that the upstream instability waves present a strong energy level in the jet axis (*r/D=0)*, decreasing and increasing in the radial direction before reaching the mixing layer (*r/D=0.5).* The topology of the image is quite similar with those found by Edgington-Mitchell *et al.* (2018) (fig. 5.12) for *Mj = 1.09* and *1.14*.

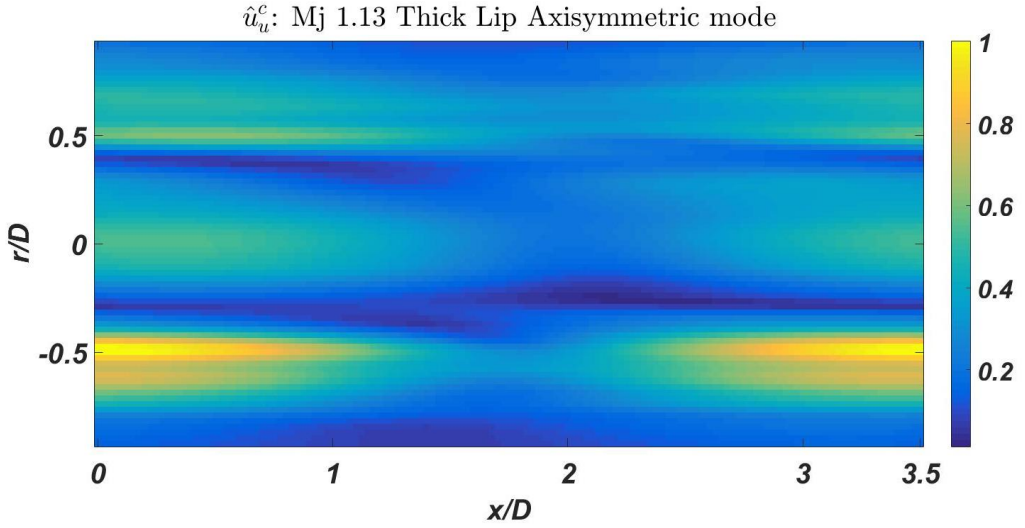

Figure 5. 11: amplitude of the upstream-travelling waves component associated to the negative wavenumbers (kD_j=-5.45 and -7.25), normalized by the overall maximum value.

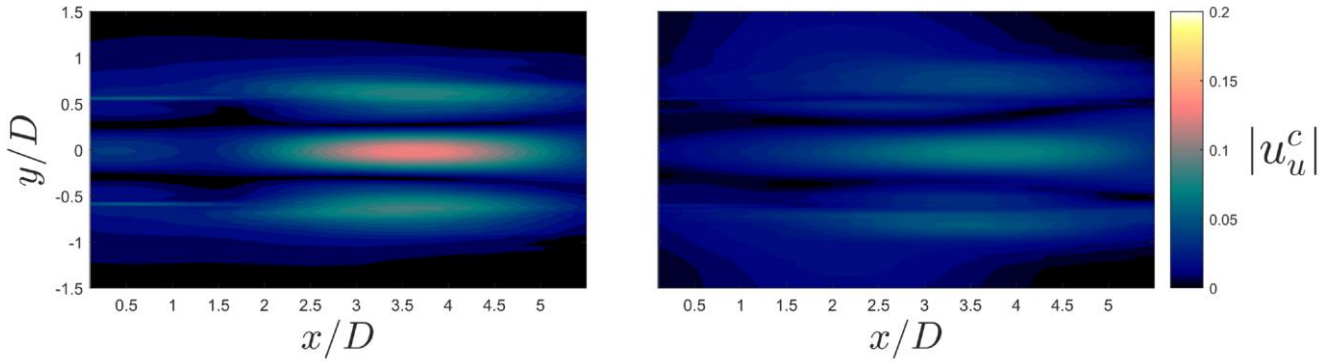

Figure 5. 12: amplitude of the upstream-travelling waves component associated to the negative wavenumbers (k-), normalized by the maximum value of u_d^c. M_j *=1.09* left and *1.14* right. Edgington-Mitchell et al. (2018).

In order to validate the results obtained, a comparison between the experimental data and the model is carried out, where the upstream-travelling waves ($\hat{u}_u^c$) profiles are compared to the vortex-sheet eigenfunction, provided from eq. 5.13. As such, we chose the eigenvalue κ at the Screech frequency in the dispersion relation corresponding to an upstream-travelling neutral waves of the family (*m=0,n=2*), as can be seen in fig. 5.13. In this figure, the chosen wave is represented by the green ellipse at the Screech frequency (St ≈ 0.65). The experimental profile of the upstream instability at the *x/D=1.0* is compared to the theoretical one, in fig. 5.14.

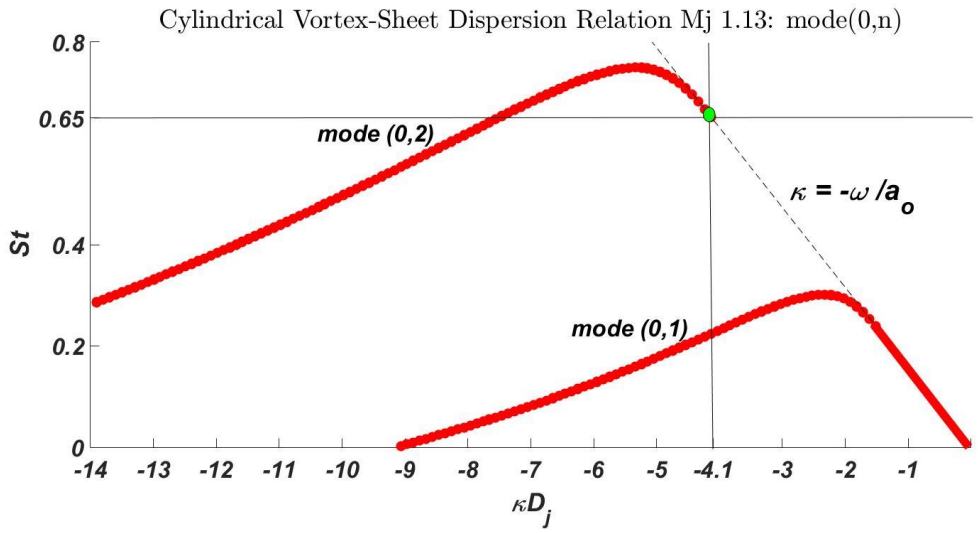

Figure 5. 13: solutions of the cylindrical vortex-sheet dispersion relation. Chosen point (green) in the family of waves (*m=0,n=2*).

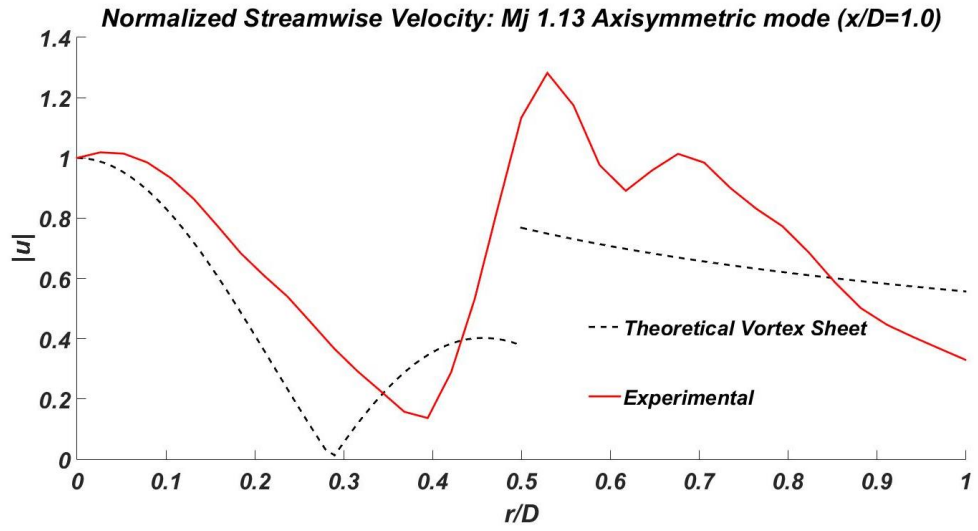

Figure 5. 14: Comparison between the amplitude of the velocity at the axial position *x/D=1.0* of the experimental upstream-travelling waves and the theoretical vortex-sheet eigenfunction for (*m=0, n=2*). *Mj=1.13,* the velocities are normalized by their value at the jet axis (*r/D=0*).

The experimental result agrees with the theoretical model, indicating the presence of upstream travelling neutral waves propagating inside and outside of the jet. Similar results were found out by Edgington-Mitchell *et al*. (2018). This result is coherent with the fact that the peaks of the modes *A1* and *A2* are inside of the allowable jet neutral modes frequencies (*m=0,n=2*), as shown in fig. 5.5. Thus, this result evidences, as already proposed by Edgington-Mitchell *et al*., that the upstream-travelling jet neutral instabilities (*m=0,n=2*) may play an important role in the Screech closure mechanism for the *A1* and *A2* modes.

5.3.3 Helical Screech Mode (C)

The spatial functions Φ, for the first and second POD modes of the jet undergoing helical *C* Screech mode, are depicted in fig. 5.15, where the streamwise and transverse velocity components are shown. The fact that the streamwise POD modes amplitudes are in opposite phase with respect to the jet axis indicates that the flow undergoes an helical instability. The relation between the temporal coefficients a_1a_2 (fig. 5.16) shows that the leading modes pair have similar and noticeable energy and that temporal coefficients are in phase quadrature which suggests that the POD has captured the cyclic motion of the coherent structures involved in the Screech. Moreover, the relation between the temporal coefficients shows an organized motion, ensuring that the jet is under helical motion contrary to the flapping mode where this organization is not clear, as cited in the previous chapters.

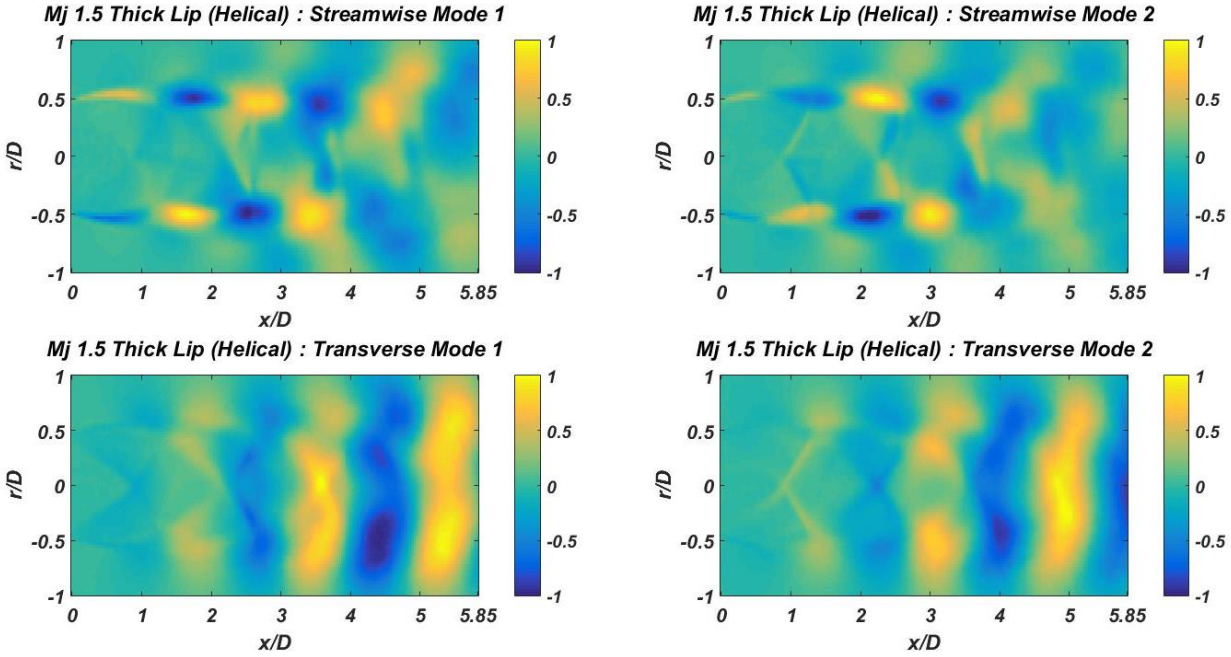

Figure 5. 15: spatial POD functions (Φ) of the modes 1 and 2, for the streamwise (top) and transverse (bottom) velocity components. Each mode is individually normalized by the respective maximum value of Φ .

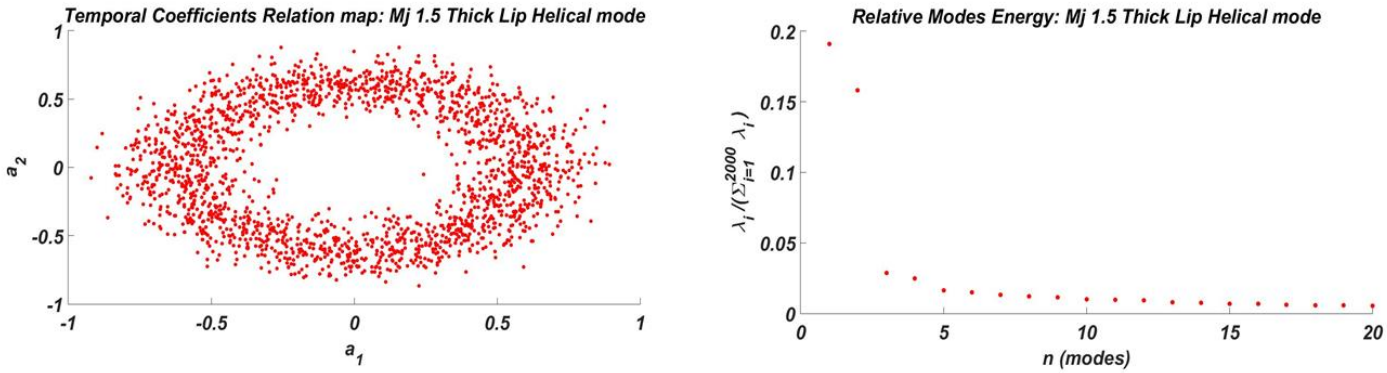

Figure 5. 16: temporal coefficients a_1a_2 (left) and relative modes energy (right) for *Mj=1.5*, C mode, thick lip nozzle.

Employing the spatial Fourier transform (eq. 5.16) of the complex function φ formed with the two first POD eigenfunctions $\varphi = \Phi_1 + i\Phi_2$, we obtain the wavenumber spectra of the streamwise velocity components ($\hat{u}_k^c$). The amplitude of $\hat{u}_k^c$ is presented in fig. 5.17. From this figure it is possible to remark a strong instability, represented by high energy levels, propagating downstream (κ>0) with a phase velocity lower than the speed of sound ($\kappa D_j = 2.5$). Most of the energy of this instability is located in the mixing layer ($r/D \approx 0.5$) and is associated to the Kelvin-Helmholtz instability. Similarly to the axisymmetric case, one can observe a noticeable energy in the negative *k* region, as shown by the dashed ellipse in the plot. These waves are propagating with a negative phase velocity and they have a velocity almost equal to that of speed of sound. Moreover, we can see that they have a support inside and outside of the jet core. This suggests the presence of the upstream neutral jet modes (*k-)* in the velocity fluctuations.

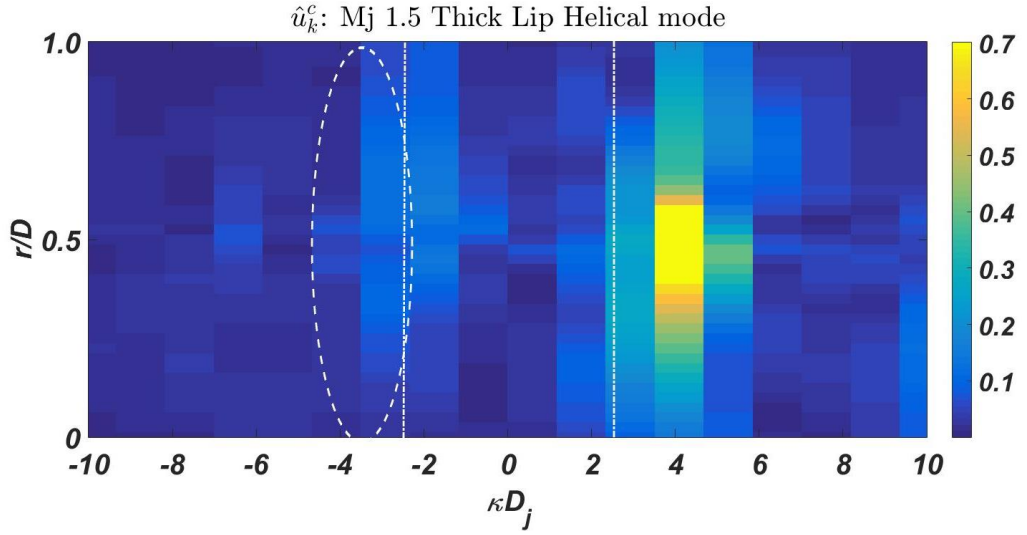

Figure 5. 17: wavenumber spectrum of the coherent streamwise velocity ($\hat{u}_k^c$). Vertical dashed lines represent the wavenumbers associated to the speed of sound at the Screech frequency in the upstream (negative values) and downstream (positive values) directions.

Again, as the wavenumbers are known, the downstream and upstream coherent waves, $\hat{u}_d^c$ and $\hat{u}_u^c$, respectively, can be obtained. The amplitude of positive phase velocity wavenumber ($kD_j \geq 0$) is depicted in fig. 5.18. One can remark that this downstream wave propagates in the

mixing layer, as expected from the Kelvin-Helmholtz instability. It is also possible to notice the growth associated to its unstable behaviour up to *x/D=2*. Then the saturation occurs where this instability becomes stable up to *x/D=3*, and subsequently decays beyond.

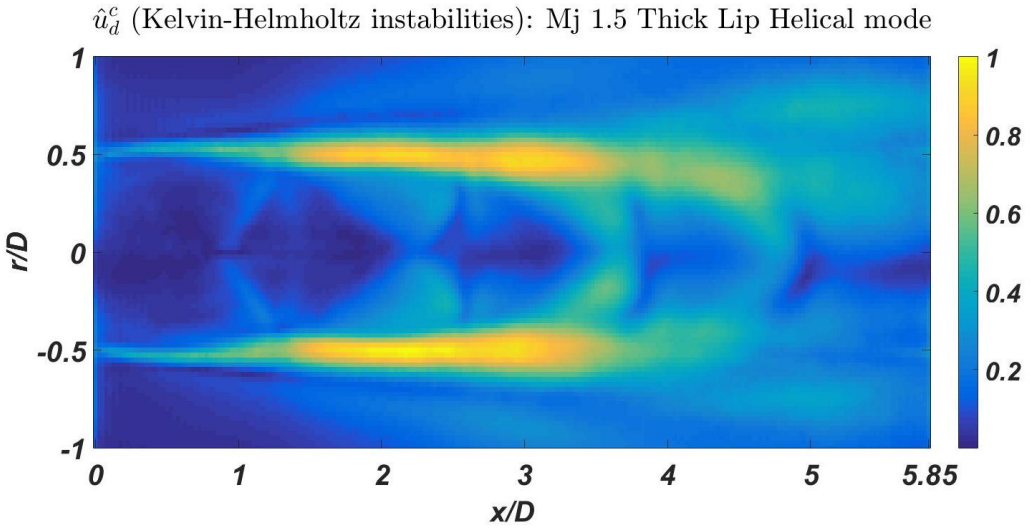

Figure 5. 18: amplitude of the downstream travelling waves normalized by the maximum value.

For the upstream travelling waves reconstruction, we consider two discrete values of kD_j=-2.92 and -4.1 to inverse the Fourier transform of $\hat{u}_k^c$. As for the axisymmetric case, the points were chosen due to fact that they are the closest to the sound waves wavenumber kD_j=-*2.5*. The upstream-travelling waves are depicted in fig. 5.19. The topology of the image reveals meaningful information about these waves: 1) it is possible to remark a discontinuity in the mixing layer (*r/D=±0.5*); 2) there is a high intensity lobe located between the jet axis and the mixing layer and 3) outside of the mixing layer (*r/D>±0.5)* it is possible to notice that, likewise the axisymmetric case, these instabilities present a remarkable energy that decay moving away from the jet boundary.

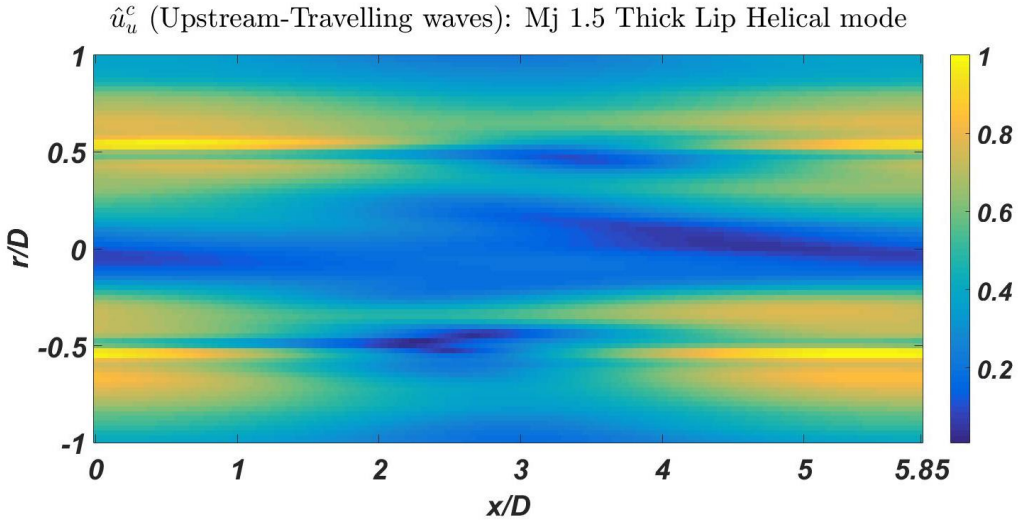

Figure 5. 19: amplitude of the upstream-travelling waves component associated to the negative wavenumbers (kD_j=-2.92 and -4.1), normalized by the overall maximum value.

Again, in order to validate the results obtained, a comparison between the experimental data and the model is carried out. It needs be stressed that, contrary to axisymmetric waves

(*m=0*), the vortex-sheet model predicts an allowable frequency band very narrow for the helical instabilitiy (*m=1*), as can be seen in fig. 5.6. As such, an eigenvalue κ (ω) is chosen close to the saddle point, representing an upper limit of the allowable frequencies for the upstream travelling waves, as one can see in the fig. 5.20. In this figure, the chosen point (κ (ω)) is represented by the green ellipse. Then, the experimental profile of the upstream instability ($\hat{u}_u^c$), at *x/D=5.0*, is compared to the theoretical one, as one can observe in fig. 5.21.

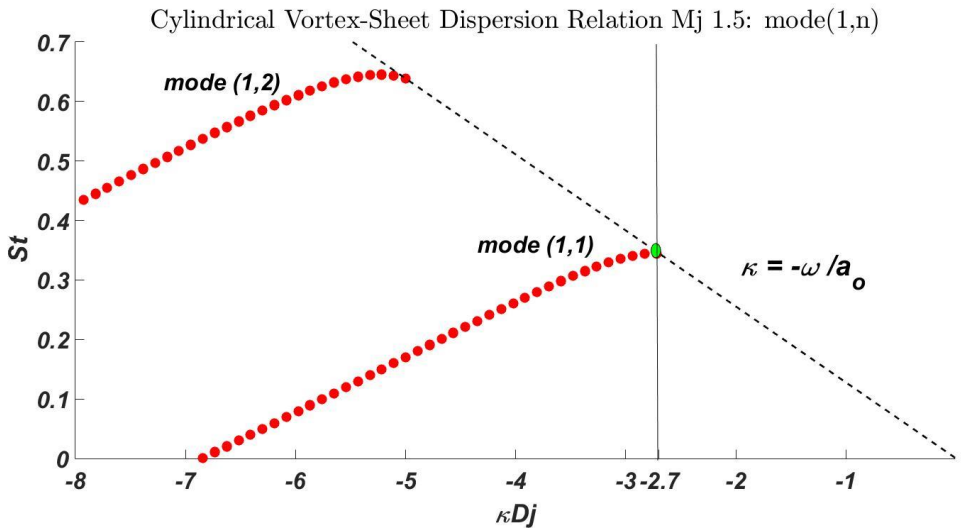

Figure 5. 20: solutions of the cylindrical vortex-sheet dispersion relation. Chosen point (green) in the family of waves of κ (*m=1,n=1*).

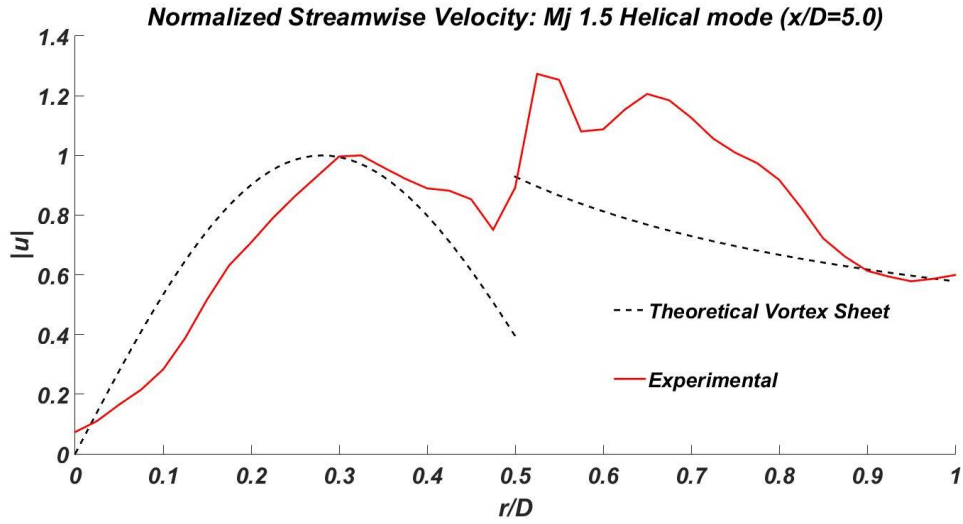

Figure 5. 21: Comparison between the amplitude of the velocity at the axial position *x/D=5.0* of the experimental upstream-travelling waves and the theoretical vortex-sheet eigenfunction for *k*(*m=1,n=1*), M_j*=1.5*. The velocities are normalized by the maximum value inside of the jet.

In this figure, one can notice a reasonable agreement between the experimental and theoretical velocities, suggesting the existence of helical neutral jet modes propagating upstream in the jet flow. Even though there is a small mismatch between the Screech and the allowable frequency range, showed in fig. 5.6, the results indicate that the upstream-travelling jet neutral instability may be involved in the closure of the Screech mechanism for the helical mode *C*. One possible reason for the mismatch between the allowable frequency range and the Screech is

maybe linked to the accuracy of the vortex-sheet model to predict the upstream neutral jet instabilities for the azimuthal mode 1, providing very narrow frequencies ranges.

5.3.4 Flapping Screech Mode (B)

The first and second spatial POD modes of the streamwise and transverse velocity fluctuations components are shown in fig. 5.22 for the jet undergoing the flapping Screech mode (M_j=1.5). The organization of the modes clearly shows that the jet is under a flapping mode instability: the fluctuations are anti-symmetrical with respect to the jet axis. The relation between the two first temporal coefficients a_1a_2, as well as the relative modes energy are depicted in fig. 5.23. In this figure, one can notice that all the conditions to perform the spatial Fourier decomposition of the spatial modes are not satisfied: the temporal coefficients do not scatter forming a Lissajous curve, suggesting a random and disorganized movement bonded to precession effect of the flapping mode, already explained in the chapter 3. However, the Fourier spatial decomposition of the POD modes will be carried out, in order to attempt to find any signature of the upstream waves in the velocity fields of the jets.

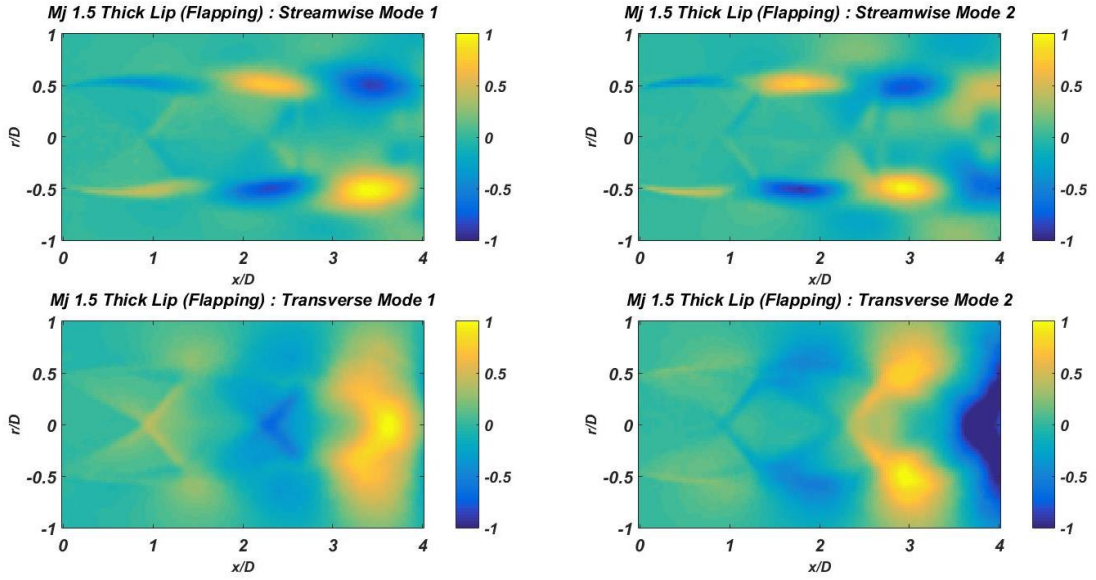

Figure 5. 22: spatial POD functions (Φ) of the modes 1 and 2, for the streamwise (top) and transverse (bottom) velocity components. Each mode is individually normalized by the respective maximum value of Φ .

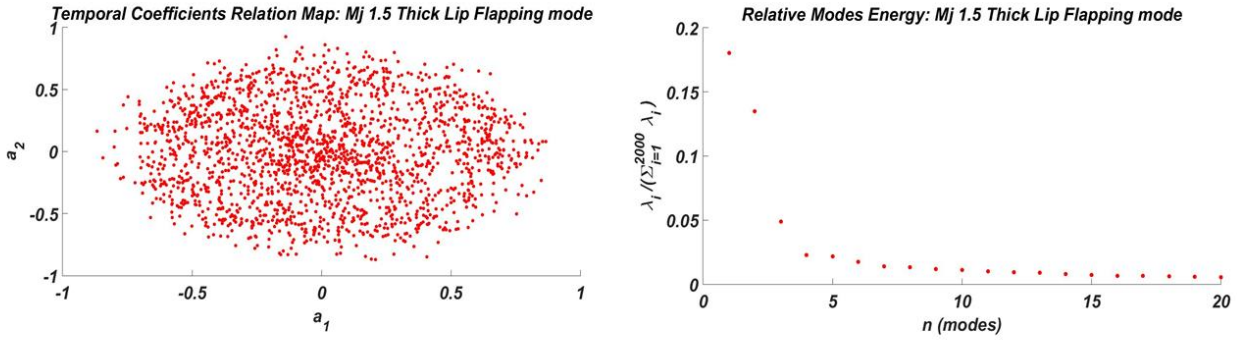

Figure 5. 23: temporal coefficients a_1a_2 (left) and relative modes energy (right) for *Mj=1.5*, B mode, thick lip nozzle.

The spatial Fourier transform (eq. 5.16) is applied to the complex function $\varphi=\Phi_1 + i\Phi_2$ in order to obtain the wavenumber spectra of the streamwise velocity components ($\hat{u}_k^c$). In fig. 5.24 we plot the amplitude of $\hat{u}_k^c$ as a function of the spatial wavenumber *kDj*. This figure shows a strong instability, represented by high energy levels, propagating downstream ($\kappa>0$) with a velocity lower than the speed of sound ($\kappa D_j = 2.1$), that again can be associated to the Kelvin-Helmholtz instability. One can also observe a noticeable energy in the negative *k* region, associated to the upstream propagation, with a phase velocity near to the speed of sound. As can also be seen, the energy of these waves is located inside and outside of the jet core, suggesting the presence of upstream neutral jet instabilities (*k-)*.

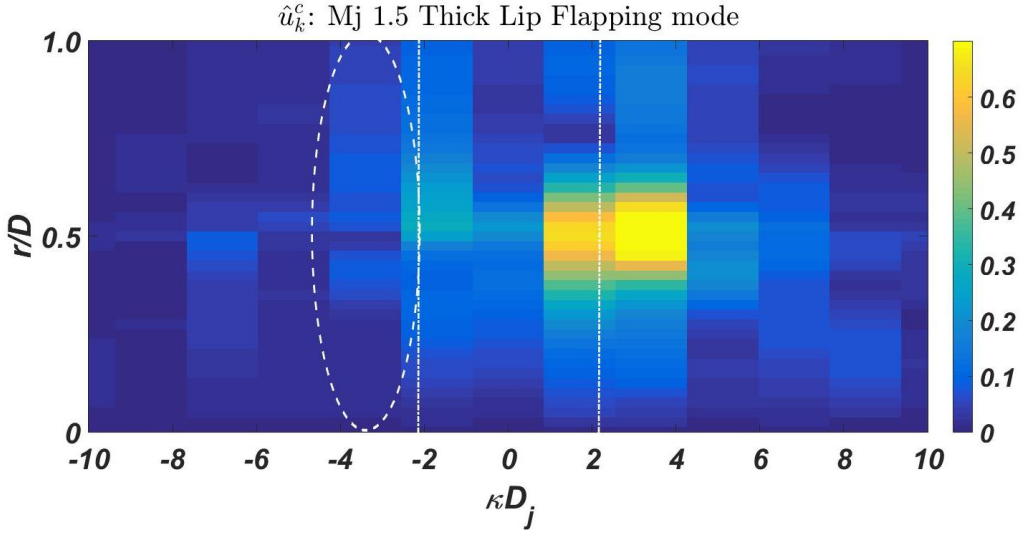

Figure 5. 24: wavenumber spectrum of the coherent streamwise velocity ($\hat{u}_k^c$). Vertical dashed lines represent the wavenumbers associated to the speed of sound at the Screech frequency in the upstream (negative values) and downstream (positive values) directions.

Since the wavenumbers are known, the downstream and upstream coherent waves, $\hat{u}_d^c$ and $\hat{u}_u^c$, respectively, can be obtained. As in the previous cases, the downstream waves are obtained by inverse Fourier transforming the positive wavenumbers ($kD_j \geq 0$) of $\hat{u}_k^c$. The amplitude of this positive phase velocity wave is depicted in the fig. 5.25. Similarly to the axisymmetric and helical cases, we can remark that this downstream wave, propagating in the mixing layer, is similar to the Kelvin-Helmholtz instability.

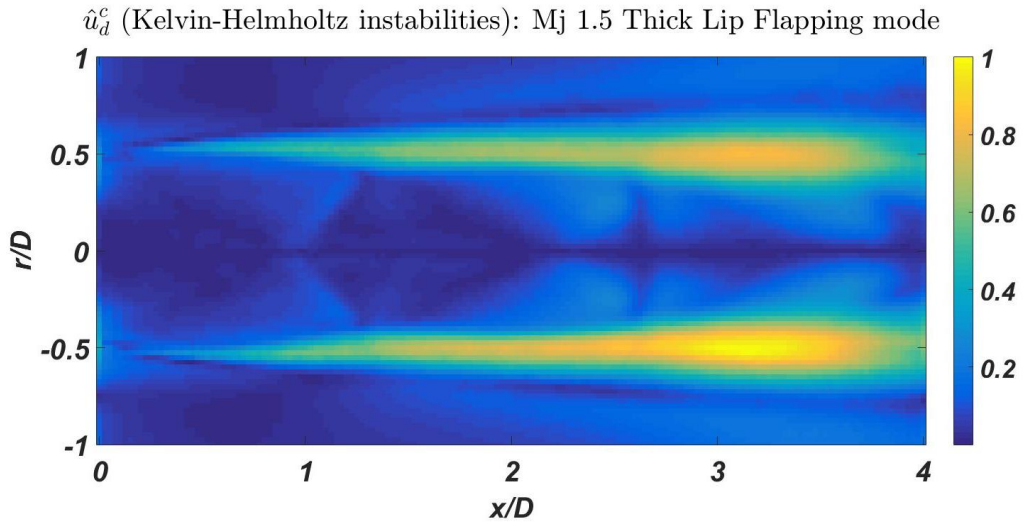

Figure 5. 25: amplitude of the downstream travelling waves normalized by the maximum value.

Concerning the upstream travelling waves reconstruction, two discrete wavenumbers kD_j=*-3.4* and *-5.1* were employed to inverse the Fourier transform of $\hat{u}_k^c$. Again, these values were chosen due to the fact that they are the closest available to the wavenumber of the speed of sound kD_j=*-2.1* at the Screech frequency. The amplitude of the upstream travelling instabilities are depicted in fig. 5.26. The topology of the image reveals a well marked pattern, represented by two lobes located between the jet axis and the mixing layer (*r/D=±0.5).* This mode shape corresponds to a family of upstream jet neutral waves (*m=1,n=2*). Indeed, the absence of a disturbance (lobe) in the jet axis (*r/D=0*) is due to the fact that these waves have an azimuthal wavenumber *m=1*. Moreover, the two lobes corresponds to radial order *n=2*.

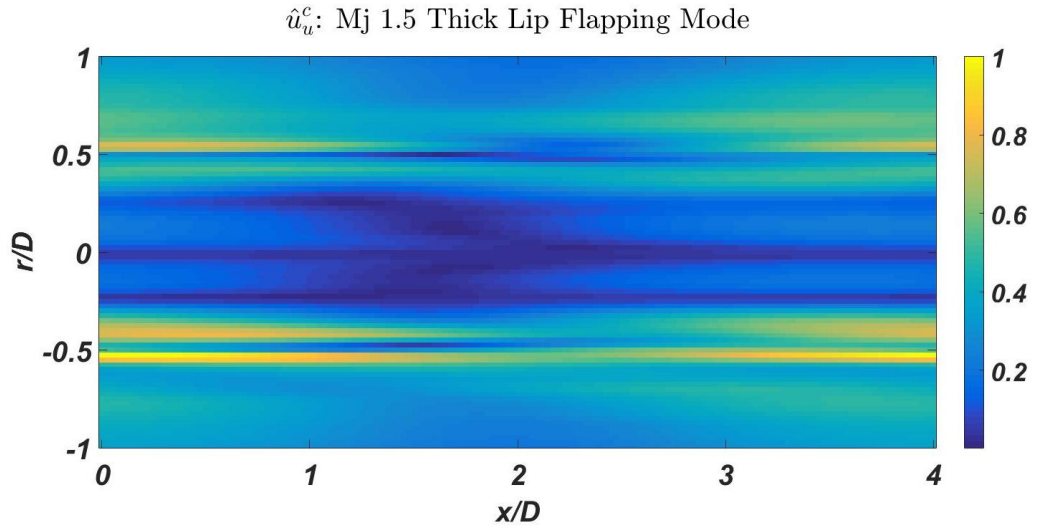

Figure 5. 26: amplitude of the upstream-travelling waves component associated to the negative wavenumbers (kD_j=*-3.4* and *-5.1*), normalized by the maximum value.

We carry out a similar analysis than employed in the previous section. In the fig. 5.27 we present the dispersion relation of the families of instabilities (*1,n*), for the jet at *Mj=1.5*. We can notice that the upstream travelling wave (*m=1,n=2*), represented by a blue circle, occurs for frequencies between *St=0.65* and *St=0.62*. As these values are strongly different than the flapping Screech frequency (*St=0.27*), we can assume that this family of instabilities is not

involved in the Screch closure mechanism. Even though the topology of the image (fig. 5.26) suggests that there is no presence of upstream travelling waves (*m=1,n=1)*, we carry out comparisons similarly to those made in the previous sections in order to provide additional results. As such, we compare the experimental data with theoretical vortex-sheet eigenfunction, at the eigenvalue (κ (ω)) corresponding to the saddle point of the upstream neutral jet family (*m=1,n=1*), represented by the green circle in fig. 5.27. The result of the comparison is depicted in fig. 5.28.

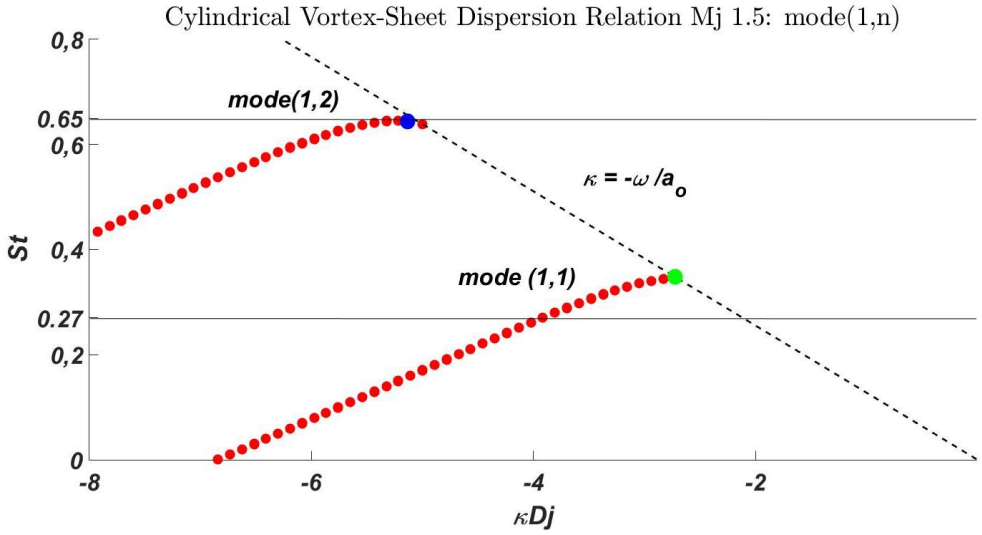

Figure 5. 27: solutions of the cylindrical vortex-sheet dispersion relation. Chosen points: green at the region of κ (*m=1,n=1*) and blue at the region of κ (*m=1,n=2*).

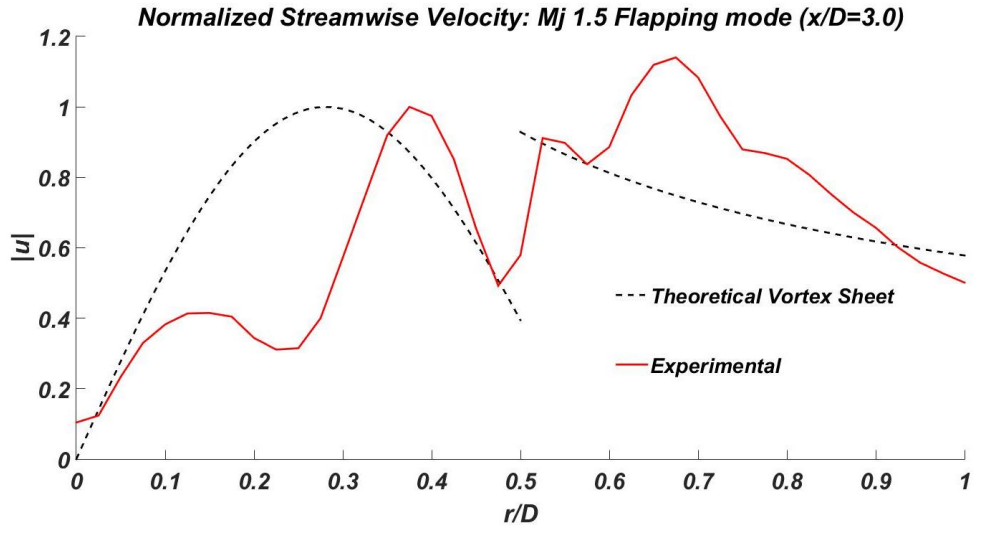

Figure 5. 28: Comparison between the amplitude of the velocity at the axial position x/D=3.0 of the experimental upstream-travelling waves and theorical vortex-sheet eigenfunction for *k*(*m=1,n=1*). *Mj=1.5*, flapping mode (*B*), the velocities are normalized by the maximum value inside of the jet.

From the fig. 5.28, as expected, we can notice that the signature of the upstream travelling waves observed experimentally does not correspond to the expected vortex-sheet eigenfunction which might be involved in the Screech closure mechanism. Indeed, two lobes are experimentally observed in the jet core whereas the model predicts only one, as could be seen in the case of the helical *C* Screech mode. Hence, we have shown the presence of upstream-

travelling waves of family (*m=1,n=2*) inside the jet. However this family of instabilities does not correspond to the Screech frequency. Therefore, one could infer that the Screech closure mechanism for the flapping mode might be driven by a different way than the axisymmetric and helical modes. For example, the initial excitation of Kelvin-Helmholtz instabilities can be provided by the freestream acoustic waves or another kind of instabilities propagating outside of the jet.

5.4 Screech Staging

Despite of the technical limitations in the study, the results presented in this chapter may give some contributions to the understanding of the Screech staging phenomenon, underpinned by different closure mechanisms. Firstly, we recall the Screech cycle, where the main elements are depicted in fig. 5.29. As such, the Screech results from coherent structures (Kelvin-Helmholtz instabilities) convected downstream inside of the mixing layer. These *KH* instabilities, at a specific shock location (*B2*), interact with the shock, with subsequent upstream waves propagation outside of the flow. These upstream instabilities reach the nozzle (*B1*), reflect on the lip and re-excite the initial instabilities (*KH*) in the shear layer. Then, the cycle is closed and the two waves are in resonance, interacting with the same frequency and delimited by two boundaries: the nozzle (*B1*) and the shock (*B2*).

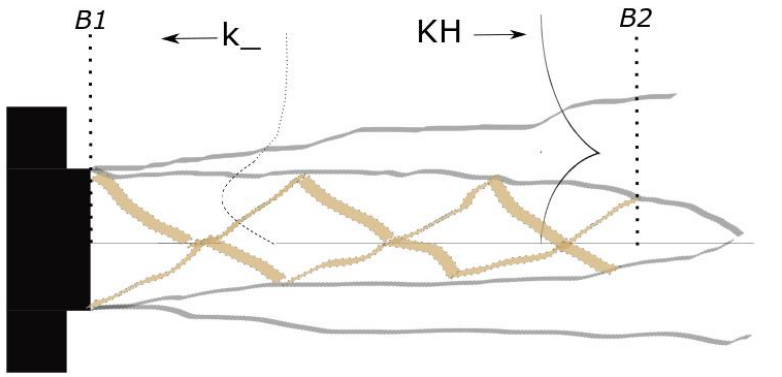

Figure 5. 29: sketch of the Screech phenomenon.

For the axisymmetric case (*A1* and *A2*), the results show that the Screech modes are dominant in the range of allowable frequencies of the upstream neutral jet modes of family (*m=0,n=2*). Then, as *Mj* increases the distance between the boundaries *B1* and *B2* also increases, due to the fact that the shock-cell length increases with the Mach number. This leads to a frequency decreasing that reaches a critical existence condition: the branch point of the upstream travelling neutral waves (*m=0,n=2*), as showed in fig. 5.5. Subsequently, there is a cessation of these dominant Screech modes. The result of this phenomenon is an abrupt fall of the frequencies in the shift *A* to *B* modes as the existence conditions of the axisymmetric upstream travelling neutral jet modes are no more satisfied.

We can conjecture two hypothesis for the large shift from *A2* to *B* Screech modes. The first one is that the "classical" mechanism is put into place, driving the flapping mode. However, this assumption requires that the boundary condition (*B2*) changes too. In other words, the classical mechanism emerges with a different characteristic length, leading to an increase in the distance between *B1* and *B2* with subsequent frequency decrease. We can infer that the Screech source shift from the 2nd to 3rd shock-cell, for example.

The second mechanism that emerge could be *similar* to the upstream neutral modes of the family (*m=1,n=1)* whose allowable frequencies range is lower than the (*m=0,n=2)* family, explaining the large discontinuity in the Screech frequency curve.

Still increasing the M_j, the supposed mechanism that drives the helical *C* Screech mode emerges: the upstream neutral jet waves of family (*m=1, n=1*). Thus, two distinct mechanims may coexist in the flow, the first driving the flapping *B* mode and the second being responsible for the closure of the helical *C* one. Therefore, the shift between dominant Screech *B*-*C* modes may be underpinned by the prominence of a closure mechanism over another. In other words, due to high unsteadiness behaviour of the phenomenon, the sudden suppression of a mechanism may enable the emergence of other as dominant, explaining the Screech staging between *B*-*C* modes. However, the details of this dynamic is not of the knowledge of the author.

Finally, the general explanation of the Screech staging phenomenon underpinned by the different mechanisms of closure seems to be plausible. Nevertheless, this reasoning needs further study to answer the questions that are still open: Why the flapping *B* mode does not exist in the M_j range where the axisymmetric modes (*A1* and *A2*) are dominant? What explain the staging between *A1* and *A2* modes? How the modes helical and flapping can be dominant over each other?

5.5 Conclusion

The results showed an excellent agreement between the Screech dominant axisymmetric modes (*A1* and *A2)* and the range of allowable frequencies of the upstream jet mode of family (*m=0,n=2*). Moreover, the vortex-sheet model and the Screech frequencies match differently according to the nozzle thickness. This means that changes in the flow conditions may influence the range of the allowable frequencies of the upstream neutral jet instabilities. This assumption is underpinned by modal changes in the screeching jets when the flows conditions are changed (Ponton & Seiner, 1992 and the present work).

The radial support of the upstream-travelling waves were compared to theoretical eigenfunctions of the vortex-sheet dispersion relation. A reasonable agreement was found for the axisymmetric (*A2*) and the helical (*C*) Screech modes, indicating that maybe these kind of instabilities may play a role as a Screech closure mechanism. However, for the flapping mode (*B*) the upstream-travelling waves observed did not correspond to the one predicted by the vortex-sheet model at the Screech frequency. This result leads to a plausible conclusion that the mechanism of Screech feedback closure for the flapping modes may be driven by another kind of waves travelling outside of the flow.

Finally, despite the experimental limitations, the results enable a preliminary and general explanation about Screech staging. It is inferred that the staging occurs due to the existence of different closure mechanisms. This reasoning does not explain the transition between the modes *A1* and *A2*, however provided the general lines that may rule the phenomenon, focused on the behaviour of upstream travelling instabilities.

6 CONCLUDING REMARKS AND PERSPECTIVES

In this part we will summarize the main results of this work and present possible perspectives in the Screech study, proposing suggestions for future works. Regarding the nozzle lip thickness influence, it was possible to notice that the thick lip nozzle causes modal changes in the flow compared to the thin lip one. Moreover, the thin lip nozzle generates jets with Screech frequencies higher than the thick one concerning the *A1*, *A2* and *B* modes, agreeing with literature, although the mode *C* almost does not change regardless of the nozzle. The azimuthal Fourier decomposition confirmed that the axisymmetric mode *A2* can be tracked over a large range of M_j conditions, although its amplitude is higher at lower M_j, and that the jet under axisymmetric dominant Screech modes does not present other tones, neither corresponding to flapping *B* mode nor helical *C* one. Furthermore, the results showed that classify the Screech modes in *D*, *E* and *F* remains more of a nomenclature issue than a physical sense, due to the fact that these ones are either flapping *B* mode extension or helical *C* mode reactivation.

We observed that the average shock-cell spacing did not present large difference between the thick and the thin lip cases. Concerning the standing wavelength, the flow generated by the thin lip nozzle presented higher values than those generated by the thick lip one, indicating that thin lip nozzle generates jets with small coherent structures moving faster inside of the mixing layer, providing higher Screech frequencies than those generated by thick lip one. In the fluctuations velocity analysis, we observed that the turbulence levels are larger for the jets generated by the thick lip nozzle than the thin lip one, suggesting that the coherent turbulent structures are larger in the flow generated by the former when compared to the latter. Finally, the POD of the velocity fluctuations fields showed that globally the lip thickness does not influence the dynamics of the coherent structures inside of the mixing layer.

The evaluation of the Screech mode effect on the flow showed that the Screech dominant mode instability almost did not influence the mean fields. Nevertheless, changes were noticed in the fluctuations ones. Indeed, the standing wavelength L_{sw} measured for the helical *C* mode was 80% of the flapping *B* one, which is linked to their frequencies differences. Concerning the turbulence features, it was observed that the up to second shock-cell both jets behave in similar way, but downstream of this point the turbulence levels for the flapping *B* mode are higher than for helical *C* one. This behaviour can be explained by the differences in the coherent structures propagating in the mixing layer due to different amplification of these ones by the different Screech frequencies. However, from the POD analysis we have observed that the flows have similar dynamics, represented by similar energy levels and spatial *POD* modes representing a convective motion.

The investigation of the closure mechanism revealed that the dominant axisymmetric Screech modes *A1* and *A2* arise inside the region of the allowables frequencies of the upstream neutral jet mode (*m=0,n=2*). Moreover, the vortex-sheet model and the Screech frequencies matched differently according to the nozzle thickness considered. This may mean that changes in the mixing layer thickness may generate different conditions for the upstream-travelling jet neutral waves existence, leading to modal changes in the screeching jets. The radial supports of the upstream jet neutral waves were compared to the theoretical streamwise eigenfunction and a reasonable agreement was found for axisymmetric (*A2*) and helical (*C*) Screech modes, indicating that these kind of instabilities may play a role as a Screech closure mechanism.

However, for flapping mode (*B*) the family of upstream travelling waves (*m=1,n=2*) observed did not correspond to the Screech frequency. This result leads to a plausible conclusion that the mechanism of Screech closure for flapping modes may be driven by another kind of waves. These results enabled a preliminar and general explanation about Screech staging underpinned by different closure mechanisms. This reasoning does not explain all questions about Screech staging, however it contributed giving the general lines that may rule the phenomenon.

Finally, Screech has been studied by several authors over the past seven decades, since Powell works in the *50's*. Although huge advances have been made during this period, the whole understanding of the phenomenon is still not achieved. The physics of the closure mechanisms and the role of the shock in the interaction between coherent structures/shock-cell are still open questions. However, this work provided meaningful information about the phenomenon, mainly with reference to the presence of upstream jet neutral waves as supposed closure mechanism for the axisymmetrics and helical modes, as well as the absence of these kinds of intabilities closing the flapping mode. Subsequently as future works we can suggest the study the upstream jet neutral waves for the modes axisymmetrics that may provide insightful information about the shift between the modes *A1* and *A2*. Moreover, a study could be carried out in order to evaluate the behaviour of these waves for helical Screech modes (*C*), analysing their relation with the nozzle thickness lip and the temperature ratio of the jet, with the purpose to understand the Screech modal changes in the flows reported in the literature and in the present work. We can suggest also works about the flapping *B* mode in order to determinate the nature of its feedback mechanism. We consider that the perspectives for Screech phenomenon studies will focus on the physic of upstream jet neutral waves and their relation with the tonal noises generated, instead of the aerodynamic effects and acoustics which were massively evaluated up to now.

REFERENCES

Alkislar, M.B., Krothapalli, A., and Lourenco, L.M., "Structure of a screeching rectangular jet: a stereoscopic particle image velocimetry study," *J. Fluid Mech*. 489, 2003, *pp* 121–154.

Ahuja, K. K.,"Basic experimental study of the coupling between flow instabilities and incident sound," NASA CR 3789, 1984.

Ahuja, K. K., "Some unique experiments on receptivity," *AIAA Paper 85-0533*, 1985.

Anderson Jr., J. D., "Fundamentals of Aerodynamics,*"McGraw-Hill*, 1991.

André, B., Castelain, T., and Bailly, C., "Shock-Tracking Procedure for Studying Screech-Induced Oscillations," *AIAA Journal*, Vol. 49, Issue 7, 2011, pp 1563-1566.

André, B., "Etude experimentale de l'effet du vol sur le bruit de choc de jets supersoniques sous-detendus," *Thèse de Doctorat*, Ecole Centrale de Lyon, 2012.

André, B., Castelain, T., and Bailly, C., "Shock Oscillations in a Supersonic Jet Exhibiting Antisymmetrical Screech,*" AIAA Journal*, Vol. 50, Issue 9, 2012, pp 2017-2020.

André, B., Castelain, T., and Bailly, C., "Investigation of the mixing layer of underexpanded supersonic jets by particle image velocimetry," *International Journal of Heat and Fluid Flow*,Vol50, 2014, pp 188-200

Aoki, T., Kweon, Y. H., Miyazato, Y., Kim, H. D. and Setoguchi, T., "An Experimental Study of the Nozzle Lip Thickness Effect on Supersonic Jet Screech Tones," *J. Mechanical Science and Technology*, Vol. 20, No. 4, 2006, pp. 522-532.

Bellaud, S., "Mesures et analyses détaillées des champs turbulents en couches de mélange annulaires supersoniques," *Thèse de Doctorat*, Université de Poitiers, 1999.

Berkooz, G., Holmes, P., and Lumley, J., "The proper orthogonal decomposition in the analysis of turbulent flows," *Annual review of fluid mechanics*, Vol. 25, No. 1, 1993, pp. 539–575.

Berry, M. G., Magstadt, A. S., and Glauser, M. N., "Application of POD on time-resolved schlieren in supersonic multi-stream rectangular jets," *Physics of Fluids*, 29, 2017.

Bishop, K. A., Ffowcs Williams, J. E., and Smith, W., "On the noise sources of the unsuppressed high speed jet," *Journal of Fluid Mechanics*, vol 50,1971, pp 21-31.

Bogdanoff, D. W., "Compressibility Effects in Turbulent Shear Layers*," AIAA Journal*, vol. 21, issue 6, 1983, pp 926-927.

Bridges, J. , and Wernet, M. P., "Turbulence associated with broadband shock noise in hot jets," *AIAA Paper 2008-2834*, 2008.

Brown, G. L., and Roshko, A., "On density effects and large structure in turbulent mixing layers*," Journal of Fluid Mechanics*, vol. 64, issue 4, 1974, pp 775-816.

Cantwell, B.J., "Organized motion in turbulent flow," *Ann. Rev. Fluid Mech*., 13, 1981, pp 457–515.

Cavalieri, A.V.G., Jordan, P., Colonius, T., Gervais, Y. "Axisymmetric superdirectivity in subsonic jets," *Journal Fluid Mechanics*, Vol. 704, 2012, pp. 388-420.

Chatterjee, A., Ghodake, D., and Singh, A., "Screech frequency prediction in underexpanded axisymmetric screeching jets," *International Journal of Aeroacoustics,* vol 8, 2009, pp 499–510.

Clem, M. M., Zaman, K. B. M. Q., and Fagan, A. F., "Background Oriented Schlieren Applied to Study Shock Spacing in a Screeching Circular Jet," *50th AIAA Aerospace Sciences Meeting*, 2012.

Clem M. M., Zaman K. B. M. Q., and Fagan, A. F., "Variation of shock-spacing during screech stage-jumps," *International Journal of Aeroacoustics,* Vol 15, issue 3, 2016, pp 324-335.

Clemens, N. T., and Mungal, M. G., ''Two and three-dimensional effects in the supersonic mixing layer,'' *AIAA Journal*, Vol 30, No 4, 1992, pp 973-981.

Crighton, D. G., "Basic Principles of Aerodynamic Noise Generation," *Progress in Aerospace Sciences*, Vol. 16, No. 1, 1975, pp. 31–96.

Crow, S. C., and Champagne, F. H., "Orderly Structure in Jet Turbulence," *Journal of Fluid Mechanics*, Vol. 48, 1971, pp. 547–591.

Davies, M. G., and Oldfield, D. E. S., "Tones from a choked axisymmetric jet. I. Cell structure, eddy velocity and source locations," *Acustica* 12 (4), 1962, pp 257–266.

Daviller, G., Lehnasch, G., and Jordan, P., "Numerical investigation of the influence of upstream conditions on properties of shock noise in shock/mixing layer interaction," *International Symposium on Turbulence and Shear Flow Phenomena*, 2013.

Dimotakis, P. E., "Two-dimensional shear-layer entrainment," *AIAA Journal*, vol. 24, issue 11, 1986, pp 1791-1796.

Dimotakis, P. E., "Turbulent Free Shear Layer Mixing and Combustion," *High Speed Flight Propulsion Systems, in Progress in Astronautics and Aeronautics*, 1991, pp 265-340.

Edgington-Mitchell, D., Honnery, D. R., and Soria, J., "The underexpanded jet mach disk and its associated shear layer," *Physics of Fluids*, 26, 2014a.

Edgington-Mitchell, D., Oberleithner, K., Honnery, D. R., and Soria, J., "Coherent structure and sound production in the helical mode of a screeching axisymmetric jet," *Journal of Fluid Mechanics*, 748, 2014b, pp 822–847.

Edgington-Mitchell, D., Honnery, D.R., and Soria, J., "Staging Behavior in Screeching Elliptical Jets," *International Journal of Aeroacoustics*, vol. 14, issue 7, 2015.

Edgington-Mitchell, D., Jaunet, V., Jordan, P., Towne, A., Soria, J., and Honnery, D. R., "Upstream-travelling acoustic jet modes as a closure mechanism for screech," *Journal of Fluid Mechanics*, Vol. *855*,*R1*, 2018.

Fleury, V., Bailly, C., Jondeau, E., Michard, M., and Juvé, D., "Space-Time Correlations in Two Subsonic Jets Using Dual Particle Image Velocimetry Measurements," *AIAA Journal*, 46 (10), 2008, pp 2498–2509.

Fu, S. and Li, Q., "Numerical simulation of compressible mixing layers," *International Journal of Heat and Fluid Flow*, vol 27, 2006, pp 895–901.

Gao, J. H., and Li, X. D., "A Multi-Mode Screech Frequency Prediction Formula for Circular Supersonic Jets," *15th AIAA/CEAS Aeroacoustics Conference (30th AIAA Aeroacoustics Conference)*, 2009.

Glass, D. R., "Effects of acoustic feedback on the spread and decay of supersonic jets," *AIAA Journal*, Vol 6, 1968, pp 1890–1897.

Glauser, M., and George, W., "An orthogonal decomposition of the axisymmetric jet mixing layer utilizing cross-wire velocity measurements," *Proceedings Sixth Symposium onTurbulent Shear Flows*,Toulouse, France, 1987a, pp. 10.1.1–10.1.6.

Glauser, M., and George, W., "Orthogonal decomposition of the axisymmetric jet mixing layer including azimuthal dependence," *Advances in Turbulence*, edited by G. Comte-Bellot and J. Mathieu. Spring-Verlag, 1987b, pp. 357–366.

Gojon, R., Bogey, C., and Mihaescu, M., "Oscillation Modes in Screeching Jets," *AIAA Journal*, Vol. 56, No. 7, 2018, pp. 2918-2924.

Harper-Bourne, M., and Fisher, M. J., "The noise from shock waves in supersonic jets," *AGARD CP131*, Noise Mechanism, 1973.

Hay, J. A., and Rose, E. G., "In flight shock cell noise," *Journal of Sound and Vibration*, Vol 11, 1970, pp 411–420.

Heeb, N., Gutmark, E., and Kailasanath, K., "An experimental investigation of the flow dynamics of streamwise vortices of various strengths interacting with a supersonic jet*," Physics of Fluids*, vol. 26, 2014a.

Heeb, N., Gutmark, E., Liu, J., and Kailasanath, K., "Fluidically enhanced chevrons for supersonic jet noise reduction." *AIAA Journal*. Vol 52, 2014b, pp 799–809.

Ho, C. M., and Huerre, P., ''Perturbed free shear layers,'' *Annual. Review of Fluid Mechanics*, Vol 16, 1984, pp 365-424.

Hu, T. F., and McLaughlin, D. K., "Flow and acoustic properties of low mach number underexpanded supersonic jet," *Journal of Sound and Vibration, v*ol 141, 1990, pp 485–505.

Hussain, A. K. M. F., "Coherent structures-reality and myth," *Physic of Fluids*, Vol 26, 1983.

Jaunet, V., Collin, E., and Delville, J., "POD-Galerkin advection model for convective flow*:* application to a flapping rectangular supersonic jet," *Exp Fluids*, vol. 57, n^{o} 5, 2016, p. 1-13.

Johannesen, N. H., "The mixing of free axially-symmetric jets of Mach number 1.40," *ARC R&M 3291*. 1957.

Jordan, P., Jaunet, V., Towne, A., Cavalieri, A. V. G., Colonius, T., Schmidt, O., and Agarwal, A., "Jet-flap interaction tones*". Journal of Fluid Mechanics*, Vol 853, pp 333-358, 2018.

Kaji, S., and Nishijima, N., "Pressure field around a rectangular supersonic jet in screech," *AIAA Journal*, Vol. 34, 1996, pp 1990-1996.

Kandula, M., "Shock-Refracted Acoustic Wave Model for Screech Amplitude in Supersonic Jets," *AIAA Journal*, Vol. 46, No. 3, 2008, pp. 682-689

Kastner, J., Samimy, M., Hileman, J., and Freund, J. B., "Comparison of Noise Mechanisms in High and Low Reynolds Number High-Speed Jets," *AIAA Journal*, Vol. 44, issue 10, 2006, pp 2251-2258.

Kerhervé, F., Jordan, P., Gervais, Y., Valière, J-C, Braud, P., "Two-point laser Doppler velocimetry measurements in a Mach 1.2 cold supersonic jet for statistical aeroacoustic source model," *Exp. in Fluids*, vol. 37, 2004, pp 419-437.

Kerhervé, F., Fitzpatrick, J., Jordan, P. "The frequency dependence of jet turbulence for noise source modelling". *Journal of Sound and Vibration.Vol* 296(12): pp 209 – 225, 2006.

Kim, Y., and Lee, D. J., "Acoustic properties associated with nozzle lip thickness in screeching jets," *Journal of Mechanic Science and Technology*, Vol 21 (5), 2007, pp 764–771.

Krothapalli, A., Hsia, Y., Baganoff, D., and Karamcheti, K., "The role of screech tones in mixing of an underexpanded rectangular jet," *Journal of Sound and Vibration*, Vol 106, 1986 , pp 119–143.

Krothapalli, A., and Strykowski, P. J., "Revisiting screech tones: effect of temperature," *34th Aerospace Sciences Meeting and Exhibit, Aerospace Sciences Meetings*, 1996.

Krothapalli, A., Soderman, P. T., Allen, C. S., Hayes, J. A., and Jaeger, S. M., "Flight effects on the farfield noise of a heated supersonic jet," *AIAA Journal*, vol 35, 6, 1997, pp 952–957.

Lassiter, L.W., and Hubbard, H. H., "The near noise field of static jets and some model studies of devices for noise reduction," *NACA Technical Report 1261*, 1954.

Lau, J. C., Morris, P. J., and Fisher, M. J., "Measurements in subsonic and supersonic free jets using a laser velocimeter," *Journal of FluidMechanics*, Vol 93, 1979, pp 1–27.

Lee, B. H. K., and Westley, R., "Effective axial source distribution in a chocked screech jet," *10th Aerospace Sciences Meeting*, 1972.

Lee, S., Lele, S. K., and Moin, P., "Direct numerical simulation of isotropic turbulence interacting with a weak shock wave," *Journal of Fluid Mechanics*, Vol 251, 1993, pp 533–562.

Lehnasch, G., “Contribution à L’étude Numérique des Jets Supersoniques Sous-Détendus, “ *Doctorat Thèse*, Université de Poitiers, 2005.

Lesieur, M., “Turbulence in Fluids,*”* Kluwer Academic Publishers, 1997.

Lessen, M., Fox, J., and Zien, H., “The Instability of Inviscid Jets and Wakes in Compressible Fluid,” *Journal of Fluid Mechanics*, Vol. 21, No. 1, 1965, pp. 129–143.

Love, E. S., Eugene, S., Lee, L. P., and Woodling, M. J., “Experimental and theoretical studies of axisymmetric free jets,” *NASA Tech. Rep. R-6*. 1959.

Lumley, J.L. “The structure of inhomogeneous turbulent flows”. *Atmospheric turbulence and radio wave propagation*, 1967, pp 166–178.

Mahadevan, R., and Loth, E., “High-speed cinematography of compressible mixing layers,” *Experiments in Fluids*, Vol 17, Issue 3, 1994, pp 179–189.

Mancinelli, M., “Etude de l’aérodynamique et de la stabilité de deux jets supersoniques , “ *Post Doc project, CNES*, internal report, 2018.

Massey, K. C., Ahuja, K. K., Jones III, R. R., and Tam, C. K. W., “Screech tones of supersonic heated free jets,” *32nd Aerospace Sciences Meeting and Exhibit*, 1994.

Massey, K. C., and Ahuja, K. K., “Screech frequency prediction in light of mode detection and convection speed measurements for heated jets,” *3rd AIAA/CEAS Aeroacoustics Conference*, 1997.

Massey, K. C., “Flow/acoustic coupling in heated and unheated free and ducted jets,” *Ph.D. Thesis*, Georgia Institute of Technology, 1997.

Melling, A., “Tracer Particles and seeding for particle emage velocimetry,” *Meas. Sci. Technology*. Vol 8, 1997, pp 1406-1416.

Mercier, B., Castelain, T., and Bailly, C., “Investigation of under-expanded jet screech associated convective velocity based on high frequency sampled schlieren visualisations,” 22ème Congrès Français de Mécanique, 2015.

Mercier, B., Castelain, T., and Bailly, C., “A schlieren and nearfield acoustic based experimental investigation of screech noise sources,” *22nd AIAA/CEAS Aeroacoustics Conference*. 2016.

Merle, M., “Sur la fréquence des ondes émises par un jet d’air à grande vitesse“. *Compte-Rendu de l’Académie des Sciences de Paris*, Vol. 243, 1956, pp. 490–493

Michalke, A., “A note on the spatial jet-instability of the compressible cylindrical vortex sheet”. 1970.

Mollo-Christensen, E., “Jet Noise and Shear Flow Instability Seen from an Experimenter’s Viewpoint,” *Journal of Applied Mechanics*. Vol. 34, No. 1, 1967, pp. 1–7.

Morrison, G. L., and McLaughlin, D. K., “The noise generation by instabilities in low Reynolds number supersonic jets,” *Journal of Sound and Vibration*, Vol 65, 1979, pp 177-191.

Morrison, G. L., and McLaughlin, D. K., “Instability process in low Reynolds number supersonic jets,” *AIAA Journal*, Vol 18, 1980, pp 793–800.

Munday, D., Gutmark, E., Liu, J., and Kailasanath, K., “Flow structure and acoustics of supersonic jets from conical convergent-divergent nozzles,” *Phys. Fluids*, vol 23, 2011.

Normand, X., “Transition à la turbulence dans les écoulements cisaillés compressibles libres ou pariétaux,“ *Thèse de doctorat*, Institut National Polytechnique de Grenoble, 1990.

Norum, T. D, “Screech suppression in supersonic jets,” *AIAA Journal*, Vol 21, No 2, 1983, pp 235–240.

Pack, D. C., “On the formation of shock-waves in supersonic gas jets: two-dimensional flow,” *The Quarterly Journal of Mechanics and Applied Mathematics*, Vol 1, Issue 1, 1948.

Pack, D. C., “A note on Prandtl’s formula for the wave-length of a supersonic gas jet,” *The Quarterly Journal of Mechanics and Applied Mathematics*, Vol 3, issue 2, 1950, pp 173–181.

Panda, J., Raman, G., and Zaman, K. B. M. Q., “Underexpanded screeching jets from circular, rectangular and elliptic nozzles,” *3rd AIAA/CEAS Aeroacoustics Conference*, 1997.

Panda, J, “Shock Oscillation in Underexpanded Screeching Jets,” *Journal of Fluid Mechanics*, Vol. 363, 1998, pp. 173–198.

Panda, J., “An experimental investigation of screech noise generation,” *Journal of Fluid Mechanics*, Vol 378, 1999, pp 71–96.

Panda, J., and Seasholtz, R.G., "Measurement of shock structure and shock-vortex interaction in underexpanded jets using Rayleigh scattering," *Phys. Fluids*, Vol 11, 1999, pp 3761–3777.

Panda, J., "Two Point Space–Time Correlation of Density Fluctuations measured in High Velocity Free Jets," *44th AIAA Aerospace Sciences Meeting and Exhibit*. 2006

Pantano, C., and Sarkar, S., "A Study of Compressibility Effects in the High-Speed Turbulent Shear Layer Using Direct Simulation," *Journal of Fluid Mechanics*, Vol. 451, 2002, pp. 329–371.

Pao, S. P., and Seiner, J. M., "Shock-associated noise in supersonic jets," *AIAA Journal*, Vol 21, No 5, 1983, pp 687–693

Papamoschou, D., and Roshko, A., "The compressible turbulent shear layer: an experimental study," *Journal of Fluid Mechanics*, Vol. 197, 1988, pp 453-477.

Papamoschou, D., and Bunyajitradulya, A., "Evolution of large eddies in compressible shear layers," *Physics of Fluids*, vol. 9, issue 3, 1997, pp 756-765.

Ponton, M. K., and Seiner, J. M., "The effects of nozzle exit lip thickness on plume resonance," *Journal of Sound and Vibration*, 154, issue 3, 1992, pp 531-549.

Powell, A., "On the mechanism of choked jet noise," *Proceedings of the Physical Society*, Section B 66, 12, 1953a, pp 1039–1056.

Powell, A., "On edge tones and associated phenomena," *Acustica*, Vol. 3, 1953b, pp. 233–243

Powell, A., Umeda, Y., and Ishii, R., "Observations of the oscillation modes of choked circular jets," *The Journal of the Acoustical Society of America*, vol 92, 5, 1992, pp 2823–2836.

Prandtl, L., "Über die stationären Wellen in einem Gasstrahl," *Physikalische Zeitschrift* 5, 19, 1904, 599–601.

Prasad, A. K., "Particle image velocimetry," *Review Article In : Current Science*, vol 79, no 1, 2000

Raman, G., and Rice, E. J., "Instability modes excited by natural screech tones in a supersonic rectangular jet," *Phys. Fluids*, Vol 6, 1994 , pp 3999–4008.

Raman, G., "Cessation of screech in underexpanded jets," *Journal of Fluid Mechanics*, vol 336, 1997, pp 69–90.

Raman, G., Panda, J., and Zaman, K. B. M. Q., "Feedback and receptivity during jet screech: influence of an upstream refector," *35th Aerospace Sciences Meeting and Exhibit*, 1997.

Raman, G., "Advances in Understanding Supersonic Jet Screech: Review and Perspective," *Progress in Aerospace Sciences*, Vol. 34, Nos. 1–2, 1998, pp. 45–106.

Raman, G., " Supersonic jet screech: Half-century from Powell to the present," *Journal of Sound and Vibration* 225(3), 1999, pp 543-571.

Rice, E. J., and Raman, G., "Enhanced mixing of a rectangular supersonic jet by natural and induced screech," *AIAA Paper 93-3263*, 1993

Rosfjord, T. J., and Toms, H. L., "Recent observations including temperature dependence of axisymmetric jet screech," *AIAA Journal, vol* 13, issue10, 1975, pp 1384–1386.

Samimy, M., and Elliott, G. S., "Effects of compressibility on the characteristics of free shear layers," *AIAA Journal*, Vol 28, 1990 , pp 439–445.

Savarese, A, "Experimental Study and Modelling of Shock-Cell Noise," *PhD these*, Université de Poitiers, 2014.

Seiner, J. M., and Norum, T. D., "Aerodynamic Aspects of Shock Containing Jet Plumes," *6th Aeroacoustics Conference*, 1980.

Seiner, J. M., Manning, J. C., and Ponton, M. K., "Model and full scale study of twin supersonic plume resonance," *25th AIAA Aerospace Sciences Meeting*, 1987.

Settles, G. S., and Hargather, M. J., "A Review of Recent Developments in Schlieren and Shadowgraph Techniques," *Measurement Science and Technology*, 2017.

Shen, H., and Tam, C. K. W., "Effects of jet temperature and nozzle-lip thickness on screech tones," *AIAA Journal*, Vol 38, No 5, 2000.

Shen, H., and Tam, C., "Three-dimensional numerical simulation of the jet screech phenomenon," *AIAA Journal*, Vol 40, 2002, pp 33–41.

Sherman, P. M., Glass, D. R., and Duleep, K. G., "Jet flow field during screech," *Appl. Sci. Res*, Vol 32, 1976, pp 283–303.

Sirovich, L., “Turbulence and the dynamics of coherent structures. part 1: coherent structures,” *Quarterly of Applied Mathematics*. Vol 45:, 1987, pp 561–571.

Suzuki, T., and Lele, S. K., “Shock leakage through an unsteady vortex-laden mixing layer: application to jet screech,” *Journal of Fluid Mechanics*, Vol. 490, 2003, pp. 139–167.

Talbot, B., Danaila, L., and Renou, B., “Variable-viscosity mixing in the very near field of a round jet.” *Phys. Scr*., 2013.

Tam, C. K.W., “On the noise of a nearly ideally expanded supersonic jet,” *Journal of Fluid Mechanics*, Vol 51, 1972 , pp 69-95.

Tam, C. K.W., and Tanna, H. K., “Shock associated noise of supersonic jets from convergent-divergent nozzles,*” Journal of Sound and Vibration*, Vol. 81, No 3, 1982, pp 337–358.

Tam, C. K.W., Jackson, J. A., and Seiner, J. M., “A multiple-scales model of the shock-cell structure of imperfectly expanded supersonic jets,” *Journal of Fluid Mechanics*, vol 153, 1985, pp 123–149.

Tam, C. K. W., Seiner, J. M., and Yu, J. C., “Proposed relationship between broadband shock associated noise and screech tones,” *Journal of Sound and Vibration*, Vol 110, issue 2, 1986, pp 309–321.

Tam, C. K. W., and Hu, F., “On the three families of instability waves of high-speed jets,” *J. Fluid Mech*, Vol 201, 1989, pp 447–483.

Tam, C. K. W., Ahuja, K. K., and Jones III, R. R., “Screech tones from free and ducted supersonic jets,” *AIAA Journal*, Vol 32, No 5, 1994.

Tam, C.K.W., "Supersonic Jet Noise", *Annual Review of Fluid Mechanics*, vol. 27, 1995, pp. 17-43

Tam, C. K., Parrish, S. A., and Viswanathan, K., “Harmonics of Jet Screech Tones,” *AIAA Journal*, Vol. 52, No. 11, 2014, pp. 2471–2479.

Tan, D. J., Soria, J., Honnery, D., and Edgington-Mitchell, D., “A Novel Method for Decoupling the Velocity Fluctuations in Screeching Axisymmetric Jets,” *22nd AIAA/CEAS Aeroacoustics Conference*, 2016.

Tan, D. J., Soria, J., Honnery, D., and Edgington-Mitchell, D., "Novel method for investigating broadband velocity fluctuations in axisymmetric screeching jets," *AIAA Journal*, Vol. 55, No. 7, 2017, pp. 2321-2334.

Towne, A., Cavalieri, A. V. G., Jordan, P., Colonius, T., Schmidt, O., Jaunet, V., and Brès, G., "Acoustic resonance in the potential core of subsonic jets," *Journal of Fluid Mechanics*, Vol 825, 2017, pp. 1113-1152.

Umeda, Y., and Ishii, R., "On the sound sources of screech tones radiated from choked circular jets," *The Journal of the Acoustical Society of America*, vol 110, issue 4, 2001.

Viswanathan, K., "Scaling laws and a method for identifying components of jet noise," *AIAA Journal, Vol* 44, No 10, 2006, pp 2274–2285.

Walker, S. H., and Thomas, F. O., "Experiments characterizing nonlinear shear layer dynamics in a supersonic rectangular jet undergoing screech," *Physics of Fluids*, Vol 9, Issue 9, 1997, pp 2562-2579

Weightman, J. L., Amili, O., Honnery, D., Edgington-Mitchell, D., and Soria, J., "On the Effects of Nozzle Lip Thickness on the Azimuthal Mode Selection of a Supersonic Impinging Flow," *23rd AIAA/CEAS Aeroacoustics*, 2017.

Westley, R., and Woolley, J. H., "Flow and Sound Visualization of an Axisymmetric Choked Jet". 16 mm Ciné Film, no. 13, 1968, NRC/NAE library.

Westley, R., and Woolley, J. H., "The near field sound pressures of a choked jet during a screech cycle," *AGARD Conference Proceedings*, No. 42, 1969

Westley, R., and Woolley, J. H., "Flow and Sound Visualization of an Axisymmetric Choked Jet," 16 mm Ciné Film, no. 13, 1970, NRC/NAE library.

Westley, R., and Wooley, J., "The near field sound pressures of a choked jet when oscillating in the spinning mode," *AIAA Paper* 479, 1975.

Wlezien, R. W., and Kibens, V., "Influence of nozzle asymmetry on supersonic jets," *AIAA Journal*, Vol 26, 1, 1988, pp 27–33.

Zaman, K. B. M. Q., "Spreading Characteristics of Compressible Jets from Nozzles of Various Geometries," *Journal Fluid Mechanics*, Vol. 383, 1999, pp 197-228.

RESUME

Cette thèse est une contribution expérimentale à l'étude des résonances aéroacoustiques des jets sous-détendus : le Screech. Diverses méthodes expérimentales sont utilisées à cette fin, telles que la mesure de pression acoustique, la strioscopie et la Vélocimétrie par Image de Particules, et associées à des techniques classiques de post-traitement comme les décompositions en mode de Fourier et aux valeurs propres. Ces Techniques permettent d'évaluer les effets d'épaisseur de la lèvre de la buse sur l'écoulement, et fournissent des informations sur les différences de comportement d'un même jet montrant des modes oscillatoires différents. Enfin, on entreprend d'étudier la présence de divers mécanismes de fermeture de la boucle de résonance pour divers modes de Screech. La présence d'ondes intrinsèques au jet, se propageant vers l'aval pour les modes axisymétrique (*A2*) et hélicoïdal (*C*) suggèrent que ces ondes puissent jouer un rôle dans la résonance. La signature de ces ondes n'est en revanche pas attestée pour les modes battants (*B*). Ces résultats semblent donc indiquer que plusieurs mécanismes de rétroaction différents puissent être à l'oeuvre dans la résonance du jet sous-détendu.

Mots clés: Screech, Jets Sous Détendu, Mécanisme de Fermeture

ABSTRACT

This work provides an experimental contribution to the study of the Screech phenomenon. Various experimental techniques such as microphones array, Schlieren and Particle Image Velocimetry (PIV) together with advanced post-processing techniques like azimuthal Fourier decomposition and Proper Orthogonal Decomposition (POD) are employed. These techniques enable the evaluation of the lip thickness effects on the jets generated by two different round nozzles. The differences on the flow aerodynamics and acoustics are discussed. Then, we carry out experiments to analyse the effects of the different dominant Screech modes (*B* and *C*) on the flow characteristics. No noticeable differences are found in the mean fields. However, the fluctuation fields shows the contrary: B mode has larger fluctuation. In the last part, we investigate the Screech closure mechanism. The signature of upstream jet waves is revealed in the axisymmetric (*A2*) and helical (*C*) mode. However, the mode *B* does not present evidence of this instability in the flow, indicating that its closure mechanism may be bonded to another kind of waves. The conclusion from these results is that the Screech phenomenon seems be driven by different closure mechanisms.

Keywords: Screech, Underexpanded Jets, Closure Mechanism